TECHNISCHE UNIVERSITÄT WIEN

HEPHY
INSTITUT FÜR HOCHENERGIEPHYSIK

DIPLOMARBEIT

Geant4 simulation of a particle range telescope used as calorimeter at MedAustron

zur Erlangung des akademischen Grades

Diplom-Ingenieur

im Rahmen des Studiums

Technische Physik

eingereicht von

Vera Teufelhart BSc
Matrikelnummer 09971447

ausgeführt am Atominstitut
der Fakultät für Physik
der Technischen Universität Wien

Betreuung
Betreuer: Univ.Prof. Dipl.-Phys. Dr.rer.nat. Jochen Schieck
Mitwirkung: Univ.Ass. Dipl.-Ing. Dr.techn. Albert Hirtl
Univ.Lektor Dipl.-Ing. Dr.techn. Thomas Bergauer

Wien, am 13. Februar 2020

(Unterschrift VerfasserIn) (Unterschrift BetreuerIn)

Contents

1 Introduction

With the average life expectancy of the world population increasing, cancer becomes a more and more widespread problem in our aging society. Radiation therapy is one important pillar of successful cancer treatment. The basic idea is to deliver energy to the tumour region with the help of radiation. The energy is taken up by the cancer cells which are destroyed as a result. In the surrounding healthy tissue there should ideally be no energy deposited at all, so as not to harm it. This is not possible as the radiation has to be transported into the tumour region which will always lead to some exposure. The challenge is to keep it as small as possible.
Conventional radiation therapy as can be found in many hospitals works with photons as energy deliverers, e.g. x-rays or gamma rays. Over the last decades, a new radiation therapy method has been developed: particle therapy [1]. Instead of photons, massive particles are used to deliver the energy to the tumour region. Particle types are mainly protons, but also heavier ions like carbon or helium, and sometimes electrons or neutrons. In this thesis, the focus will be on protons.
The large advantage of ions in contrast to photons is their very different dose profile [2]. In Figure 1.1, the dose profile is shown for photons, protons and carbon ions. When photons enter matter, the energy deposition as a function of penetration depth quickly rises to a maximum shortly after the entrance point, followed by an exponential decrease. Protons and carbon ions, however, deposit most of their energy at the very end of their path. The dose profile shows a distinctive peak, the so-called Bragg peak. Before that, there is a steady plateau, and after the peak, the dose quickly falls down to zero. This is very well suited for cancer treatment as the main part of the energy is deposited in a small region [4]. There is only a minor energy deposit before that region. Behind the Bragg peak, protons deposit no energy at all. Carbon ions show a minor deposit known as fragmentation tail.
There are several facilities worldwide which offer ion therapy [5]. One of them, called MedAustron [6], is situated in Austria, near Vienna. Treatment planning in those facilities is currently done on the basis of x-ray computed tomography (CT) images. From these, the stopping power (SP) distribution in the patient is calculated as this is the quantity needed for ion therapy planning [7]. This calculation introduces errors which compromise the effectiveness of the therapy. As an improvement, the SP can also be measured directly in a proton computed tomography (pCT) [8] .
The details of a pCT setup are described in Section 2.5. The basic components are

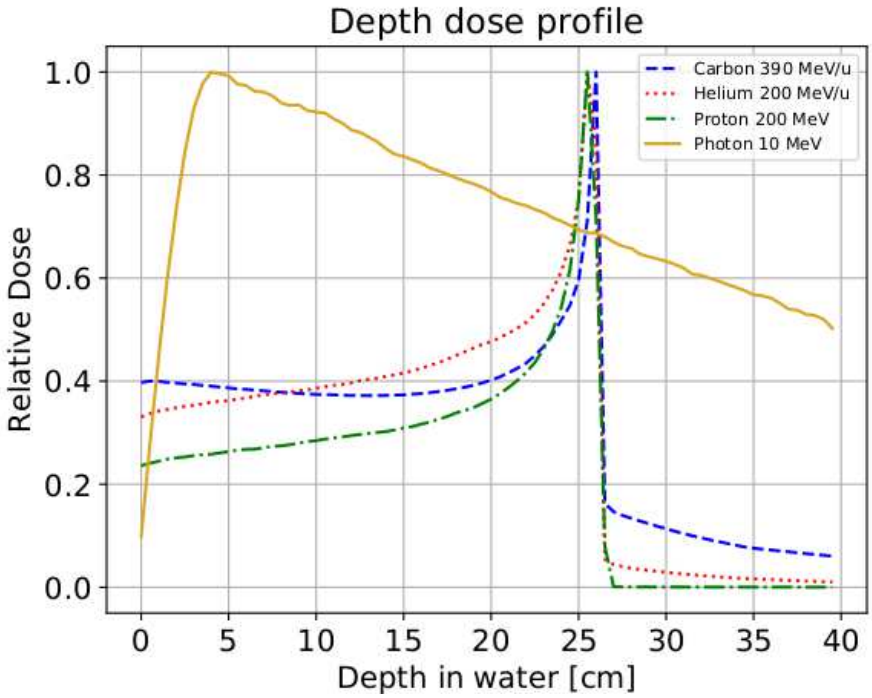

Figure 1.1: Energy deposit as a function of the penetration depth into matter for different particle types [3].

tracking modules in front and after the target (patient) and a residual energy measurement device at the end. Which technology and which exact layout are best suited for the requirements in a pCT [9], is not clear. Different research groups investigate various setups [10, 11]. A possible detector for energy measurement is a calorimeter. One particular calorimeter, the Proton Range Radiography 30 (PRR30), is studied in this thesis to find out if it is suitable for proton computed tomography. The calorimeter was simulated using the Geant4 [12] software toolkit to investigate properties like measurable energy range and resolution. Two approaches of simple alterations were also tested.

2 Physical background

When particles traverse matter, they interact with the target material which makes them lose energy, i.e. they slow down. Depending on the type of particles and on the properties of the target material, different processes may take place. Interaction partners are the electrons and nuclei of the material. Some typical interaction processes with target electrons are ionisation and excitation. Spallation and fission are examples for nuclear interactions. The information in this Physics chapter is mainly taken from [13].

2.1 Interaction of photons with matter

For photons, three processes are important as they traverse matter: photoelectric effect, Compton effect and pair production.
Photoelectric effect is the absorption of the photon by an atom which consequently releases an electron. The photon energy E_γ must be at least larger than the binding energy of the electron E_B. The Compton effect describes the energy loss due to inelastic scattering of the photon by an electron. The electron is again released from the material. Pair production occurs only in the presence of an electromagnetic field where the photon is converted into an electron and a positron. The photon energy must be at least as much as the sum of the rest masses of both produced particles, $E_\gamma \geq 2m_e c^2$.
The cross sections of these three processes show different dependencies on energy and absorber material. As the interaction probability is proportional to the cross section, each process is most probable in a certain regime, as shown in Figure 2.1. The vertical axis shows the atomic number Z of the target material. The horizontal axis shows the photon energy E_γ. Generally, it can be said that for small energies the photoelectric effect is dominant. In contrast, pair production is dominant at high energies. Between these two regimes, the Compton effect will occur most likely. This Compton regime gets more and more confined in energy as Z increases. It can be deduced that, in high-Z materials, absorption processes are much more likely for photons. As can be seen in Figure 2.1, pair production is almost certain for photon energies $E_\gamma > 50\,\mathrm{MeV}$.
The intensity of a photon beam traversing matter is decreasing because photons get absorbed along the way. As a function of penetration depth z, the intensity shows an exponential decline

$$I(x) = I_0 \exp(-\mu z), \tag{2.1}$$

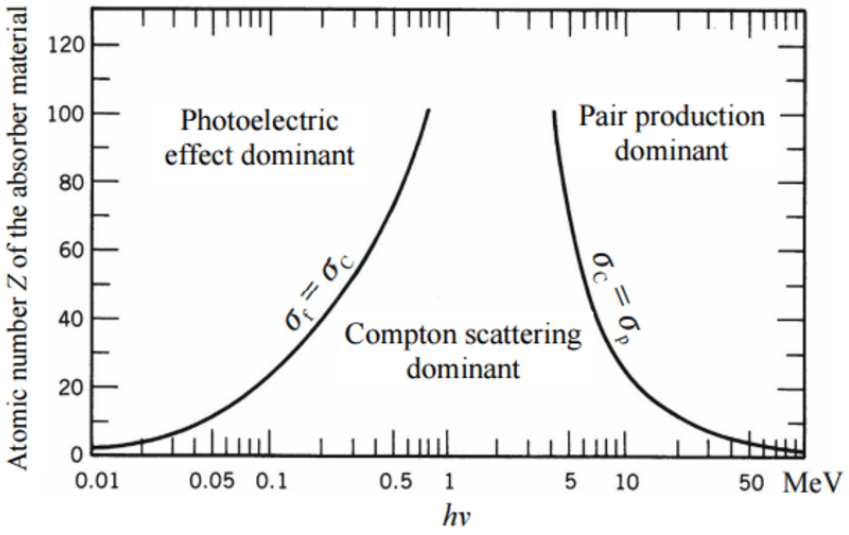

Figure 2.1: Dominant photon interaction processes for photon energy E_γ traversing material with atomic number Z [14].

where I_0 is the initial intensity of the beam when entering and μ is the linear attenuation coefficient of the material.

2.2 Interaction of charged particles with matter

Charged particles can interact via the electromagnetic force with both the target electrons and nuclei. This leads to ionisation and excitation of the material as well as the emission of photons. For hadrons, also strong interaction with the nucleons is possible, which may result in nuclear excitation, or even spallation and fission processes.

2.2.1 Ionisation and excitation

If the particle interacts with the electrons, it can transfer energy ΔE. If this energy ΔE is larger than the binding energy of the electron E_B, the electron can escape. Alternatively, if $\Delta E < E_\mathrm{B}$, the electron can not escape but is elevated to a higher-energy state. The atom is called excited. Deexcitation brings the electron back to its initial state while the energy difference is emitted in form of a photon or a less tightly bound electron.

2.2.2 Bremsstrahlung

The mass of electrons and positrons is much smaller than that of protons. In the Coulomb field of a nucleus, they are significantly deflected from their path. As this is an acceleration of a charged particle in an electromagnetic field, it leads to the emission of photons, so-called bremsstrahlung. The photon output is proportional to $\frac{E}{m^2}$, where E and m are

the energy and mass of the charged particle, respectively. Therefore, energy loss through bremsstrahlung is much more important for light-weight particles. But if the energy is very high, even the energy loss of heavy particles may contain a significant bremsstrahlung part.

2.2.3 Critical energy

For charged particles in matter, ionisation/excitation and bremsstrahlung are competing energy loss processes. They follow different dependencies on particle energy and target material. The energy loss per path length shows the following relations:

$$\left(\frac{dE}{dx}\right)_{\text{ionisation}} \propto Z \ln\left(\frac{E}{m}\right) \tag{2.2}$$

$$\left(\frac{dE}{dx}\right)_{\text{bremsstrahlung}} \propto Z^2 \frac{E}{m^2}. \tag{2.3}$$

Z is the atomic number of the target material, E and m are the energy and mass of the particle, respectively. From this, one can see that bremsstrahlung is only important for light charged particles, that is, electrons and positrons. There is also a difference in energy dependency. Due to the linear proportionality, bremsstrahlung accounts for larger energy loss rates at high particle energies. As the energy of the particle decreases, ionisation and excitation take over as dominant energy loss processes.
There is one energy where both processes lead to the same energy loss per path length. This energy is called the critical energy E_c. It is defined as

$$\left(\frac{dE}{dx}(E_\text{c})\right)_{\text{ionisation}} = \left(\frac{dE}{dx}(E_\text{c})\right)_{\text{bremsstrahlung}}. \tag{2.4}$$

For electrons, E_c can be calculated from the empirical formula [15]

$$E_\text{c} = \frac{800\,\text{MeV}}{Z + 1.2}. \tag{2.5}$$

2.2.4 Bethe-Bloch equation

Ions count as heavy particles when compared to electrons and positrons ($m_\text{p} \approx 10^3 \cdot m_\text{e}$). In the energy regime below E_c, they interact mainly with the electrons of the target atoms, leading to ionisation and excitation of the atoms. This corresponds to a series of many small interactions with equally small energy losses. The energy loss from this series of interactions is cumulatively described as an energy loss per path length, which is expressed in the Bethe-Bloch formula [13]:

$$S = -\left\langle \frac{dE}{dx} \right\rangle = \frac{e^4}{4\pi m_\text{e}(c\varepsilon_0)^2} \cdot \frac{\rho_\text{el} z^2}{\beta^2} \cdot \left[\frac{1}{2}\ln\left(\frac{2m_e c^2 \beta^2 T_\text{max}}{I \cdot (1-\beta^2)}\right) - \beta^2 - \frac{\delta}{2} - \frac{C}{Z}\right] \tag{2.6}$$

e	...	elementary charge
m_e	...	electron mass
c	...	speed of light
ε_0	...	electric constant
ρ_el	...	electron density of target material
z	...	charge of particle
$\beta = \frac{v}{c}$	...	velocity of particle, divided by the speed of light
T_max	...	maximum energy transfer to hull electron
I	...	mean ionization potential of target material

As the energy loss happens through many small interactions that are not exactly predictable, the Bethe-Bloch formula can only give a mean value. Statistical fluctuations have to be kept in mind.
The last two terms in Equation (2.6) are corrections for energy extrema. The density correction term $\frac{\delta}{2}$ is important for high energies $\beta \approx 1$. The shell correction term $\frac{C}{Z}$ is needed in case of low energy particles with $\beta \ll 1$.
The negative of $\frac{dE}{dx}$ is called the stopping power S. Figure 2.2 shows the stopping power as a function of energy for a muon in copper. For the Bethe-Bloch regime, indicated by the red arrow, there are roughly three domains. At lowest energies, the curve shows a $\frac{1}{\beta^2}$ drop, towards high energies it rises with $\ln\beta$. In between, there is a broad minimum at $\beta\gamma \approx 0.95$. Particles in this regime are called *minimum ionizing particles*, MIPs. The $\frac{1}{\beta^2}$ term has the effect that ions lose most of their energy towards the end of their path when they have become very slow. This results in a sharp peak in the function of energy loss over depth, see Figure 1.1. This is called the Bragg peak and is the reason why ions are very useful in radiation therapy. It means that the energy deposition per path length is highest in a very small region at the very end of the particle's path. The position of the Bragg peak can easily be manipulated by changing the initial energy of the ions.

2.2.5 Range of ions in matter

The range of ions in a material can be calculated from the Bethe-Bloch formula by integrating the stopping power over the energy from the initial kinetic energy T_0 to zero.

$$R(T_0) = \int_{T_0}^{0} \left\langle \frac{dE}{dx} \right\rangle^{-1} \tag{2.7}$$

Often, the range of ions is approximated with the Bragg-Kleemann rule [2, 18]

$$R(E_0) = \alpha {E_0}^p. \tag{2.8}$$

Equation (2.8) is the first term of a Taylor expansion with E_0 as the ion's initial energy. α and p are empirical parameters.
As ions are slowed down almost continuously, with absorption processes being rather rare,

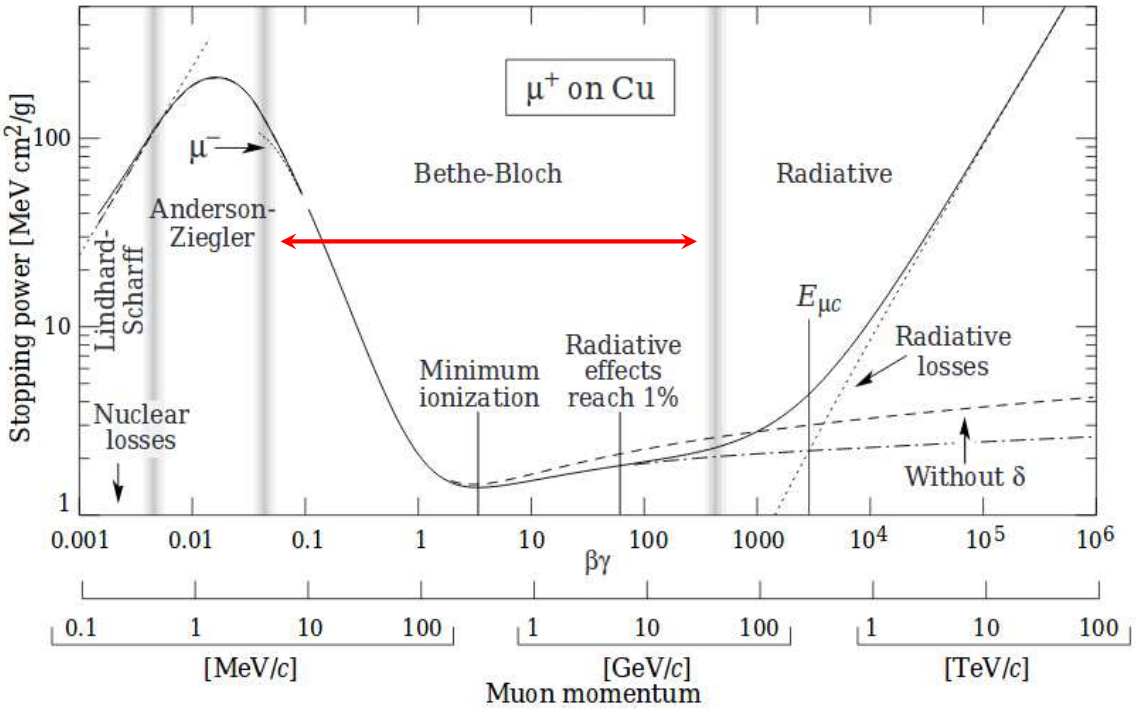

Figure 2.2: Stopping power as a function of energy for a muon in copper. The red arrow denotes the energy range where the Bethe-Bloch equation (2.6) gives a valid description [16].

the number of particles as a function of depth is almost constant, with a steep step down to zero at the mean range value. It is not an abrupt step though, but "smeared out" due to statistical fluctuations. These fluctuations are called *range straggling*. The range distribution can be described by a Gaussian function around the mean range value. Thus, the function of the number of ions per depth can be obtained by convolution of this Gaussian with a step function at the mean range. Figure 2.4 shows this function for heavy charged particles. As comparison, it is also shown for photons which predominantly interact via absorption processes. The number of photons as a function of depth shows an exponential decline.

2.2.6 Multiple Coulomb scattering

Ionisation and excitation processes are responsible for the energy loss of ions in matter. The path of the ion is interrupted by many small interactions. The direction, however, is not changed significantly, as electrons have a much lower mass. Direction variations are caused by elastic collisions of the ions with the material's nuclei. This is called multiple Coulomb scattering (MCS) and it's effect is larger at lower ion energies. High-energy ions pass through a material in a straighter line than low-energy ions.

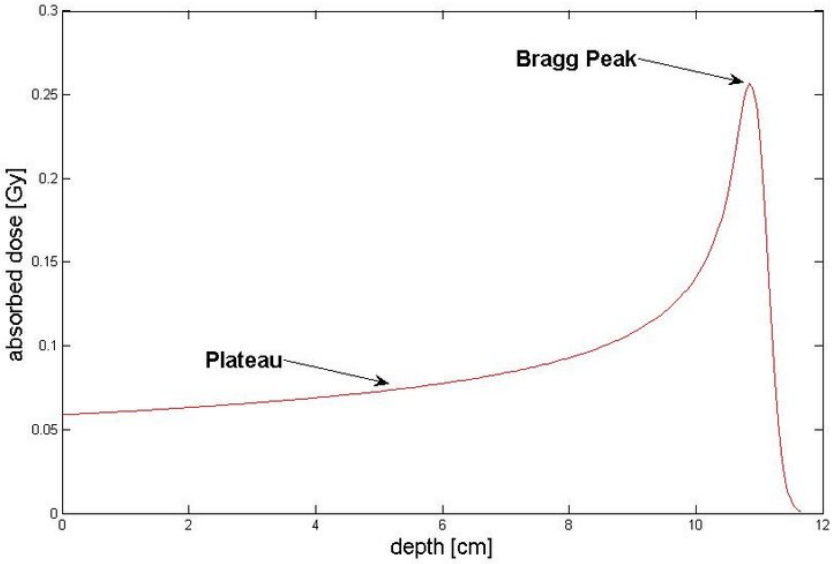

Figure 2.3: Energy deposition as a function of penetration depth for heavy charged particles shows the typical Bragg peak at the end of the path [17].

2.3 Particle showers

Very high-energy particles entering a material produce secondary particles with such high kinetic energies that these themselves are considered high-energy particles. They will in turn produce secondaries along their path through the material and so on. As a result, a cascade of particles is triggered, a so-called particle shower. The initial energy of the primary particle is distributed among the secondary particles and deposited in the material through these.
Depending on the type of primary particle, a shower can be either electromagnetic or hadronic. Electromagnetic showers are much more confined in space and simpler to describe, as there are fewer processes involved. Figure 2.5 shows the development of an electromagnetic and a hadronic shower in an equivalent block of material. Both showers are initiated by a particle with an energy of 100 GeV. In the top one it is an electron, in the bottom one a pion. It can clearly be seen that the electromagnetic shower is much more localised. Dense areas in the hadronic shower denote electromagnetic sub showers.

2.3.1 Electromagnetic particle showers

Electrons, positrons and photons interact only via the electromagnetic force. A shower initiated by one of these particle types will predominantly be an alternating series of bremsstrahlung and pair production. Both of these processes happen in the Coulomb field of the target nuclei.

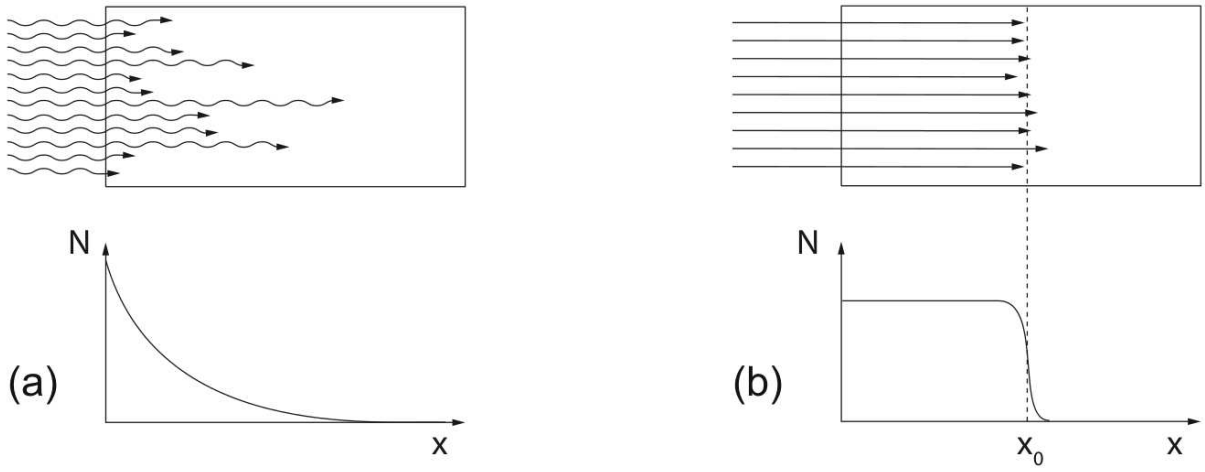

Figure 2.4: Number of particles as a function of depth into material for (a) photons and (b) heavy charged particles [13].

- Photons at high energies are most likely to interact via pair production (see Figure 2.1). The photon traversing the Coulomb field of the nucleus produces an electron positron pair while the photon itself is absorbed.
- The paths of electrons and positrons as light-weight particles are significantly influenced by the presence of nuclei. They are deflected in the Coulomb field and emit bremsstrahlung (high-energy photons) in the direction away from the nucleus.

Both processes' probability increases proportionally to the square of the atomic number Z of the target material, $\sigma \propto Z^2$. In high-Z materials, the probability of bremsstrahlung and pair production is significantly higher than in low-Z materials. Thus, showers will occur more easily in high-Z materials.
The geometric dimensions of the electromagnetic shower can be described with two quantities, the radiation length X_0 for the longitudinal and the Molière radius R_M for the lateral expanse. The radiation length is the distance after which the primary particle's energy has decreased to $1/e$ of the initial value E_0. The energy at the radiation length can be described as

$$E(X_0) = E_0 \frac{1}{e}. \tag{2.9}$$

This brings the energy as a function of depth x to

$$E(x) = E_0 \exp\left(-\frac{x}{X_0}\right). \tag{2.10}$$

The Molière radius can be calculated from critical energy E_c and radiation length X_0 as

$$R_{\mathrm{M}} = \frac{21}{E_{\mathrm{c}}} X_0. \tag{2.11}$$

A cylinder with radius R_{M} along the shower axis contains 90% of the deposited energy.

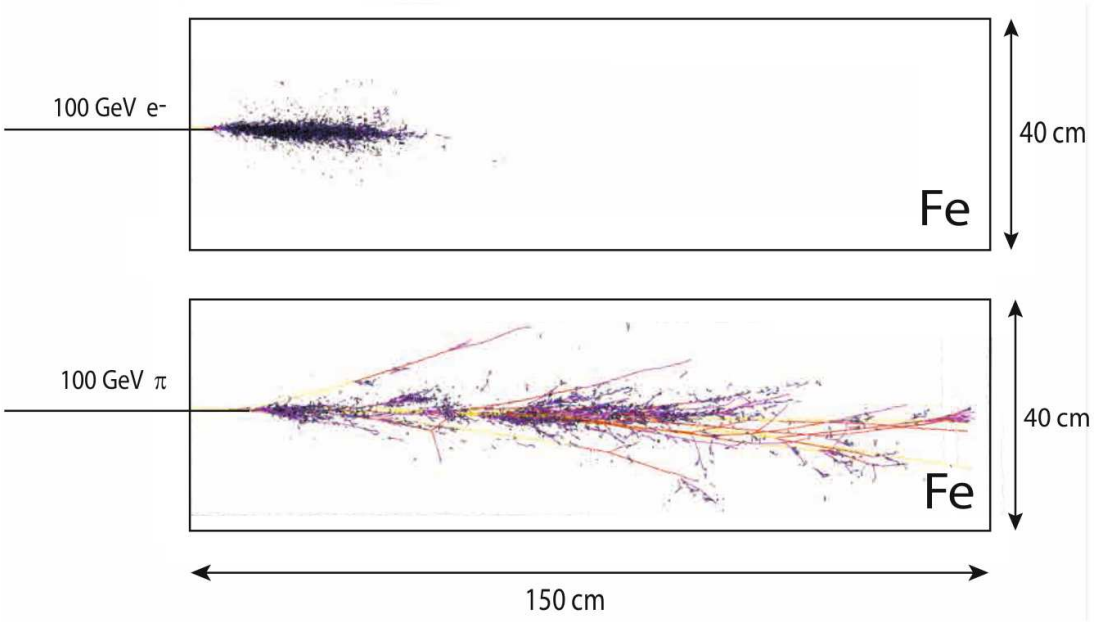

Figure 2.5: Comparison of electromagnetic shower at the top and hadronic shower at the bottom [13].

2.3.2 Hadronic particle showers

Hadronic showers are more complicated to analyse and describe than electromagnetic showers because hadrons have more possibilities to interact with the material. In addition to ionisation and excitation of atoms due to electromagnetic interaction with hull electrons and nuclei, also hadronic interactions with the nuclei have to be considered. When a high-energy hadron enters the material, it triggers a hadronic shower of secondary particles, much like the electromagnetic shower but with different underlying processes.
Nuclear processes mostly occur via inelastic interaction with only a single nucleon. During this interaction, many high-energy particles are produced, hadrons as well as electrons and photons. Interaction of these secondary particles with the other nucleons as they try to exit the nucleus leads to nuclear excitation. This extra energy can be released through spallation. The nucleus is fragmented into pieces which are emitted with energies in the order of 100 MeV to a few GeV. These high energies enable the fragments to trigger new spallations. Fragments include nuclei, ions and neutrons as well as gamma photons. Spallation occurs about 10^{-22} s after a hadron enters the primary nucleus. The highly excited nucleus left behind after the spallation process loses its extra energy via evaporation. It releases nuclear fragments and nucleons after 10^{-18} s with energies of a few MeV. All charged fragments, from spallation as well as evaporation, are highly ionising and have a short range which means they deposit most of their energy locally. If there are neutrons among the products, especially in high-Z materials, nuclear fission is possible.
Neutral pions can decay exclusively into electrons and photons. If there is a neutral pion

among the secondary particles, it will trigger an electromagnetic subshower within the hadronic shower. The total energy deposit of a hadron shower can be split into two parts, an electromagnetic component $f_{\text{em}}E$ and a hadronic component $f_{\text{h}}E$

$$E_{\text{dep}} = (f_{\text{em}} + f_{\text{h}}) \cdot E. \tag{2.12}$$

The probability for the creation of neutral pions grows with increasing energy. The electromagnetic component therefore also shows an energy dependency.

$$f_{\text{em}} \approx 1 - \left(\frac{E}{E_k}\right)^{k-1} \tag{2.13}$$

E_k and k are parameters which need to be extracted from data or simulation [13].
Analogously to electromagnetic showers, geometric properties can be described with some key values. The nuclear absorption length λ_a for hadronic showers takes the place of the radiation length X_0 for electromagnetic showers. It is defined as the length after which a fraction $\frac{1}{e}$ of the initial particles N_0 still exist

$$N(x) = N_0 \exp\left(-\frac{x}{\lambda_a}\right) \tag{2.14}$$

As the cross section for high-energy hadrons is only weakly dependent on the energy, the nuclear absorption length can be calculated as

$$\lambda_a = \frac{A}{N_A\,\rho\,\sigma_{\text{inel}}} \approx 35\,\text{g}\,\text{cm}^{-2}\frac{A^{\frac{1}{3}}}{\rho}. \tag{2.15}$$

A and ρ are the atomic number and density of the material, respectively. σ_{inel} is the cross section for inelastic scattering, N_A is the Avogadro constant. About 95% of the energy is deposited in a cylinder with radius λ_a around the shower axis. The relation of λ_a to X_0 depends on the material's atomic number Z and reads

$$\frac{\lambda_a}{X_0} \approx 0.37 \cdot Z. \tag{2.16}$$

For any $Z \geq 3$, $0.37 \cdot Z$ becomes larger than 1, making the nuclear radiation length λ_a larger than the radiation length X_0 (see Figure 2.5). The fraction $\frac{\lambda_a}{X_0}$ gets larger with increasing atomic number Z of the material. For most materials, a hadronic shower will be significantly larger than an electromagnetic shower. The difference grows with the atomic number Z of the material.

2.4 Calorimeters

Information in this chapter was taken from [13] and [19]. Calorimetry is the science of measuring the energy of high-energy particles. Calorimeters are detectors which fully absorb

the particle and its energy. The interaction of the particle with the detector material leads to a reaction that can be measured. Examples for such interactions are light production in scintillators or charge deposition through ionisation. The initial signal is converted into an electrical signal which is amplified and read out. The signal should be proportional to the deposited energy which is in turn proportional to the initial energy of the particle.

$$I_{\text{signal}} \propto E_{\text{dep}} \propto E_0 \tag{2.17}$$

The architecture of the calorimeter has to be optimised for the type of particle one wants to measure. Electromagnetic calorimeters detect particles that interact primarily via the electromagnetic force, i.e. electrons, positrons and photons. Hadronic calorimeters are, as the name suggests, made to detect hadrons. Hadrons are all particles which are made out of quarks and therefore interact via the strong force. Electromagnetic calorimeters are much more compact than hadronic ones. This is a result of the different shower properties. To stop a hadronic particle, the volume needs to be much bigger, see Figure 2.5 and Equation (2.16).

Calorimeters can also be distinguished by their construction type into homogeneous and sampling calorimeters, see Figure 2.6. In a homogeneous calorimeter, there is one volume in which the incoming particles are slowed down and detected. Sampling calorimeters consist of two different kinds of material. One is a detector which produces a signal upon particle passage, e.g. a scintillation event. The other one is an absorber (typically a high-Z material like Pb) which slows down the particles. This makes the calorimeter more compact but comes with the challenge that only a part of the deposited energy is measured. Analysis after the measurement is necessary to achieve the full energy deposit. Electromagnetic calorimeters exist both as homogeneous calorimeters and as sampling calorimeters. Hadronic calorimeters are always sampling calorimeters. This is the only way to make them compact enough for practical experimental use.

As discussed in Section 2.3.2, electromagnetic subshowers can be caused inside hadronic showers by neutral pions. This is a general problem for calorimetry as electromagnetically deposited energy results in a higher signal. In hadronic interactions, "hidden" energy deposition is possible, like the nuclear binding energy in spallation processes and the creation of muons and neutrinos which escape without interaction in the detector material. This energy can not be measured by the detector, falsely reducing the signal for purely hadronic shower components. To get the true energy deposit, the signal has to be corrected. This process is called compensation, and a calorimeter that produces equally high signals, no matter if the energy is deposited hadronically or electromagnetically is called a compensating calorimeter. There are a number of ways to achieve this, both in optimisation of hardware as well as software analysis of the signal after the measurement. See for example [13] for details.

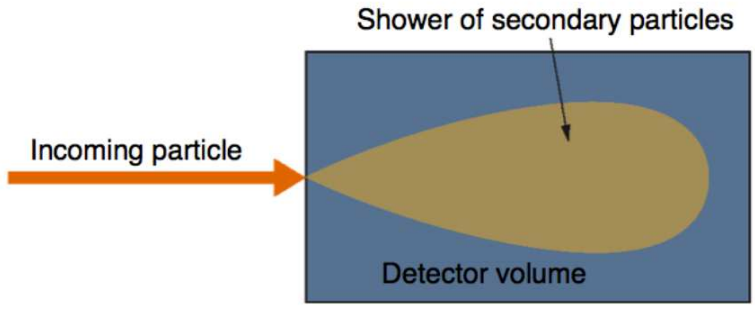

(a) Homogeneous calorimeter

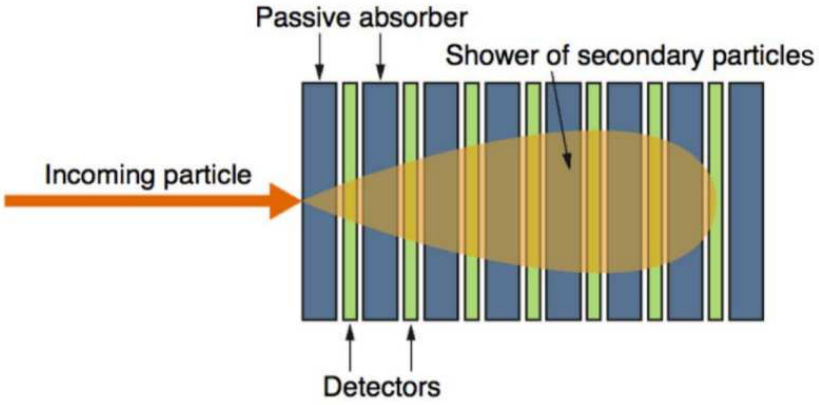

(b) Sampling calorimeter

Figure 2.6: Particle shower in (a) homogeneous and (b) sampling calorimeter [20].

2.4.1 Scintillators

Commonly used materials for the sensitive layer in calorimeters are scintillators. A scintillator is a material that emits light after being traversed by ionising radiation. The radiation deposits energy which leads to an excitation in the material, either atomic or in the crystal structure. This extra energy is then emitted again via photons, bringing the material back to the original state. Depending on the time gap Δt between arrival of radiation and light emission, the phenomenon has different names: prompt fluorescence ($\Delta t \approx$ ns), delayed fluorescence ($\Delta t \approx$ µs to ms) and phosphorescence ($\Delta t \approx$ ms).
There are two groups of scintillators, organic and inorganic. Here, the focus lies on organic scintillators as this is the type used in the experiment.
In inorganic scintillators, which are solid crystals, the absorption and emission spectra are determined by the energy bands due to the crystal structure. Absorption of ionising radiation can lift an electron into the higher-energy conduction band. When it jumps back down, the energy difference is emitted in form of a photon. Common inorganic scintillators are, e.g., thallium-doped sodium iodide (NaI(Tl)) and lead tungstate ($PbWO_4$). Inorganic scintillators show good energy resolution and are often used for gamma spectrometries. Due to their high density and short radiation length, they are well-suited for detection of high-energy photons and electrons. Inorganic crystals can be made very small. If arranged in an array, position sensitivity can be achieved. Disadvantages are their tendency to hygroscopy and relatively slow signal. Also, they are fragile to handle and it is not possible to cover large areas.

The scintillation mechanism of organic scintillators works on a molecular level. As they

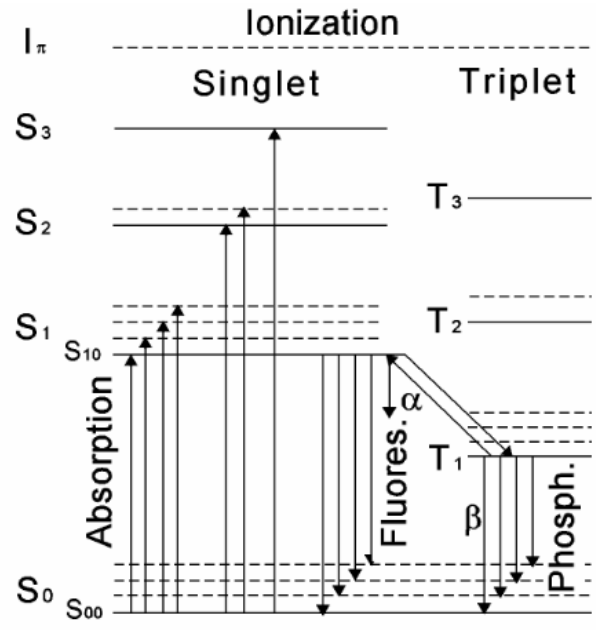

Figure 2.7: Electronic structure of the carbon atom and possible transitions [21].

are all hydrocarbons, the scintillation properties are mainly determined by the electronic structure of the π electrons in bound carbon atoms which is shown in Figure 2.7. Ionising radiation lifts electrons from the ground state S_{00} into one of the excited states S_{1i}, S_{2i}, S_{3i},... After a few picoseconds, they change from S_{ji} to S_{10} without radiation emission via vibrational relaxation. The following de-excitation back to S_{00} leads to the emission of a photon with characteristic wavelength. There are two ways this can happen. Either directly, at the time scale of nanoseconds as fluorescence, from S_{10} to S_{0i}. Another possibility is a radiation-less transition into the triplet state T_1 with a following relaxation into S_{0i} at the microsecond scale (phosphorescence). This slower process is not wanted and can be suppressed by making the material as pure as possible. Then, the scintillation process is very fast, making organic scintillators suitable for timing applications.

The emission wavelength is always longer than the absorption wavelength, as can be seen

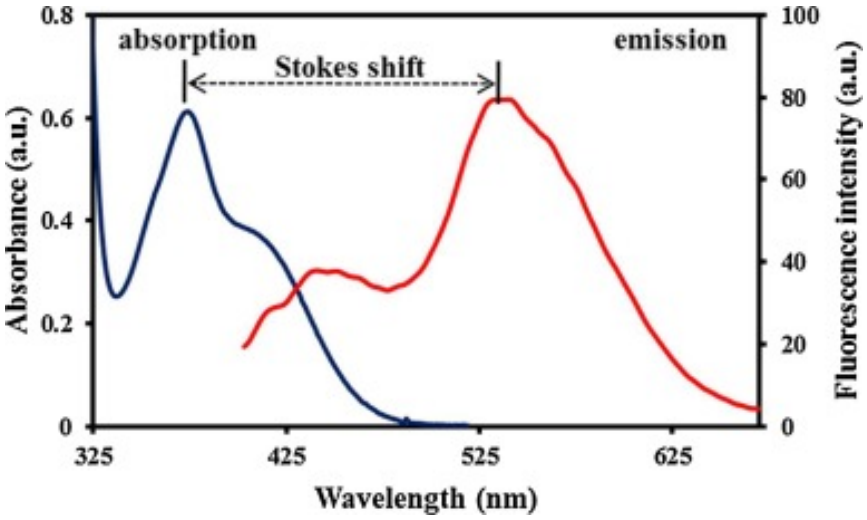

Figure 2.8: The difference between the maxima of absorption and emission spectrum of a scintillator is called Stokes shift [22].

from the lengths of the arrows between the energy levels in Figure 2.7. Arrows pointing up, corresponding to excitation, are all longer than the ones pointing down, which symbolise de-excitation. This difference is called *Stokes shift*. It is defined as the difference in energy of the maxima of absorption and emission spectrum, see Figure 2.8. The Stokes shift is an important property for scintillators which need to be transparent to their own emission light. If absorption and emission spectrum overlap, scintillation light in that wavelength region is reabsorbed before it can be detected. Often, the Stokes shift of the scintillator is too small to completely prevent absorption and emission spectrum from overlapping. A wavelength shifting (WLS) material can be added in concentrations of typically $\approx 1\%$ to achieve this goal. The WLS material is another scintillator with a large Stokes shift and an absorption spectrum that matches the emission spectrum of the initial scintillator. Another advantage of a larger emission wavelength is the generally better efficiency of photomultipliers in that region.

Organic scintillators are available as liquids or solids. Solid organic scintillators are called plastic scintillators. They are manufactured via polymerization of a liquid base in which a scintillator is dissolved. The two most common bases are polyvinyltoluene (PVT) and polystyrene (PS). Both materials scintillate by themselves under ionising radiation but the light yield and transparency are very low. Therefore, a fluor is added. Plastic scintillators are relatively cheap and can be machined into almost any shape, see Figure 2.9. They are easy to handle which makes them popular in particle physics applications. Due to the short decay time, they can be used for triggering and time of flight measurements.

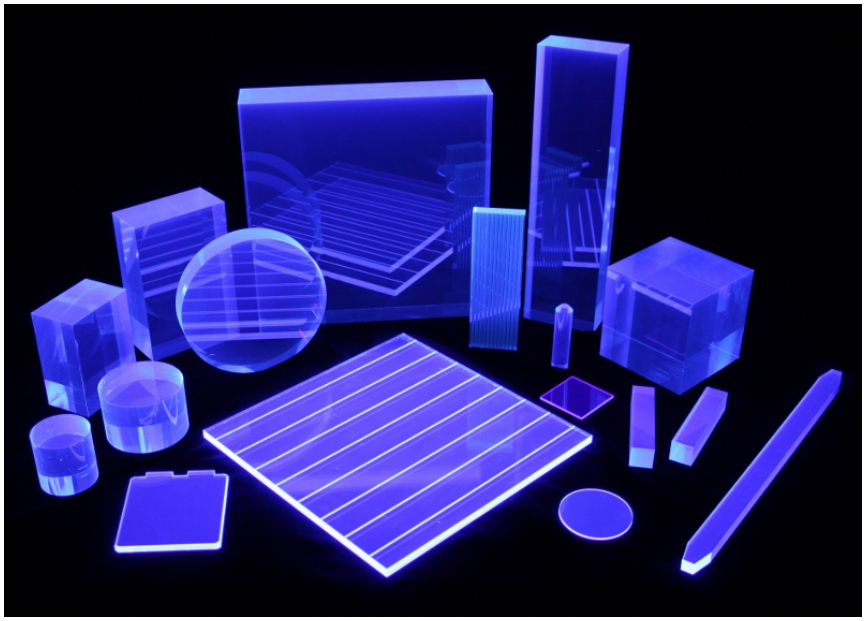

Figure 2.9: Commercially available plastic scintillators [23].

2.4.2 Silicon photomultipliers

Scintillators as radiation detectors give a signal in form of light, i.e. photons. These photons have to be converted into an electrical signal in order to work with it. The typical device for photon detection is a photomultiplier tube (PMT). A PMT contains a photocathode where electrons are produced by incoming photons via the photoelectric effect. These electrons are then multiplied in an array of dynodes and collected at the anode. Between each two neighbouring dynodes, an electric field accelerates the electrons towards the next dynode. Further secondary electrons are produced, which increase the signal. One big disadvantage of photomultiplier tubes is that they are sensitive to magnetic fields. This is the main reason for the choice of silicon photomultipliers instead of PMTs for readout in many medical applications.

To explain the concept of a silicon photomultiplier (SiPM), we have to start with the photodiode. A photodiode is a semiconductor device which produces an electric signal when

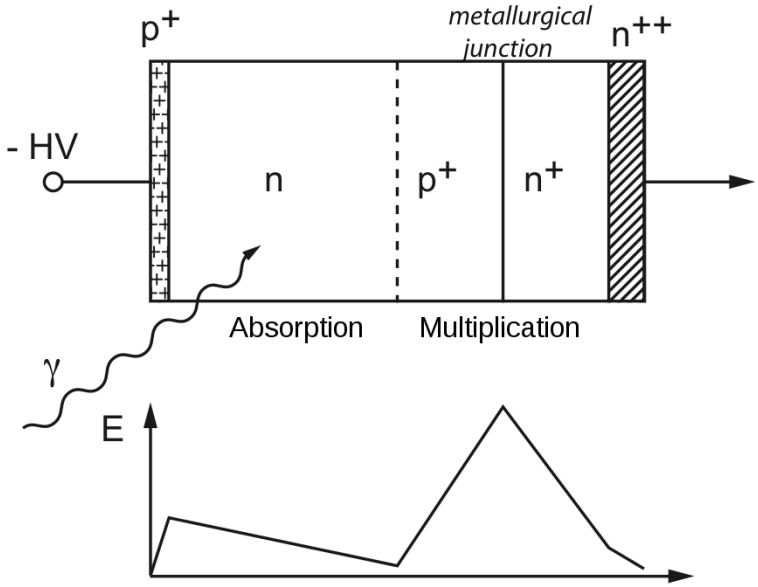

Figure 2.10: Layout and electric field of a single photon avalanche diode [13].

hit with light. In order to operate, it has to be provided with reverse bias voltage. A special modification of a photodiode is the single photon avalanche diode (SPAD). As the name suggests, SPADs are able to create a signal for single photons traversing their material. A schematic drawing of the SPAD architecture is shown in Figure 2.10. The material is doped in a way to create two zones: a broad low-field region and a thin high-field region. Photons are absorbed in the large volume of the low-field region and produce photoelectrons which drift into the high-field region. There, they are accelerated and create secondary electrons. They cause an avalanche of electrons being released towards the anode, inducing an electric readout signal. This intrinsic amplification makes the energy deposition of a single photon detectable. During the avalanche, the detector volume is "blind" for other photons reaching the material. This so-called dead time is typically in the order of nanoseconds which is acceptable for most applications. The bias voltage has to be about 10-15% above the breakdown voltage to enable single photon detection.
In order to create a SiPM, many SPADs are arranged in an array to create a larger detection area. Each one of these SPAD pixels has an area of about $50\,\mu m \times 50\,\mu m$, the whole SiPM comes to $\approx 1\,mm^2$. In this configuration, the sensitivity is increased as the dead time of one SPAD effects only a small part of the detection area. A photon hitting the neighbouring SPAD will still be detected. SiPMs show good linearity but the signal is temperature dependent. Cooling is therefore necessary. This also helps reduce the relatively high noise.

2.5 Proton computed tomography

Before a patient can be treated with ion therapy, a treatment plan has to be made in which all parameters for the irradiation have to be decided. Beam energy, intensity and irradiation time have to be set as well as the angle between beam and patient. Currently, x-ray computed tomography images serve as a basis for this treatment plan. A computed tomography is obtained from a series of 2D projection images taken at different angles which are combined by a reconstruction algorithm to give a 3D image.
In an x-ray image, the contrast results from differences in intensity of the x-ray beam after traversing the patient [11]. The intensity $I(z)$ of an x-ray beam with initial intensity I_0 after travelling a distance z in a material is attenuated according to

$$I(z) = I_0 \exp(-\mu z), \tag{2.18}$$

see Section 2.1. μ is the linear attenuation coefficient which depends on the material. For each projection, an intensity map $I(x, y, z = z_{\text{projection}})$ at the z-position of the detector is measured from which μ is retrieved. To be able to judge the radiodensity of a material, the attenuation coefficient is converted into Hounsfield units (HUs). The HU scale is oriented at the linear attenuation coefficients of water and air. $\mu_{\text{water}} = 0\,\text{HU}$, $\mu_{\text{air}} = -1000\,\text{HU}$. Therefore, the general conversion for any material is [24]

$$1\,\text{HU} = 1000\frac{\mu - \mu_{\text{water}}}{\mu_{\text{water}} - \mu_{\text{air}}}. \tag{2.19}$$

This is the quantity that can be read out of an x-ray CT. For ion therapy treatment planning, however, a stopping power map of the patient is needed in the tumour region of the body. Therefore, HUs are converted to SP values [7]. The conversion function is dependent on the tissue, see Figure 2.11. It introduces errors in the SP map that can be as large as several millimetres [26]. Any error leads to compromises in the treatment plan, as irradiation of sensitive regions has to be avoided. Irradiation margins have to be made smaller than the actual tumour region to make sure no harm is done outside. This decreases the effectiveness of the therapy as parts of the tumour will remain unirradiated. Ion therapy is especially sensitive to such errors because of the very localised energy deposition at the Bragg peak position. A shift of the Bragg peak in the order of millimetres can mean that the majority of the energy is deposited in healthy tissue instead of the tumour region.
A way to avoid errors from conversion is to measure the stopping power directly. That is, create the CT basis for treatment planning with the same particles used for irradiation, in our case protons [27]. The basic setup for a proton computed tomography (pCT) is shown in Figure 2.12. In the middle, there is the phantom, the object to be scanned. It can be rotated around its vertical axis. There is a tracking detector system both before and after the phantom. At the very end, an energy detector is placed. The proton beam comes from the left, first traversing the front tracking system, then the phantom, the rear tracking system and finally, it is absorbed in the energy detector.
The tracking systems each consist of at least two position sensitive detectors. Each detector

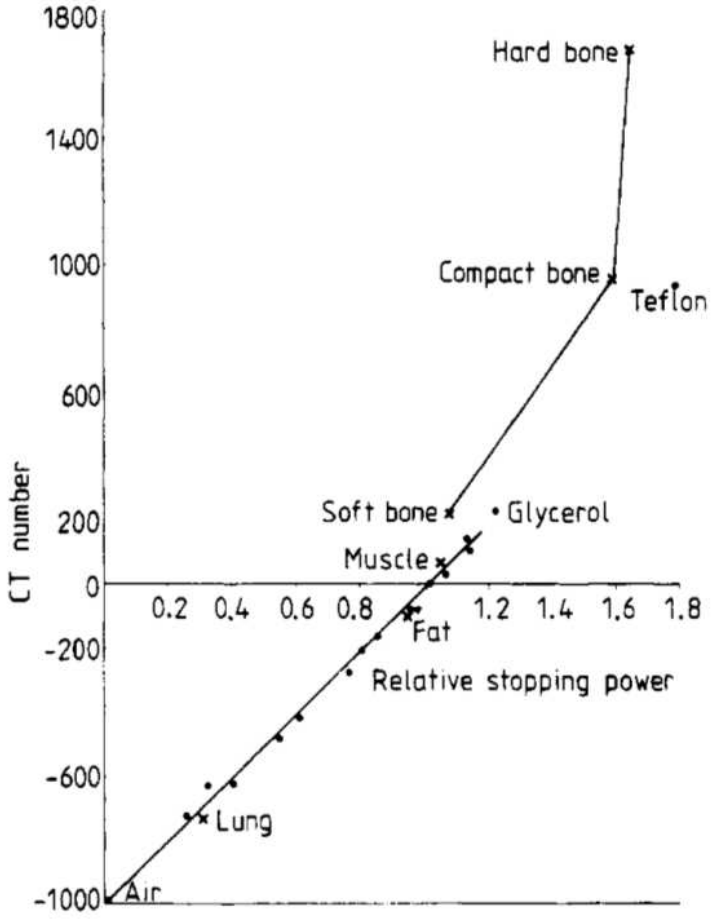

Figure 2.11: Relation of stopping power to Hounsfield unit values [25]. Different linear relations exist for different regions, dependent on the material.

gives a 2D particle position in the detector plane. From these, the momentum direction as well as entry and exit positions into and out of the phantom can be obtained. This information is necessary to estimate the path travelled by the proton inside the phantom. At the end of the setup, the remaining energy of the proton is measured. As the initial energy of the proton is known, its energy loss can be calculated. From the path estimation and the energy loss, the stopping power can be obtained using the tomographic equation (see Section 2.5.1) and a reconstruction algorithm. The energy measurement can be done, for example, with a calorimeter or a time of flight (TOF) setup.

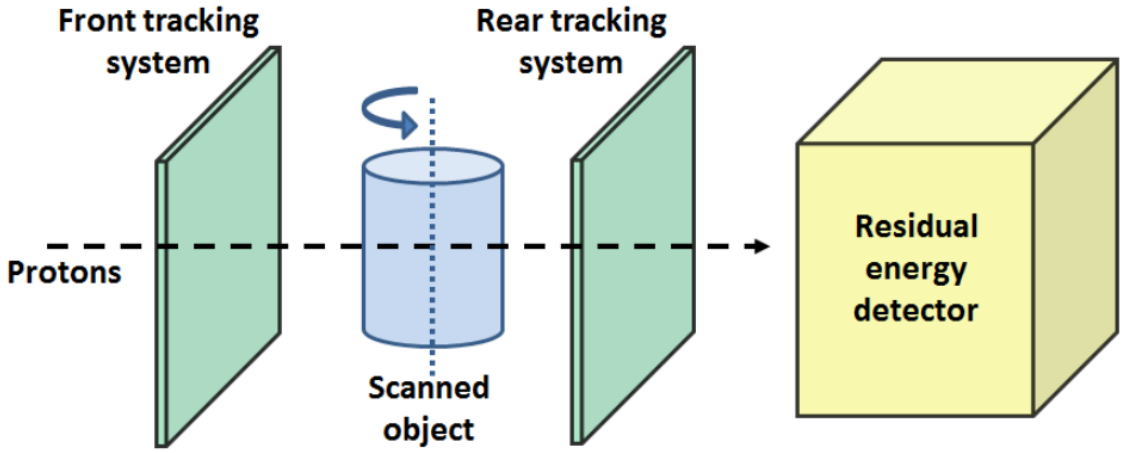

Figure 2.12: General setup of a pCT: Tracking system before and after the phantom; residual energy detector at the end [24]. Each tracking system consists of at least two position sensitive detectors.

2.5.1 Tomographic equation

The quantity required for proton therapy treatment planning is the stopping power

$$S = -\frac{dE}{dl}. \tag{2.20}$$

The SP can not be measured directly. The following derivation of the tomographic equation is taken from [28] and [29].
Under the continuous slowing-down approximation (CSDA), one can turn (2.20) into

$$-dE = S(\vec{r}, E)dl, \tag{2.21}$$

where E is the particle energy, $\vec{r} = (x, y, z)$ is an arbitrary position in the reconstruction plane and dl is an infinitesimal path segment along which the particle loses the infinitesimal energy dE. Often, the stopping power is given as mass stopping power $\frac{S}{\rho}$ which will be introduced here as well. If Equation (2.21) is extended by the mass stopping power at a specific energy $\tilde{E}$, one gets

$$-\frac{S(\vec{r}, \tilde{E})}{\rho(\vec{r})}dE = \frac{S(\vec{r}, \tilde{E})}{\rho(\vec{r})}\frac{S(\vec{r}, E)}{\rho(\vec{r})}\rho(\vec{r})dl. \tag{2.22}$$

Dividing by the mass SP at energy E gives

$$-\frac{\frac{S(\vec{r}, \tilde{E})}{\rho(\vec{r})}}{\frac{S(\vec{r}, E)}{\rho(\vec{r})}}dE = S(\vec{r}, \tilde{E})dl. \tag{2.23}$$

For better readability, a shorter notation is introduced for the fraction on the left hand side:

$$\frac{\frac{S(\vec{r},\tilde{E})}{\rho(\vec{r})}}{\frac{S(\vec{r},E)}{\rho(\vec{r})}} = \left[\frac{S}{\rho}(\vec{r})\right]_E^{\tilde{E}}. \tag{2.24}$$

This fraction shows only a weak dependency on the material. For the two tissues with minimal and maximal density in the human body, the difference in value of the fraction is less than 0.6% (for energies in the clinical range) [28]. Hence, a well-known material can be assumed, like water

$$\left[\frac{S}{\rho}(\vec{r})\right]_E^{\tilde{E}} \cong \left[\frac{S}{\rho}(\mathrm{H_2O})\right]_E^{\tilde{E}}, \tag{2.25}$$

leading to

$$-\left[\frac{S}{\rho}(\mathrm{H_2O})\right]_E^{\tilde{E}} dE = S(\vec{r},\tilde{E})dl. \tag{2.26}$$

Now the left hand side of the equation is not dependent on the spatial coordinates anymore but only on the energy. This helps in the next step as both sides are integrated

$$-\int_{E_{\mathrm{in}}}^{E_{\mathrm{out}}} \left[\frac{S}{\rho}(\mathrm{H_2O})\right]_E^{\tilde{E}} dE = \int_{\mathrm{path}} S(\vec{r},\tilde{E})dl. \tag{2.27}$$

The left hand side is only dependent on the arbitrary energy $\tilde{E}$ if the energies E_{in} and E_{out} of the particle before and after traversing the target are known. The right hand side depends on the path that the proton travels. Dividing the phantom into N voxels turns the integral into a sum

$$p_i = -\int_{E_{\mathrm{in}}}^{E_{\mathrm{out}}} \left[\frac{S}{\rho}(\mathrm{H_2O})\right]_E^{\tilde{E}} dE = \sum_{j=1}^{N} w_{ij} S_j(\tilde{E}). \tag{2.28}$$

w_{ij} is the distance travelled by proton i in voxel j, $S_j(\tilde{E})$ is its stopping power in voxel j at energy $\tilde{E}$. From a series of M protons, one gets a set of M equations

$$p_1 = w_{11}S_1 + w_{12}S_2 + \cdots + w_{1N}S_N, \tag{2.29}$$

$$p_2 = w_{21}S_1 + w_{12}S_2 + \cdots + w_{1N}S_N, \tag{2.30}$$

$$\vdots$$

$$p_M = w_{M1}S_1 + w_{M2}S_2 + \cdots + w_{MN}S_N \tag{2.31}$$

for the stopping power values S_j at energy $\tilde{E}$. One proton will traverse a limited number of voxels, therefore it will contribute only to the corresponding SP values in those voxels. There is a minimum number of protons needed to get at least one value for each S_j. Ideally, more than one value exists for each voxel. If this is the case, statistical values like the mean can be used which will improve the result. However, more data means more particles, which comes with a higher dose for the patient. Careful consideration is necessary to find an acceptable balance.

3 Materials and methods

3.1 MedAustron

MedAustron is an ion therapy center south of Vienna, near the town Wiener Neustadt. An overview picture of the center can be seen in Figure 3.1. The building process was completed in 2011, the first patient was treated in December 2016. The main goal at MedAustron is to offer ion therapy to cancer patients. But as there are still many open questions and room for improvement in this field, research is also part of the agenda. During weekdays, the beam is used for patient treatment. In the night and on weekends however, various research groups, mainly from TU Wien and MedUni Wien, have the possibility to conduct their experiments in non-clinical research fields [30].

The accelerator complex was developed in close collaboration with CERN, based on the PIMMS study [32–34]. It is of synchrotron type with a circumference of about 77.4 m. It is able to accelerate protons to energies in the range of 60 MeV to 800 MeV and Carbon ions from 120 MeV/u to 400 MeV/u. Electron Cyclotron Resonance ion sources provide H_3^+ ions or $^{12}C^{4+}$ ions by creation of a plasma and subsequent separation from electrons by an electric field. The ions are led into a linear accelerator which will accelerate them to 7 MeV/u, as synchrotrons are not able to accelerate particles from rest. The pre-accelerated particles are fed into the synchrotron where they are further accelerated. A synchrotron is basically a big ring where particles are sent around in circles. The acceleration itself happens only along a short part of the ring in radio frequency (RF) cavities (blue in Figure 3.1). These are closed metal pipes in which standing electromagnetic waves are built up. The electromagnetic field in these cavities accelerates passing charged particles. Strong magnets along the ring make sure the particles stay on the desired orbit. Dipole magnets (green in Figure 3.1) deflect, and quadrupole magnets (red in Figure 3.1) focus the beam. The magnets' strength has to be increased with every round as the particles' energy increases. When the particles have achieved the desired energy, deflective magnets extract the beam from the synchrotron and lead it into irradiation rooms.

MedAustron has four irradiation rooms, IR1 to IR4. IR3 is a treatment room for horizontal irradiation, IR2 for both horizontal and vertical irradiation. In IR4, a gantry will be available to irradiate from various angles. Room IR1 has the same layout as IR3 but is reserved exclusively for non-clinical research. This has the advantage of being able to prepare before and clear away after the beam time without having to worry about getting the room back to clinical conditions. In IR1 to IR3, both protons and carbon ions will be

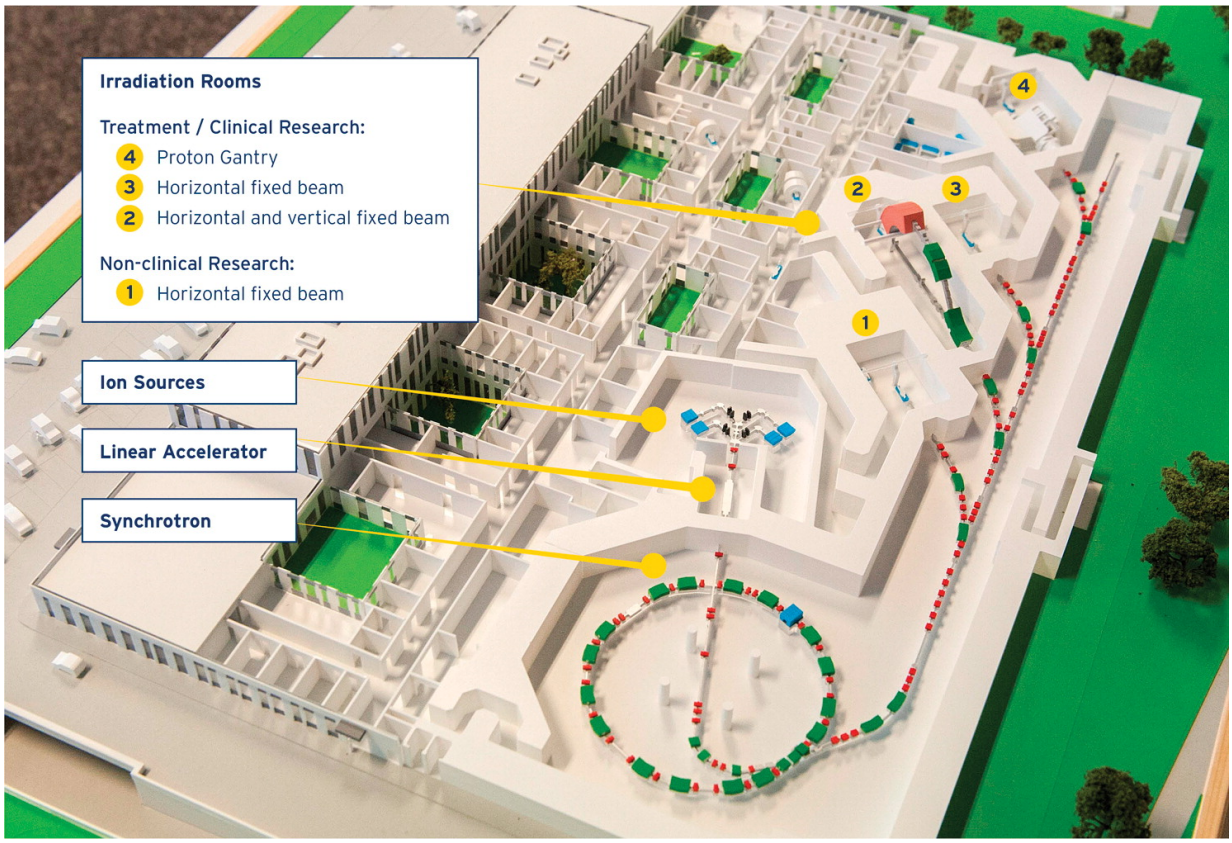

Figure 3.1: Outline of the accelerator complex and irradiation rooms at MedAustron [31].

available. The gantry in IR4 will only be operated with protons.

3.2 Experimental pCT setup at MedAustron

The basic setup for a pCT consists of two tracking systems and one energy measurement system, see Figure 2.12. The tracking systems are placed one before and one behind the phantom. Each tracking system consists of at least two position sensitive detectors. In the experimental setup at MedAustron, each tracking detector is a double-sided silicon strip detector module. The sensors have an active area of 2.56 cm × 2.56 cm. They are approximately 300 µm thick. The strips are orthogonal and have a pitch of 50 µm in the horizontal and 100 µm in the vertical direction. They are connected to APV25 chips via wire-bonds and read out by a VME-based system built for the Belle II experiment. A picture of one of the modules can be seen in Figure 3.3. The trigger signal is provided by two plastic scintillators. For more details, see [35].
At the very end of the setup, the residual energy must be measured. This can be done, e.g., with a calorimeter or a time of flight apparatus. This energy measurement part is not yet implemented at MedAustron. One possibility is to use the PRR30, a calorimeter

provided to the research group. The design of this calorimeter is described in detail in the next section 3.2.1.

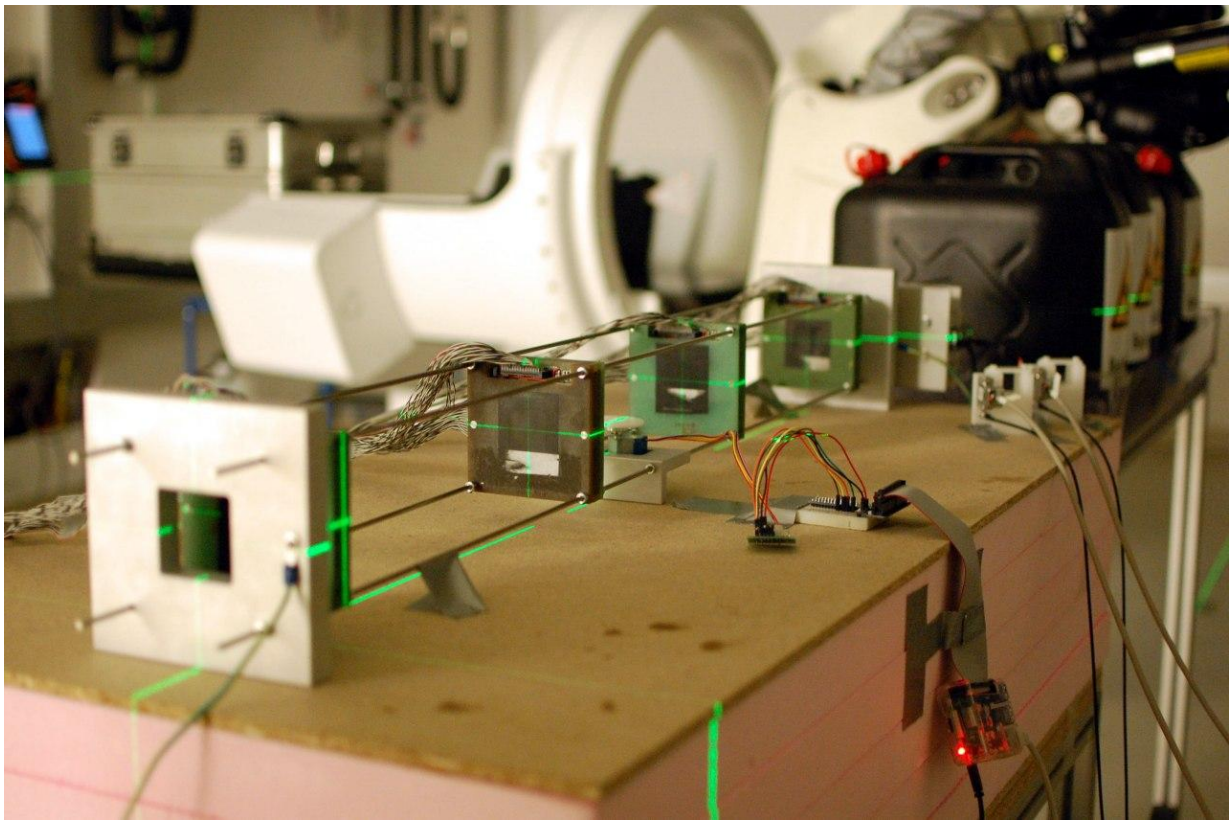

Figure 3.2: pCT setup at MedAustron [36]. Four modules with double-sided silicon strip detectors. Between the inner two is a round table for the phantom which can be rotated. The two white cables at the end are connected to the trigger scintillators. The green laser light is used to help with positioning.

3.2.1 TERA calorimeter

The calorimeter simulated for this thesis was built by the TERA foundation [37–39]. It is called PRR30 [40] and is a further development of the smaller prototype PRT10 [41]. The PRR30 is a scintillator based calorimeter. The basic structure can be seen in Figure 3.4. It consists of 50 plastic scintillator slabs, read out by SiPMs. The first two scintillators are intended for triggering, the remaining 48 make up the range telescope.
Each scintillator slab has an area of 30 cm × 30 cm and a thickness of 3 mm. They are arranged parallel one after another with a distance of 5 mm. The scintillator material is polyvinyltoluene, type BC-408 from Saint Gobain Crystals [43]. Its emission peak is at 425 nm. To prevent light from escaping, each scintillator is wrapped in 20 µm thick Aluminium foil. Another layer of 106 µm thick black paper is used to keep ambient light

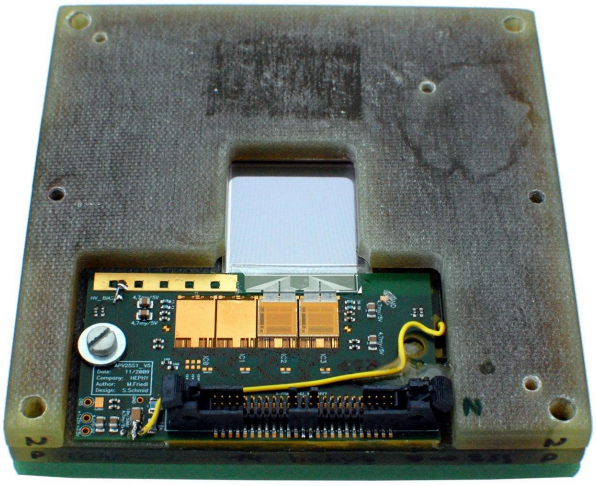

Figure 3.3: Tracker module with double-sided silicon strip detector [36].

out. Coupling to the SiPM is achieved with a wavelength shifting fiber. This fiber matches BC-408 perfectly as it has its absorption maximum at 425 nm. The fiber is glued to the scintillator slabs in a small groove along one of their edges. In front of the scintillators there is a possibility to place two gas electron multipliers [44] to record the position of incoming particles.

3.3 Monte Carlo method

The Monte Carlo method is a widely used numerical algorithm. Its significant feature is the use of random numbers. In most use-cases, there is a complex macroscopic problem which is very expensive to solve arithmetically, or is even unsolvable. The microscopic laws of such a problem are often known. The idea is to split up the macroscopic problem into many small, microscopic steps which, each on its own, can be easily solved. The microscopic results are then combined to achieve the macroscopic solution.
In this work, the macroscopic question is the signal in a calorimeter when bombarded with a certain amount of primary protons. This is split into the transportation of each particle through the geometry. The particle's path is divided into steps through the volumes which are interrupted by interactions with the target material. These interactions change the properties of the particle. Decisions on the length of a step and what kind of interaction will occur are made by use of random numbers in the following way [45].
Assume n possible events

$$E_1, E_2, E_3, ..., E_n \tag{3.1}$$

with respective probabilities

$$p_1, p_2, p_3, ..., p_n, \tag{3.2}$$

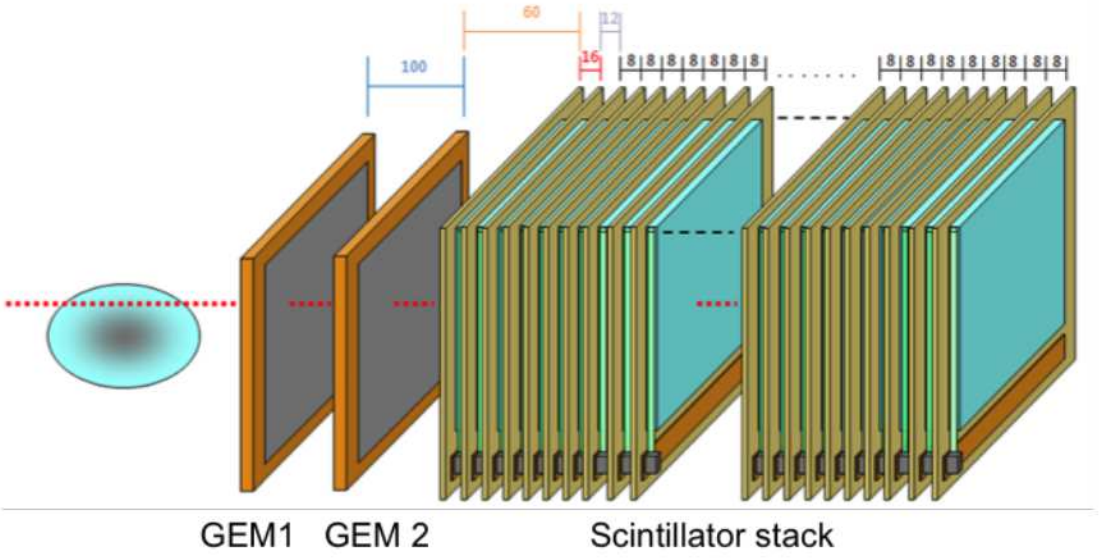

Figure 3.4: Layout of the TERA calorimeter PRR30 [42].

where

$$\sum_{i=1}^{n} p_i = 1. \tag{3.3}$$

A random number $\xi \in [0, 1)$ can be used to choose an event E_i according to

$$p_1 + p_2 + ... + p_{i-1} < \xi < p_1 + p_2 + ... + p_i. \tag{3.4}$$

In our example of particle transport in matter, E_i is one of all the possible interactions. The probability of an interaction is determined by its cross section.
Geant4 is a so-called mixed Monte Carlo. There is an energy threshold W_0 which determines how detailed the simulation is done. If the energy loss in a process ΔE is larger than the threshold, i.e. $\Delta E > W_0$, then the process is simulated in detail. All processes with $\Delta E < W_0$ are simulated cumulatively via statistical data. The threshold can be set by the user.

3.4 The Geant4 toolkit

Geant4 (GEometry ANd Tracking) is a big and versatile Monte Carlo simulation toolkit [12]. It was developed at CERN. Written in C++, it exploits the possibilities of object-oriented programming. This leads to a very modular and flexible design, making it useful in many different fields. Some examples of use are detector development and accelerator design (e.g. at CERN), medical applications like dose calculations and radiation hardness studies in astrophysics. As Geant4 is a toolkit, not a program, it is not possible to use

Figure 3.5: The TERA calorimeter PRR30. The large copper-colored part in the front is one of the GEMs. The scintillators can be seen to the left [42].

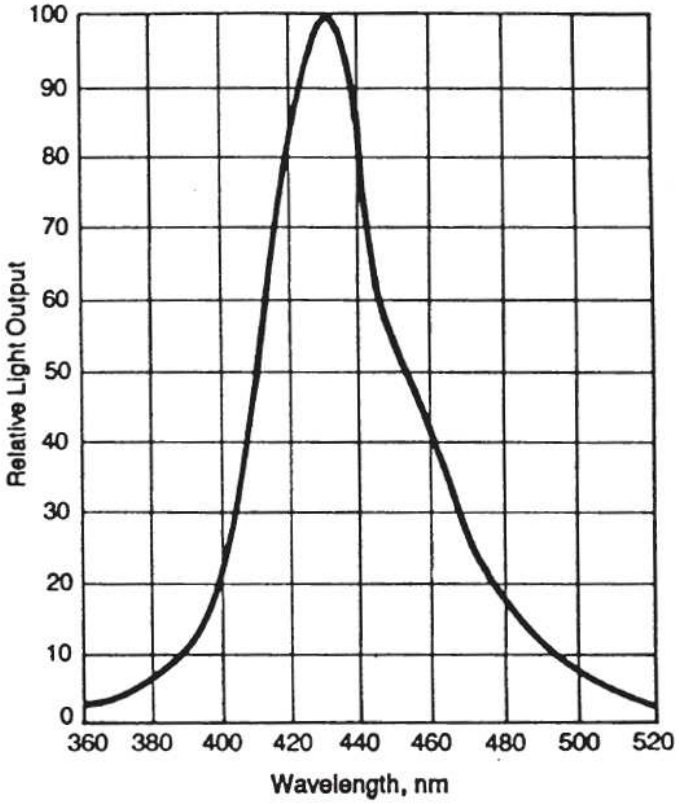

Figure 3.6: Emission spectrum of scintillator BC-408 [43].

Geant4 "out of the box" with default settings. Instead, the user has to build his/her own program, using only those of the many available classes and methods which are relevant to the respective case.
First, a short explanation of the principle of the Monte Carlo method is provided. In the following sections, an overview of the most important Geant4 classes is given. For more detailed information, refer to [12] and [46]. Recent developments and new publications can be found on the homepage [47].

3.4.1 Procedural structure

Run

The largest entity of the Geant4 procedure is the run, represented by the class `G4Run`. A run is a collection of events. During a run one is not to change the geometry and physics of the application. A run is started with the command `beamOn` (analogously to real-life particle physics experiments) and stops when all events are processed. The `G4RunManager` controls the run and manages the event loop within a run as well as all other major manager classes. It should be constructed in `main` and all user initializations have to be registered to it.

Event

The event is represented by the class `G4Event`. An event consists of one primary particle and everything that happens with and because of it. That means, secondary particles, deceleration, reactions in the target material etc. Event processing is done via three stacks, *urgent*, *waiting* and *postpone to next event*. During an event, new tracks (secondary particles) are pushed onto the stacks and then processed on a first-in-last-out basis. The user can decide on some tracks to be pushed onto, e.g., the *postpone to the next event* stack in order to only deal with currently relevant information.

Track

`G4Track` stores all current information about a particle travelling through the geometry (current position, volume, velocity etc.). It is often compared to a "snapshot" of the particle. It has access to further information through the pointers to `G4DynamicParticle` and `G4ParticleDefinition`. `G4DynamicParticle` contains properties of the moving particle (energy, momentum direction, polarization etc.). `G4ParticleDefinition` contains all 'static' information (mass, charge etc.). Track information can only be changed by a process.

Step

The step is the smallest unit of the simulation. It is represented by the class `G4Step`. `G4Step` contains delta information about the step, like `TotalEnergyDeposit`, as well as

pointers to its end points and `G4Track`. Through the end points `G4PreStepPoint` and `G4PostStepPoint`, volume information can be accessed. A particle is transported through the geometry via steps. Each particle type contains a list of processes it may undergo. Depending on the chosen physics, only those processes relevant for the current case are attached. Processes are divided into three categories, depending on when they take effect: *AtRest*, *continuous* and *discrete*. *AtRest* processes are invoked only for particles with zero kinetic energy. For moving particles, there are *continuous* and *discrete* processes. At the beginning of a step, each process proposes a step length to the `G4SteppingManager` which depends on the probability of the interaction, based on its cross section. The process manager chooses the process with the smallest step length which is then carried out. First *continuous*, then *discrete* processes are invoked and track properties are updated accordingly. Any secondary particles are stored in `SecondaryList`. If a process has slowed the particle down to zero kinetic energy, *AtRest* processes are invoked in the next step. Here as well step lengths are proposed, but in contrast to processes for moving particles, *AtRest* processes propose step lengths in time rather than space.
A step is also confined by the geometry. It is not allowed to traverse a volume boundary. If a step reaches a volume boundary, it ends there. The `PostStepPoint` lies on the boundary and logically belongs to the volume beyond the boundary. A new step is started in this volume. The `PreStepPoint` of this new step has the same coordinates as at the `PostStepPoint` of the former step.
There is a possibility to customize the stepping behaviour with the class `G4UserSteppingAction`, for example to kill certain tracks if they are not important to the application.

3.4.2 Mandatory user classes

The minimal requirements for a Geant4 application are the description of the geometry, primary particles and physics models. Three user initialization classes need to be registered directly to the run manager with the method `G4RunManager::SetUserInitialization()`.

- `DetectorConstruction` describes the geometry of the detector, materials, electromagnetic fields (if present) as well as the sensitive regions used for data acquisition. There is a hierarchical structure of three stages for any volume. `G4Solid` represents the geometrical shape. There are preconfigured classes for most common shapes, like `G4Box` or `G4Sphere`. It is also possible to create more complicated shapes through Boolean combination. From the solid and a `G4Material`, one can construct a `G4LogicalVolume`. In the third stage, `G4PhysicalVolume` is the placement of a logical volume in a so-called mother logical volume. The first constructed volume which must contain all other volumes is called the world.

- In `PhysicsList`, all physics that should be considered in the simulation must be listed. This means, all particle types must be registered together with all their processes of interaction. This can be done by creating a custom class inherited from `G4PhysicsList` where every particle type and interaction is listed, one by one. On

the other hand, Geant4 provides a number of ready-to-use physics lists from which one can choose the most suitable.

- `ActionInitialization` is the third user initialization class where all user action classes must be registered. One user action class is mandatory, namely the one to describe the primary particles, which is derived from `G4VUserPrimaryGeneratorAction`. The other five user action classes are optional. They are listed in Section 3.4.3.

3.4.3 Optional user classes

The six user action classes are possibilities for the user to control the simulation during a run. For each, Geant4 provides a virtual base class from which the user can derive their own action class and override desired methods. Following base classes exist:

- `G4UserRunAction`
- `G4UserEventAction`
- `G4UserStackingAction`
- `G4UserTrackingAction`
- `G4UserSteppingAction`

Typical usages are the creation of histograms, analyses at the end of a run or event, saving information, writing to histograms. `G4UserStackingAction` can be used to influence the order in which tracks are processed. The user can decide to prioritize, postpone or even kill a track.

3.4.4 Data acquisition

With only the mandatory classes, the application will run but will not store and show any data. For the goal of any experiment, whether real-life or in form of a simulation, to acquire data and see results, additional parts of the toolkit must be used. The key classes for this purpose are `G4VHit` and `G4VSensitiveDetector`.
`G4VHit` is a base class from which the user must derive their own concrete hit class. For each piece of information to store, there should exist a data member in the hit class, together with a `Set` and a `Get` function. Hits are created and filled by sensitive detectors. The user must construct their own sensitive detector class, inheriting from `G4VSensitiveDetector`. An instance of the class must be constructed in `G4DetectorConstruction::ConstructSDAndField()` and registered to a logical volume. If a step occurs in any placed instance of that logical volume, the sensitive detector uses information from `G4Step` to fill the hit object in the way given in the sensitive detector class. All hit objects from one event are stored in a `G4HitsCollection` which belongs to `G4Event`. To access hits, one can retrieve the hits collection from the event.

3.5 Geant4 application

In the following section, the simulation program built from the Geant4 toolkit is described. Classes and methods are mentioned, each for the construction of the detector geometry, primary particles and physics properties as well as data extraction. In Appendix B, selected parts of the source code are shown.

3.5.1 Geometry

3.5.1.1 Materials

Most materials were derived from the Geant4 Material Database [48] via the method `FindOrBuildMaterial()` of `G4NistManager`. This method takes a string as parameter, e.g. `"G4_AIR"` for air.
As paper does not exist in the Geant4 Material Database, the material `"G4_CELLULOSE_CELLOPHANE"` was used instead for the second layer of scintillator wrapping. The scintillator material had to be created from elements, according to the properties given in the data sheet by Saint Gobain [43]. For the creation of a composite material, the density and mass fractions of the components (for BC-408, that is carbon and hydrogen) must be known. The data sheet gives the number of atoms per cubic centimetre

$$N_{\mathrm{C}} = 4.74 \cdot 10^{22} \frac{\mathrm{atoms}}{\mathrm{cm}^3} \tag{3.5}$$

$$N_{\mathrm{H}} = 5.23 \cdot 10^{22} \frac{\mathrm{atoms}}{\mathrm{cm}^3}. \tag{3.6}$$

With the molar masses M_{C}, M_{H}, obtained through the `GetA()` method, the mass fractions result in

$$H_{\mathrm{fraction}} = \left(1 + \frac{N_{\mathrm{C}} M_{\mathrm{C}}}{N_{\mathrm{H}} M_{\mathrm{H}}}\right)^{-1} \tag{3.7}$$

$$C_{\mathrm{fraction}} = \left(1 + \frac{N_{\mathrm{H}} M_{\mathrm{H}}}{N_{\mathrm{C}} M_{\mathrm{C}}}\right)^{-1}. \tag{3.8}$$

The material is constructed in the function `DetectorConstruction::BC408()` by adding the components in the respective mass fractions. For the source code see Appendix B.1.

3.5.1.2 Volumes

The first volume to be constructed is the so-called world. It needs to house the whole setup and in this application it is filled with air. All other volumes are placed at a position and with a rotation with respect to the world center which is the position at which the world was placed.
The calorimeter mainly consists of only one type of volume, the scintillator piece, which is placed a number of times. The logical volume `scintLog` is constructed from the solid

scintBox and the material bc408. Placement is done in a loop, placing fNoOfScintLayers scintillators with a spacing of 5 mm along the z-axis starting from $z = 0$. At each of these positions, two more logical volumes are placed, representing the aluminium and paper wrapping around the scintillator material to avoid noise. They are created as G4SubstractionSolid to tightly enclose the scintillators. For the two triggering scintillators, another identical logical volume trigLog was created and placed 12 mm and 28 mm in front of the telescope's first scintillator. This separation into two different logical volumes is necessary as readout is attached to the logical volumes and the triggers do not contribute to the energy signal. The simulation model of all scintillator volumes is shown in Figure 3.7a.
For the simulation of a sampling calorimeter, additional absorber volumes were created and also placed with the help of a loop between the energy recording scintillators. The position-sensitive triple gas electron multiplier (GEM) foils are created as described in [49] with the help of an own class GEM for the possibility to consider them in the material budget. As position detection was not needed for this thesis, the holes in the foils were neglected.
To extend the measurable energy range, a member function AddBlock can be called to add an absorber block in front of the calorimeter. Input parameters are the desired material of the block, its dimensions and the z-coordinate of the end facing the beam. Together with this block, also a sphere around it is created. It is used to record properties of secondary particles as a function of the angle and is supposed to not influence the beam in any way, just save data. Therefore, it is made simply from air. An image of the simulation geometry with absorber block and sphere can be seen in Figure 3.7b.

3.5.1.3 Sensitivity

In order to record any data, sensitivity must be added to volumes. This is done in the function DetectorConstruction::ConstructSDandField(). Instances of the custom-made sensitive detector classes are created, registered to G4SDManager and associated with the according logical volume.
For energy detection in the calorimeter, an instance of the sensitive detector class EVolSD is linked to the scintillator logical volume scintLog. Every time a particle enters a placed instance of scintLog, EVolSD creates a new instance of EVolHit. The class EVolHit, derived from G4VHit, was constructed to store four quantities: the name of the physical volume, the name of the particle type, the particle's parent's ID and the total energy deposition of the step. This information is drawn from step and stored in the hit instance via Set and Get functions. At the end, the hit is added to the hits collection.
Two more sensitive detector classes were created, one for the absorber block and one for the sphere around it. Accordingly, they are called BlockSD and SphereSD. Both create instances of the class BlockHit to store information of particles that reach the end of the block or the sphere surface, respectively. Properties recorded are particle type, kinetic energy, exit position and momentum direction.

3.5.2 Physics list

The Geant4 physics list `"QGSP_BERT_HP"` [50] was used throughout the simulations. This physics list is based on the quark gluon string model for high-energy hadrons [51]. At lower energies, the Bertini cascade model [52] is applied, which shows more accuracy for the number of secondary particles produced. The abbreviation `HP` at the end of the physics list's name depicts the use of a high precision calculation for neutrons, considering neutrons even below 20 MeV. The physics list is created in `main()` through `G4PhysListFactory` and registered to the run manager.

3.5.3 Primary particle source

The Geant4 base class `G4GeneralParticleSource` was used to create the particle source in `PrimaryGeneratorAction`. Configuration was done in a macro file `gps_mono.mac`. Only monoenergetic protons with incident momentum direction $\vec{v} = (0, 0, 1)$ were used as primary particles. The initial position is a point at $x = y = 0$. z is chosen such that the particle starts before the beginning of the geometry. This was achieved by constructing the geometry in `main()` with the command `/run/initialize`. Then, the method `GetBeginOfSetup()` of `DetectorConstruction` was used to place the `GPS` in front of it.

3.5.4 Data output

Data is stored in ROOT [53] histograms, see Section 3.6. The `.root` file is registered to the `G4AnalysisManager` in `main()`. Histograms are created in `RunAction::BeginOfRunAction()` and filled in `EventAction::EndOfEventAction()`. Two types of histograms are created for each run, one for the energy deposition per scintillator layer, and one for the frequency distribution of the total energy per event.
In `EventAction::EndOfEventAction()`, the hits collection is retrieved from the instance of `G4Event`. In a for loop, all hits are checked for the name of the physical volume which gives the number of the scintillator slice in which the hit took place. The respective energy deposition in the i-th slice is added to the i-th entry of a C++ vector of length `fNoOfScintLayers`. The vector values therefore give the energy depositions for each layer. Per event, one vector is created. This is the basis for the first type of graph, named "E_scint". The values are plotted over the slice number, giving a bar plot in the domain one to `fNoOfScintLayers`. Vector values of different events are added on top of each other. In `RunAction::EndOfRunAction()`, "E_scint" is scaled by the number of events in the run, such that the entries give the mean energy deposition per scintillator slice.
For the second histogram, called "Etot", the vector values are summed up after each event to get the total energy deposition of the event in the whole PRR30 without regards for the spatial distribution. This gives a histogram of the total signal, showing the number of entries for each energy. x values in this histogram range from zero to the energy of the primary protons.

3.6 Data analysis with ROOT

As mentioned in Section 3.5.4, data extracted from the simulation was stored in `.root` files. This is a binary data file format. It contains a special structure, the ROOT Tree, which is very memory-efficient and optimised to handling large amounts of data. The `.root` file format was designed at CERN to the purpose of analysing results from collision experiments which produce a lot of data which has to be sorted carefully to extract significant information.
Evaluation of simulation data is done with the software toolkit ROOT [53, 54]. ROOT is a comprehensive data analysis framework which offers many useful features. One can save and sort data, fit functions to it as well as display it in various plots, like histograms or 3D representations. A description of most possibilities can be found in the user guide [55]. The framework is primarily written in C++, making use of the flexibility of object-oriented programming. It is being maintained and further developed by a group of scientists, mainly physicists and computer scientists. A big contribution also comes from the users which actively participate by recording problems along with possible solutions.
In this work, ROOT was used to store data from the simulation and do small analyses. The Gaussian fit to the total energy deposit was done in ROOT. Fit values were extracted and stored. ROOT offers three types of access. The interactive Object Browser is useful for quick display of recent results. All features are available by drop-down menus and their effect can instantly be seen on the screen. Short sequences of commands can be provided by macro file. For larger tasks on a number of files, an application can be built. This is the way most data extraction for this work was done.

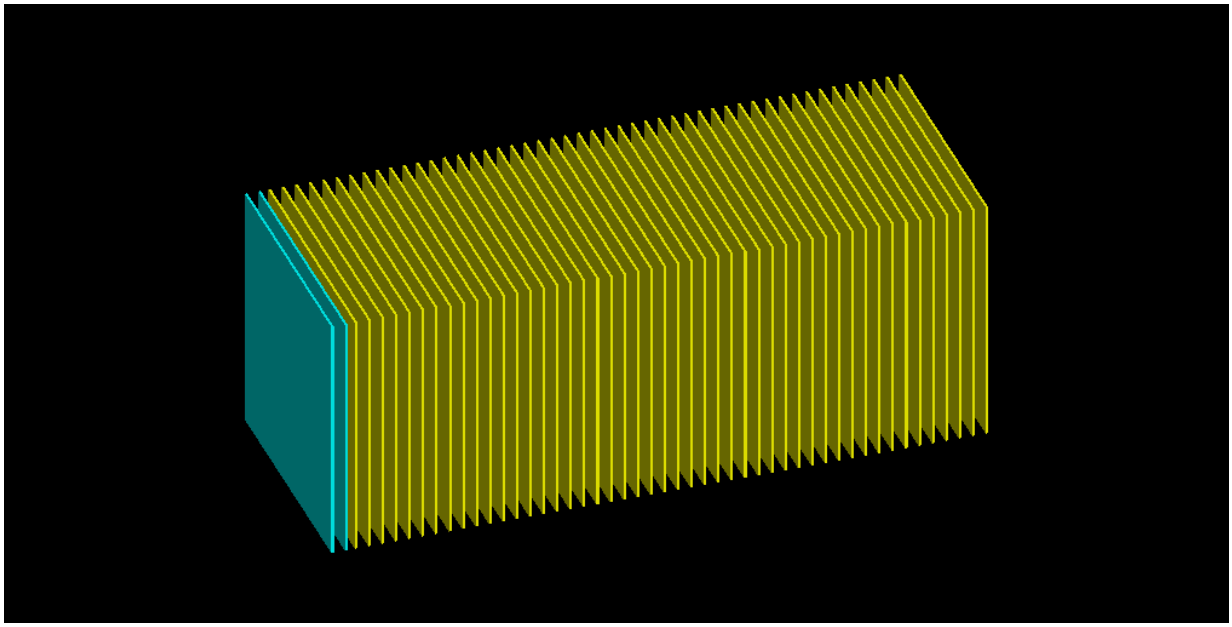

(a) Simulation geometry of the calorimeter. Energy recording scintillators are in yellow, the two trigger scintillators in cyan.

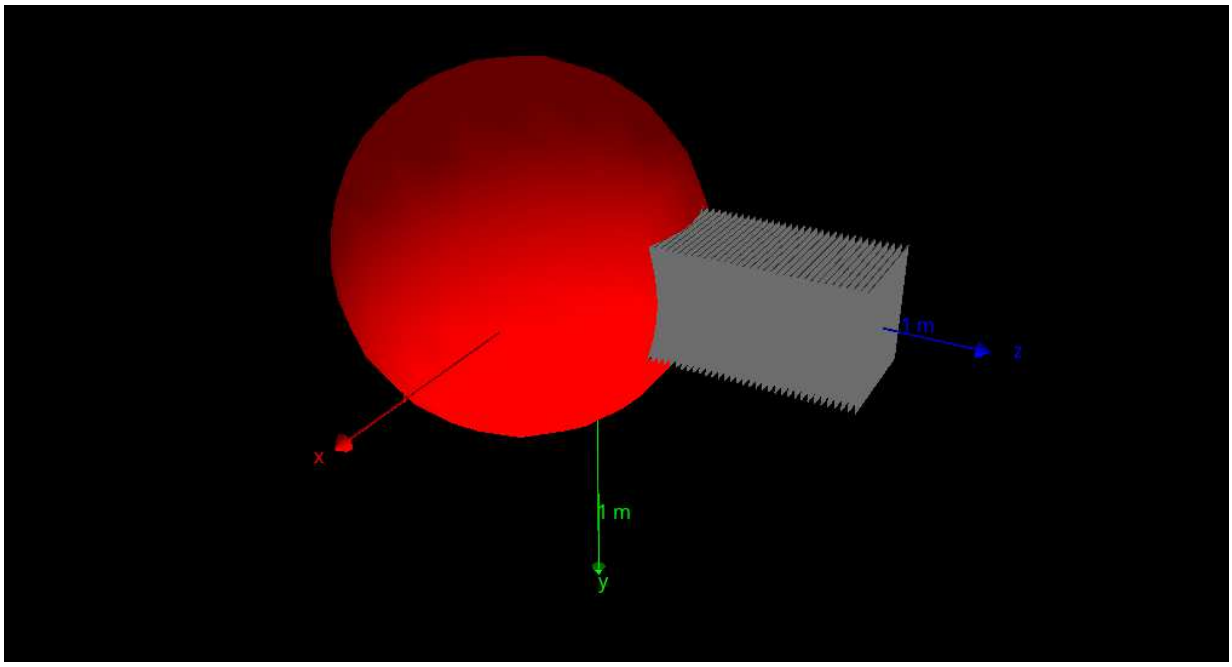

(b) Simulation geometry of calorimeter with absorber block in front of it together with a sphere around the block for particle recording.

Figure 3.7: Geometries used in the simulation.

4 Results and discussion

Results will be presented in three parts. First, the PRR30 was analysed. Energy range and resolution were derived.
In a second step, small modifications of the geometry were done. The primary goal was to widen the measurable energy range. At MedAustron, proton energies up to 800 MeV will be available. The advantage of high energies in respect of pCT is a straighter path of the protons through the target as the effect of multiple Coulomb scattering is lower at high energy see Section 2.2.6. To achieve this, two methods were employed. Firstly, a passive preabsorber was placed in front of the calorimeter to get the proton energy down before reaching the detector. On the other hand, absorber plates were placed between the scintillators to create a sampling calorimeter.

4.1 Pure TERA calorimeter

4.1.1 Bragg peak range

A calorimeter needs to fully absorb the particle in order to measure its energy. For heavy charged particles in the Bethe-Bloch region, the Bragg peak needs to be inside the calorimeter volume. As the Bragg peak position shifts in depth with increasing particle energy, there is an energy region for which this criterion is met. This energy interval is the operation regime of the calorimeter. This was the first property to be investigated in the simulation. In Figure 4.1 the Bragg peak in the calorimeter can be seen clearly. The x-axis shows the scintillator slabs, numbered from one to 40. The y-axis gives the energy (in MeV) deposited in each of these scintillator slabs. The PRR30 was designed to measure protons in an energy range between 20 MeV and 190 MeV [56]. However, some hardware components showed errors, reducing the number of usable scintillators. That is why the majority of the simulations was done for 40 instead of 48 scintillators. The energy region had to be re-identified for this adjustment. Bragg peak curves at different energies are shown in Figure 4.2. For 150 MeV, the peak is already outside the volume, and with it most of the energy deposition. The reduction from 48 to 40 scintillators cuts down on the upper end of the energy regime. Instead of 190 MeV as an upper end, as suggested in [56], the simulation shows that protons with $E > 135$ MeV can not be measured. Thus, the maximum energy can be set to be 135 MeV.
For the lower boundary, the evaluation is more complicated. As the peak is situated at the

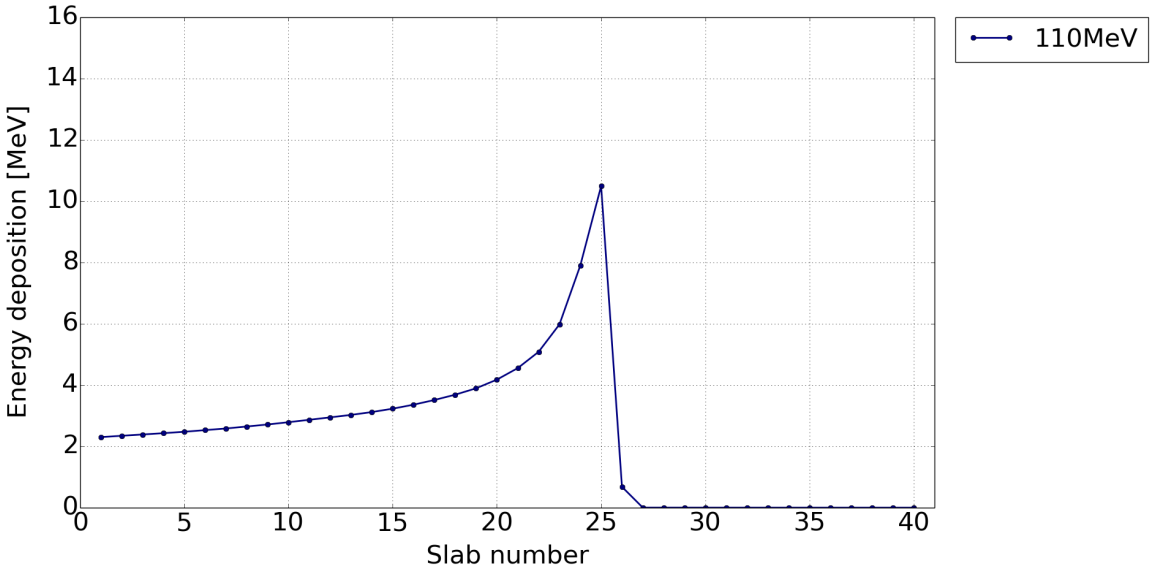

Figure 4.1: Bragg peak: Signal in calorimeter per scintillator slab. The values shown are the mean values of 10^6 primary protons with an initial energy of 110 MeV.

very end of the particle path, any small signal at the beginning of the calorimeter can be interpreted as the peak. To judge if it really is a peak and not just any signal, a significantly lower value before the maximum needs to be apparent. In Figure 4.2, this criterion is met for 40 MeV. This gives an energy range for the PRR30 of 40 MeV to 135 MeV.

4.1.2 Energy resolution

The Bragg peak position is important in order to determine the energy regime in which the detector can be used in principle. For the measurement of a concrete proton energy, the total energy deposition in the detector volume has to be evaluated. The deposited energy is proportional to the initial energy of the proton. Ideally, there is a linear relation of deposited energy to initial particle energy that is valid for the whole energy regime.
The total energy depositions per event were stored in a ROOT histogram called "Etot" during the simulation. Figure 4.3 shows an example of such a histogram. The x-axis gives the total energy deposit per event. The respective y-value gives the number of events with that energy deposit. Data from a run of 10^6 protons with initial energy of 110 MeV can be seen. A Gauss function was fitted to the histogram in a fit range of 40 MeV around the maximum's x-value. The fit captures the main peak well. A smaller subpeak is visible at $\approx$ 90 MeV. This is the result of the finite thickness of the scintillator plates and the passive air gap between them, limiting the possibility to distinguish particles' energy to any desired grade. If the Bragg peak position is between two scintillators, a significant part of the energy deposit is not detected. The particle seems to the detector as lower energetic as it truly is. In a simulation with more but thinner scintillators, the subpeak vanishes.

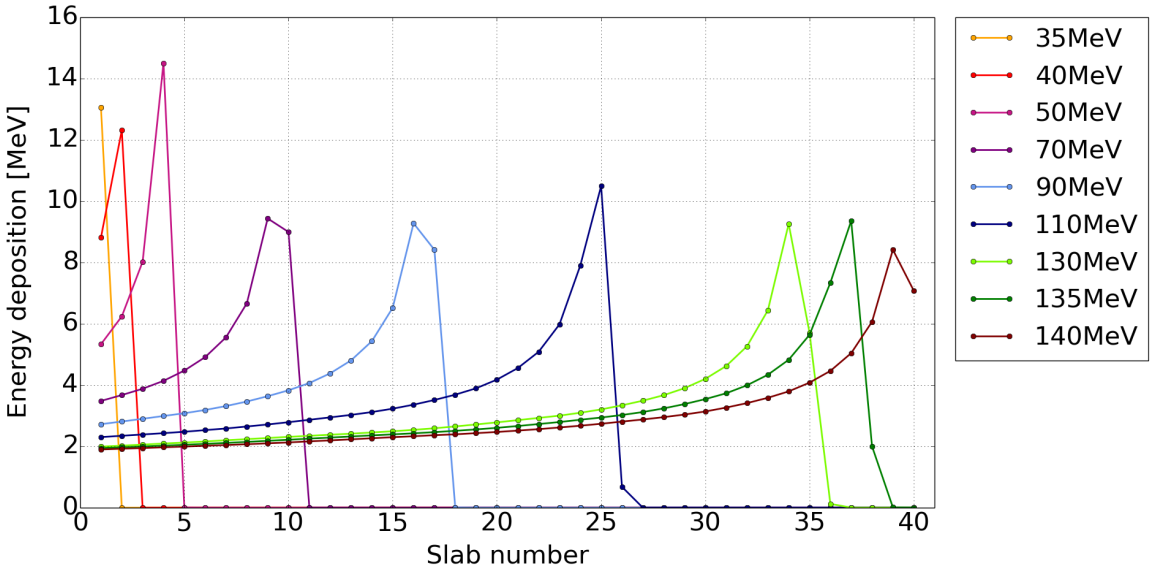

Figure 4.2: Energy range: Signal in calorimeter per scintillator slab for energy range from 40 MeV to 150 MeV. The values shown are the mean values from 10^6 primary protons.

Such an "Etot" histogram exists for all energies in the detectable range. Mean and standard deviation were extracted from the fit and plotted to judge the calorimeter response, see Figure 4.4. The mean μ is plotted as a function of the initial proton energy, with the standard deviation σ shown as error bars. The signal in the calorimeter is always lower than the initial energy (identity function). This makes sense as the proton will lose some of its energy already during its way through the air before entering the detector and between the scintillator sheets. Also, some secondary particles (e.g. photons) may escape the volume without interaction with the material. These parts of the energy are lost to detection. A linear function $f(x) = k \cdot x + d$ is fitted to the data in Figure 4.4. The fit parameters come to $k \approx 1.02$, $d \approx -16.31$. The data points follow this linear function very well.

As a measure for the energy resolution, the standard deviation σ was divided by the initial proton energy E [57]. This resolution $\frac{\sigma(E)}{E}$ can be seen in Figure 4.5 as a function of the initial particle energy. Values are shown in percent. The energy resolution is below 2% for the whole energy range of 40 MeV to 135 MeV. At two energies, 55 MeV and 75 MeV, $\frac{\sigma(E)}{E}$ is significantly higher than for the rest of the range. To understand this, a closer look at the distribution of the energy deposition is necessary. In Figure 4.6, the signal per scintillator slice for 55 MeV and 65 MeV is shown. In both cases, the signal does not drop down to zero right after the Bragg peak's maximum but shows an entry in the next scintillator slice. For 55 MeV, this value is significantly larger, which means that more protons reached this slice. The total energy deposit of all protons reaching the i-th slice shows a Gaussian shape around the mean value. In the "Etot" histograms in Figure 4.7, the superposition of the individual Gaussians for the slices are visible. The main peak at the highest energy

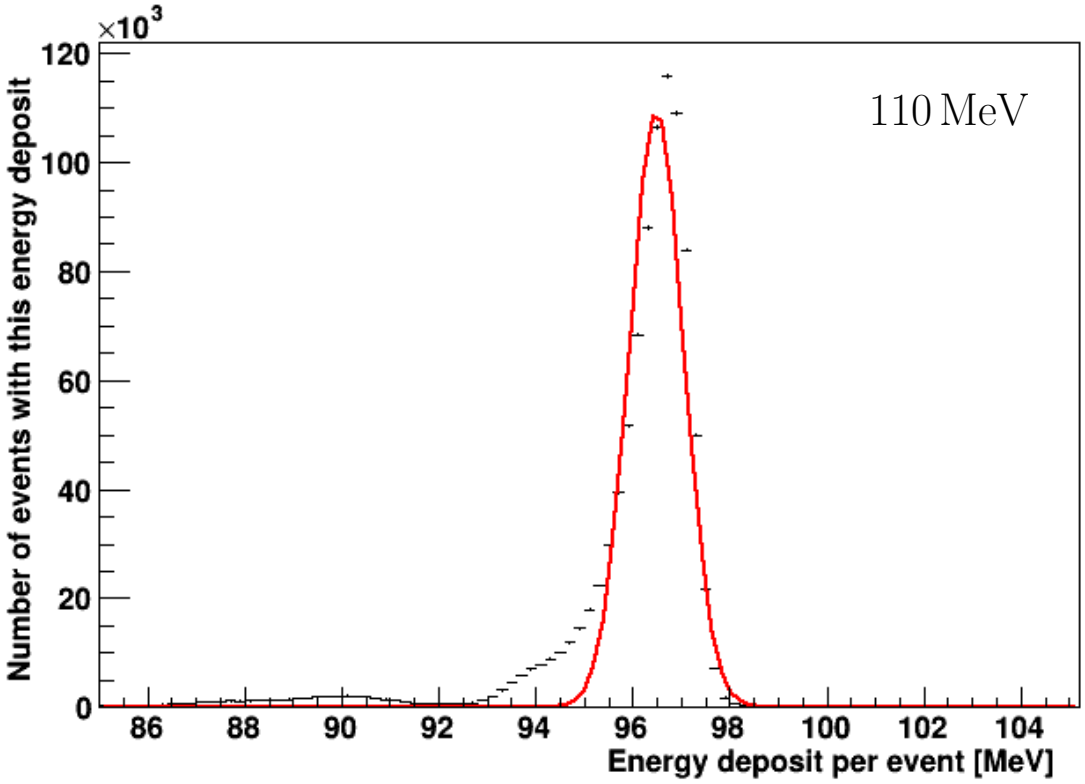

Figure 4.3: ROOT histogram shows number of events per total energy deposition for a run of 10^6 protons with initial energy of 110 MeV. The red curve is the Gauss function fitted to the data. Mean value μ and standard deviation σ from this fit are: μ =96.5 MeV, σ =0.561 MeV.

comes from the particles reaching the last slice with signal above zero. This peak is much more narrow for 65 Mev and is "caught" by the fit nicely. For 55 MeV, the peak is broader and closer the peak for the slice before. The fit function can not distinguish between the two peaks anymore and fits them as one, resulting in a much larger standard deviation as can be seen in Figure 4.4. The same is the case for 75 MeV. The underlying reason is the separation of the detector volume into slabs. With a homogeneous scintillator, this problem does not arise.

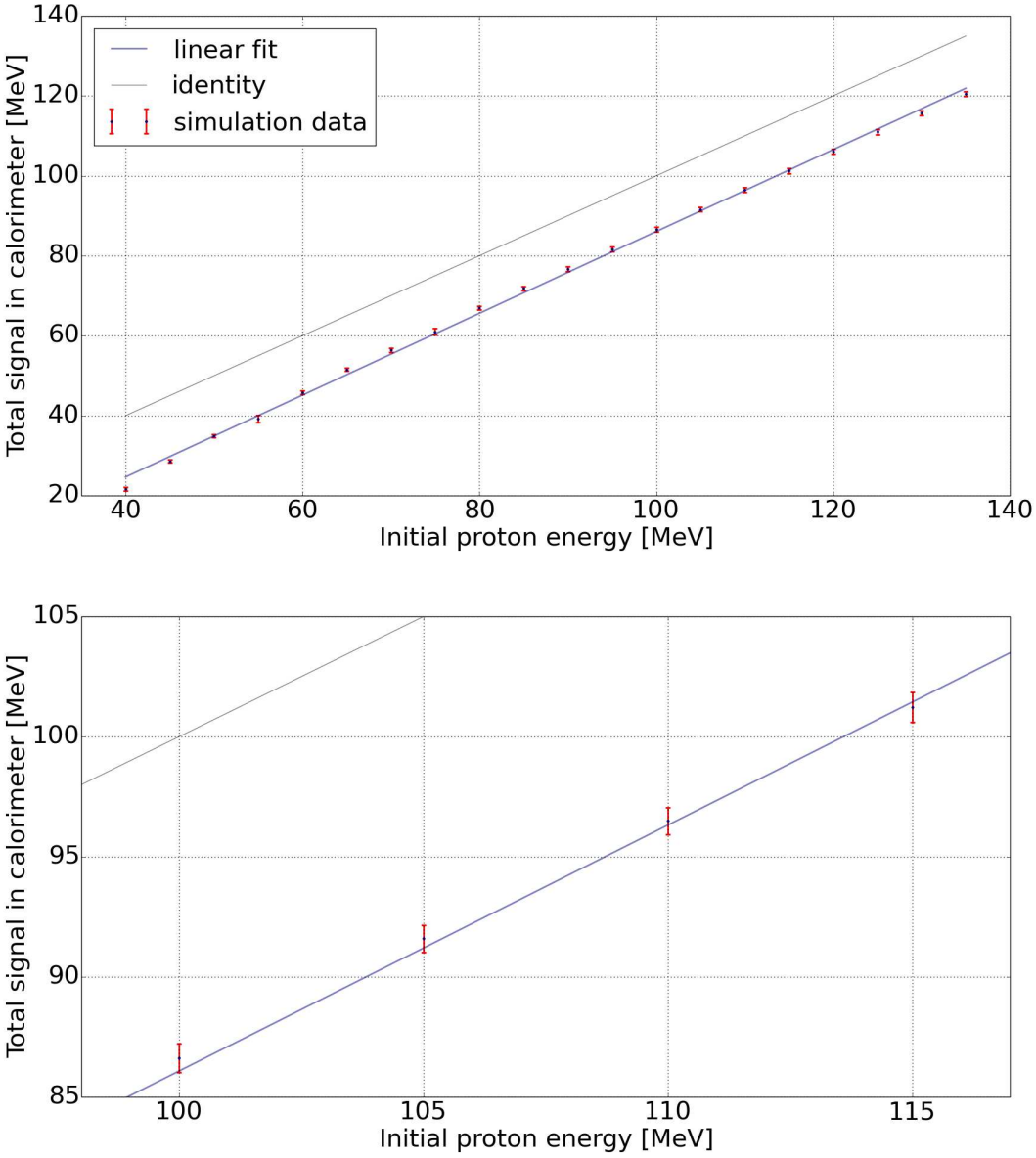

Figure 4.4: Plot of $\mu(E)$ with $\sigma(E)$ as error bars for the TERA calorimeter. Linear fit function $f(x) = k \cdot x + d$ with fit parameters $k \approx 1.02$, $d \approx -16.31$. The lower figure is a zoom into a small region of the upper figure.

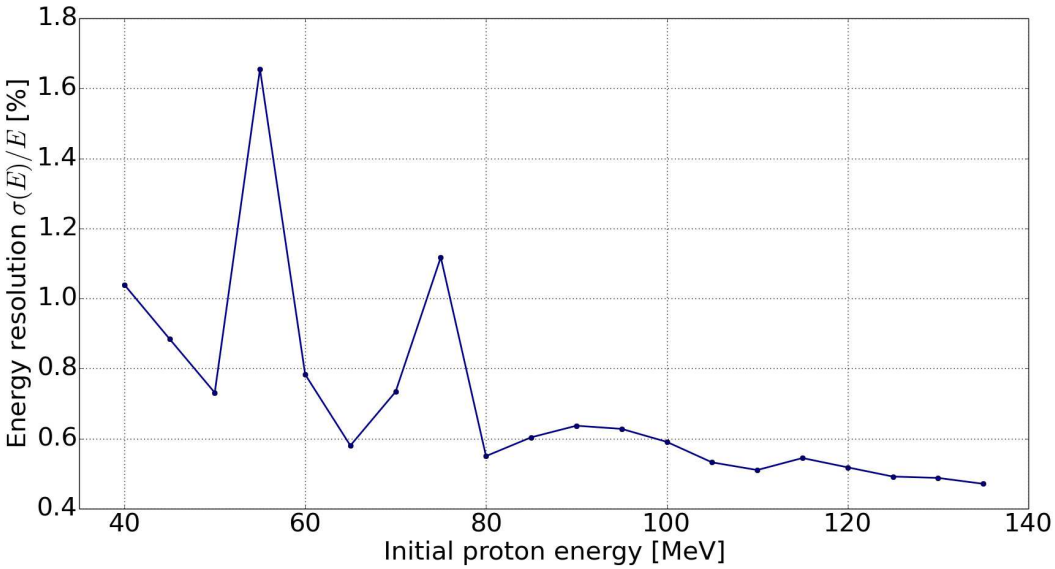

Figure 4.5: $\frac{\sigma(E)}{E}$ of the TERA calorimeter.

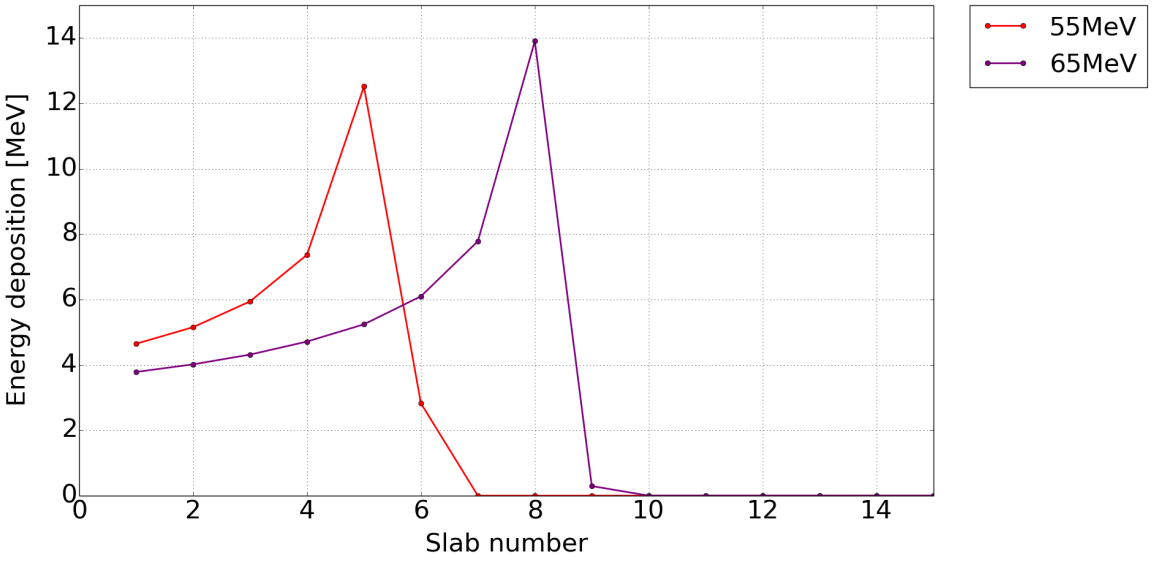

Figure 4.6: Signal per scintillator slice for 55 MeV and 55 MeV. The last entry before the drop down to zero is higher for 55 MeV.

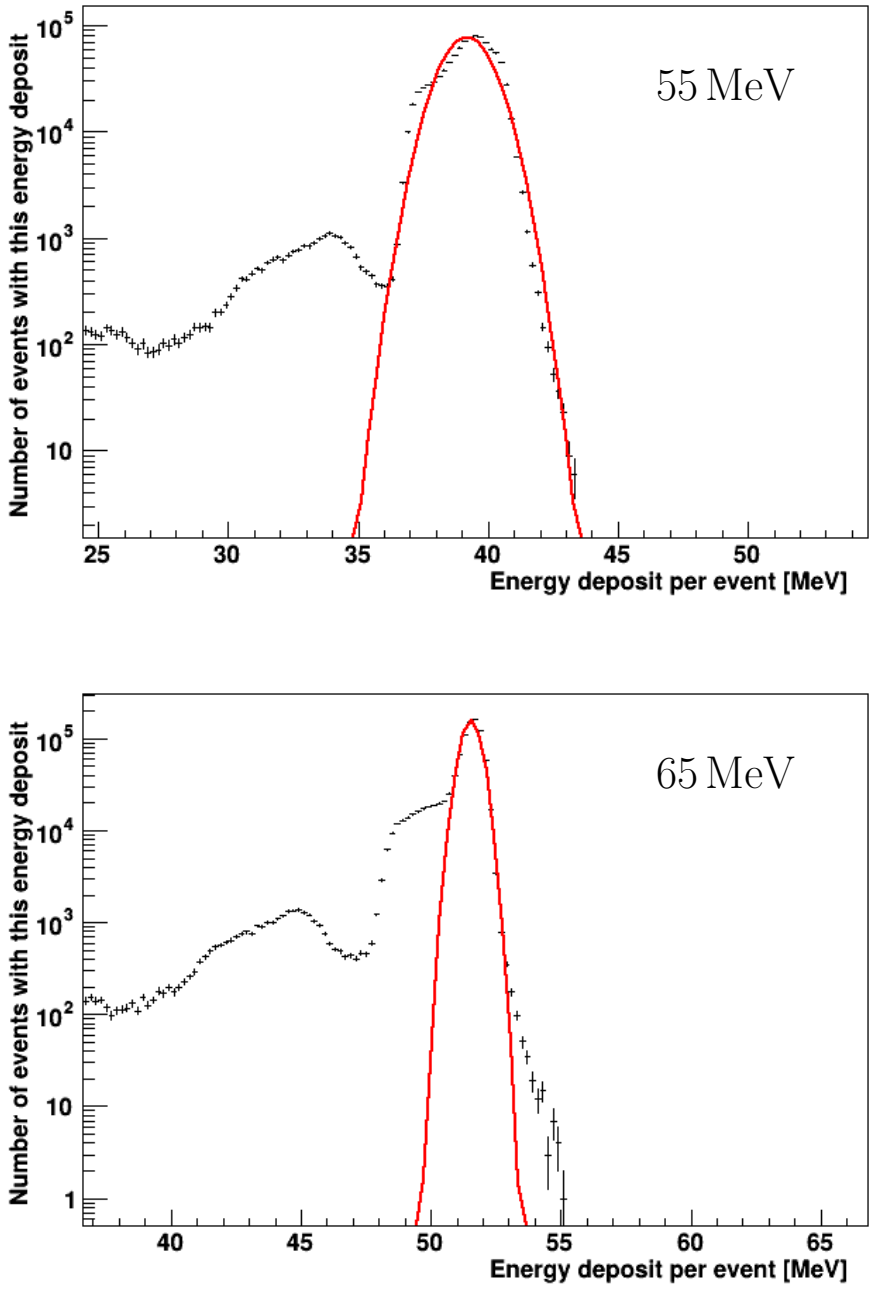

Figure 4.7: Comparison of fit to total energy per event for 55 MeV and 65 MeV. The two superimposed Gaussian peaks in each figure show the energy distribution of protons reaching the last or second to last scintillator slice with signal above zero, respectively. For 55 MeV, they are no longer distinguishable in the fit process. The resulting fitted function has a larger standard deviation σ. This is visible as a peak inFigure 4.4.

4.2 Extension of energy range with passive preabsorber

In order to detect 800 MeV protons, the energy range of the PRR30 must be extended beyond 135 MeV. Any material in front of the calorimeter will slow down the particles before they enter the detector. Blocks of different materials and thicknesses were placed there and the response in the PRR30 was recorded. If space is an issue, a high-density material should be chosen. Materials investigated in the simulation are iron (Fe), lead (Pb), tungsten (W), water and Polymethyl methacrylate (PMMA). In order to measure 800 MeV protons in the PRR30, blocks of up to 40 cm in thickness are needed in case of metal absorbers (Fe, Pb, W). For PMMA and water, the blocks need to be as large as 2 m.

4.2.1 Bragg peak range

The goal was to obtain a setup with a large energy interval in which the Bragg peak is as distinct as possible. Figure 4.8 and Figure 4.9 show the signal development for Fe as preabsorber material. Four thicknesses are chosen, 5 cm, 15 cm, 25 cm and 35 cm. For each, the signal per scintillator in the calorimeter is shown at different primary proton energies. In the first case, a 5 cm Fe preabsorber, the Bragg peak and its shift along the detector volume with increasing energy can be clearly seen. As the thickness increases, the peak gets more and more shallow. The initial proton beam is monoenergetic. Every proton has the same primary energy as depicted by the color. After passing the absorber block, the beam is not monoenergetic any more. Statistical variations in the interaction with the absorber material leads to an energy distribution. The signal of each single proton in the calorimeter would still show a Bragg peak. The sum of all protons, however, is a superposition of Bragg peaks at different positions.
The results are very similar for Fe and Pb. For practical experimental use however, Pb is unattractive due to its toxicity. Tungsten (W) shows a much higher stopping power than the other two metals. This can be seen in Figure 4.10 and Figure 4.11. This is in part due to its significantly higher density of 19.25 $\mathrm{g\,cm^{-3}}$ (compared to 11.342 $\mathrm{g\,cm^{-3}}$ for Pb). As a consequence, W absorbers are thinner, which is convenient as an experimental setup can be made more compact.
Figure 4.12 shows the energy range in which a Bragg peak can be found inside the calorimeter for different thicknesses of the preabsorber block for materials Fe, Pb, W and PMMA. Thicknesses investigated range from 5 cm to 40 cm for Pb and Fe, from 5 cm to 20 cm for W, in 5 cm steps. For PMMA, 50 cm steps are shown from 50 cm to 200 cm. The energy range for one setup gets narrower with increasing thickness.

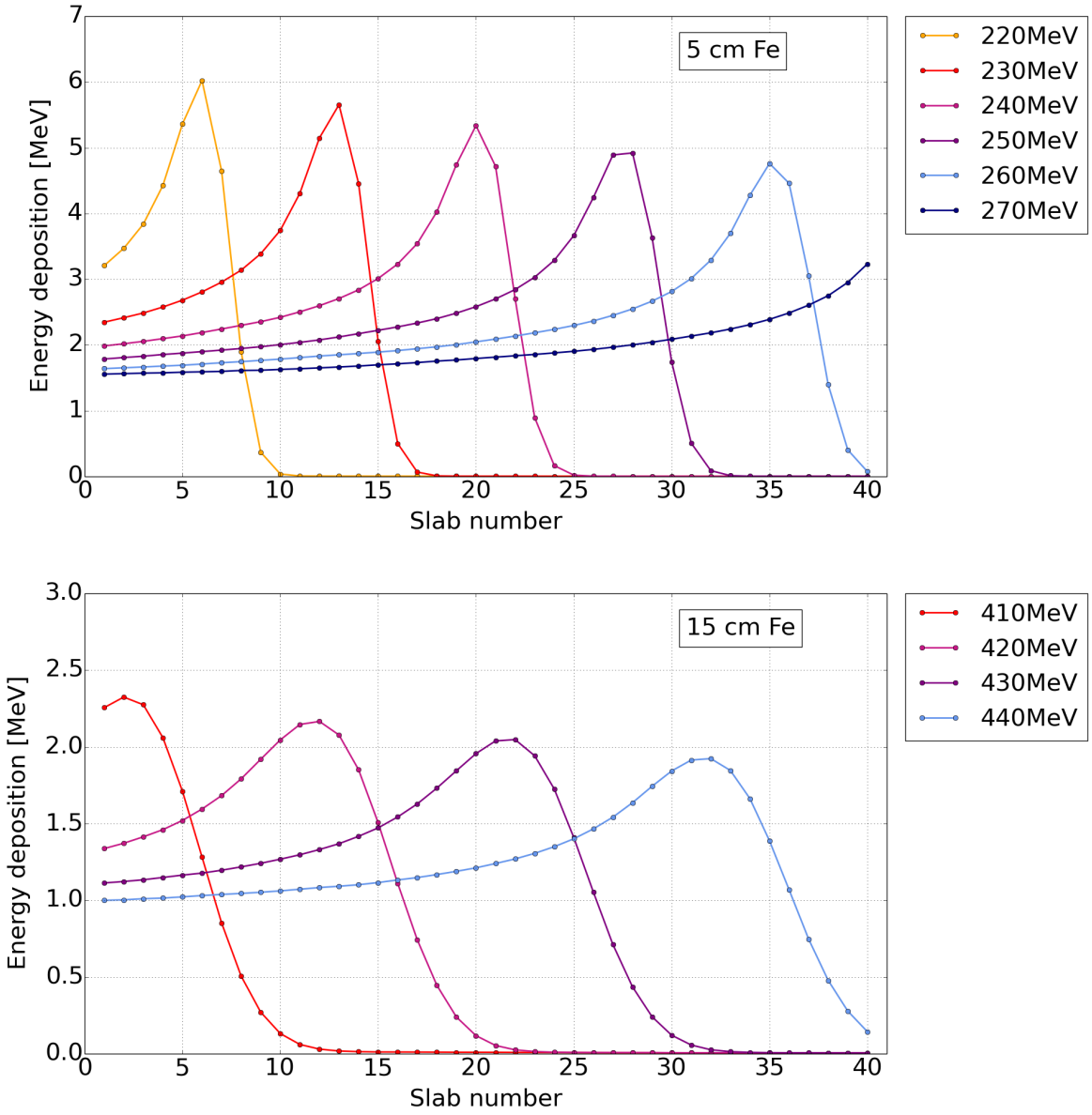

Figure 4.8: Signal in TERA calorimeter per scintillator slab with a Fe absorber placed in front of it. The graphs are colored according to the initial energy of the primary protons.

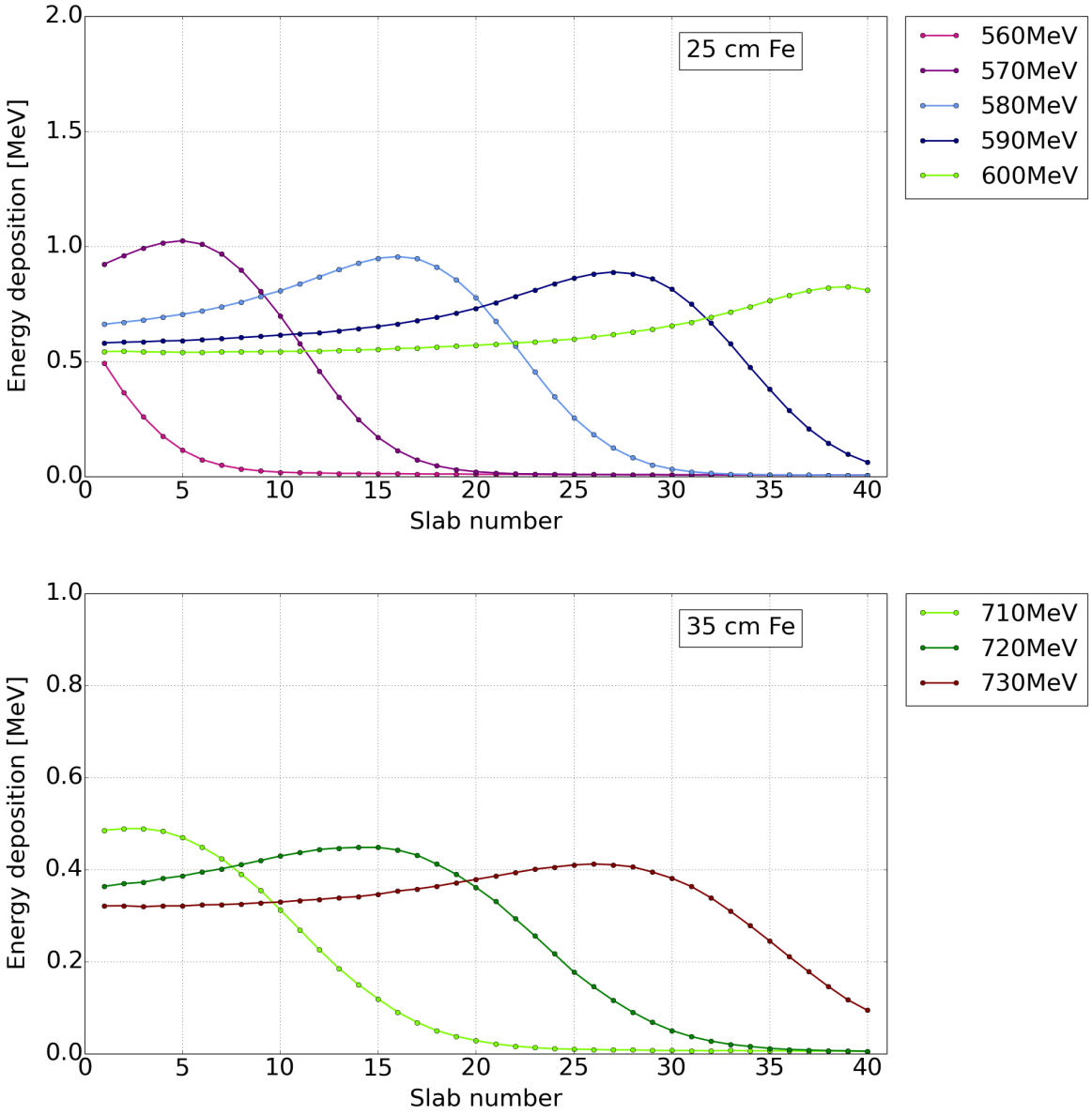

Figure 4.9: Signal in TERA calorimeter per scintillator slab with a Fe absorber placed in front of it. The graphs are colored according to the initial energy of the primary protons.

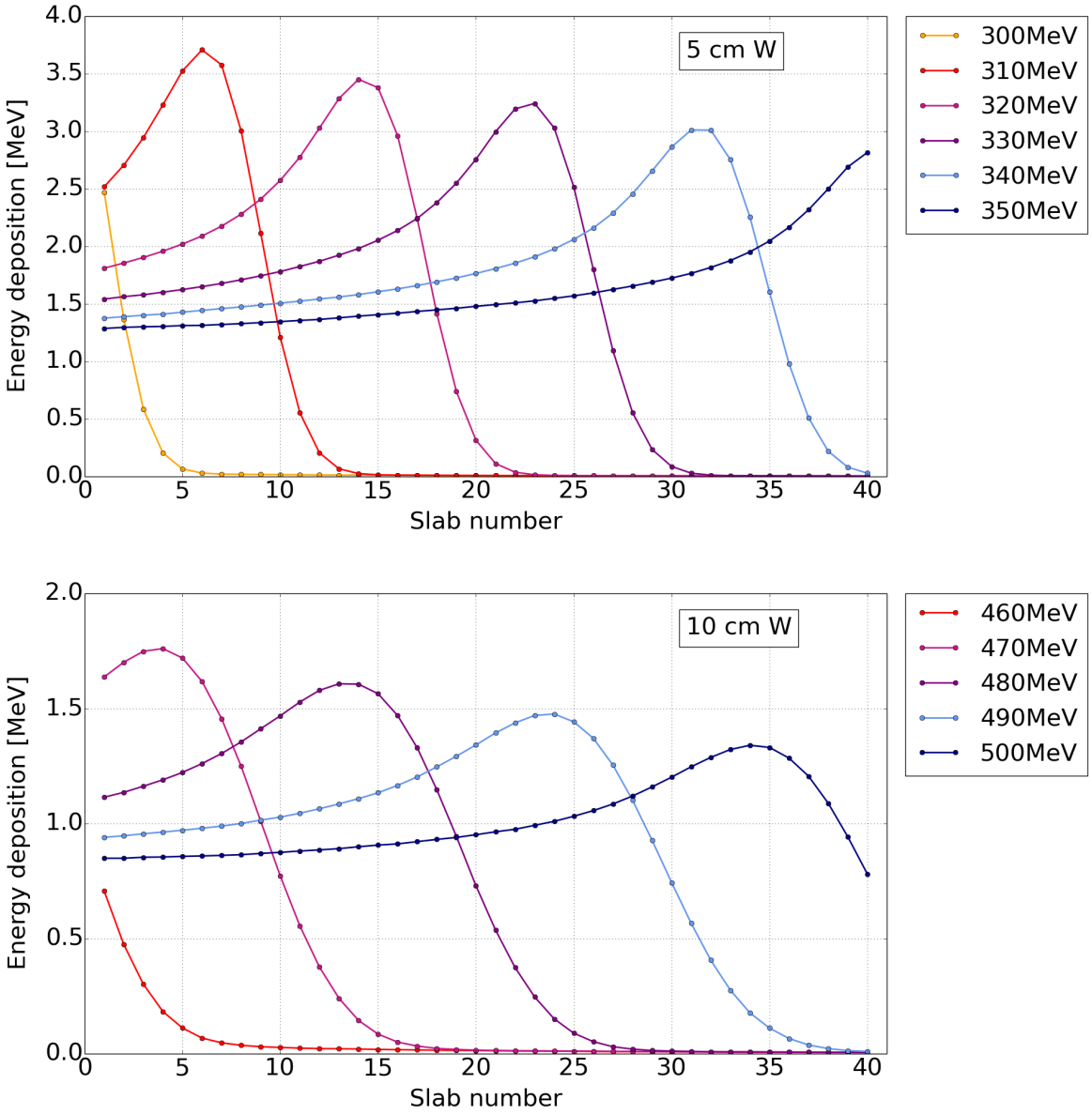

Figure 4.10: Signal in TERA calorimeter per scintillator slab with a W absorbers placed in front of it. The graphs are colored according to the initial proton energy.

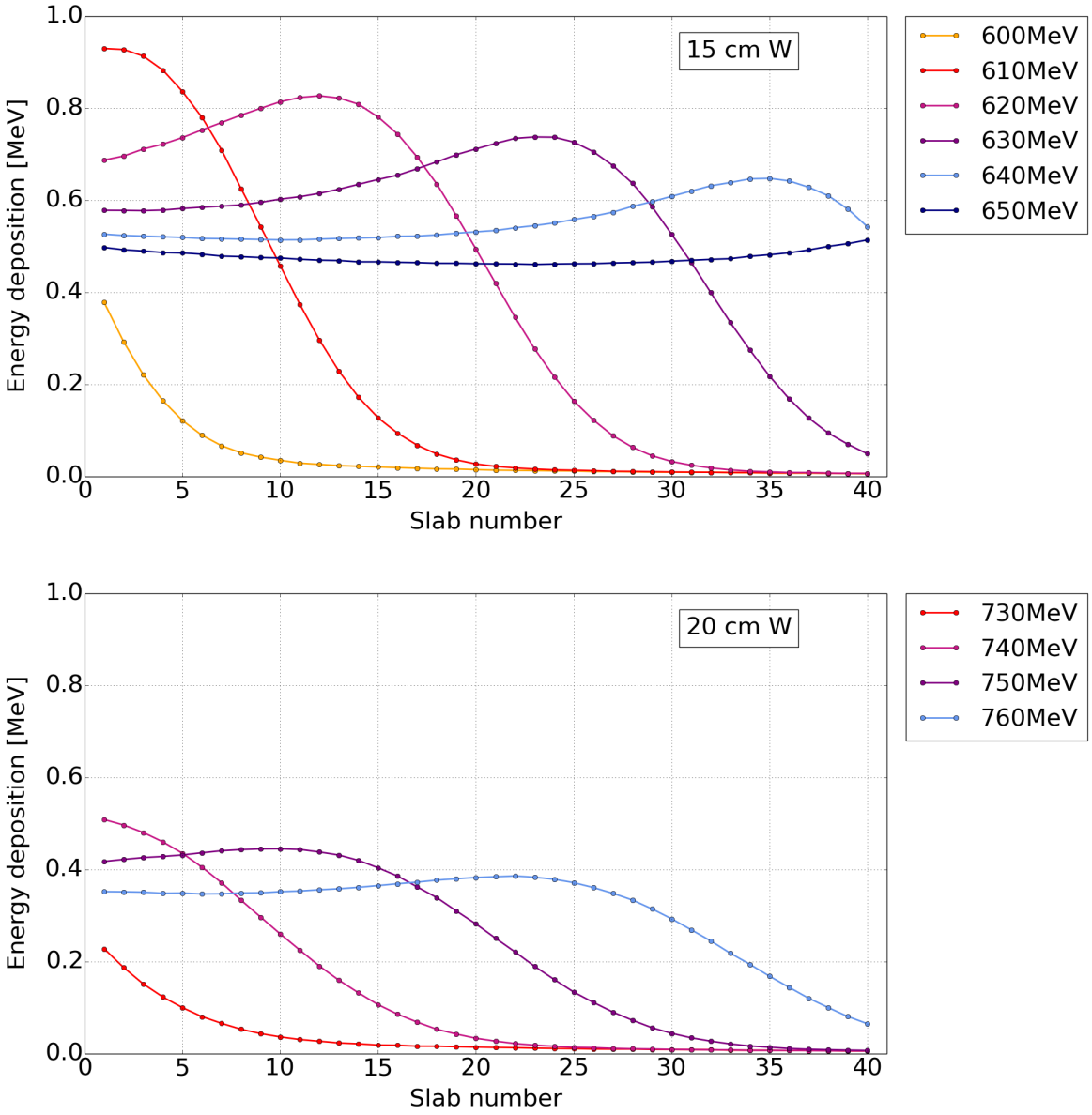

Figure 4.11: Signal in TERA calorimeter per scintillator slab with a W absorbers placed in front of it. The graphs are colored according to the initial proton energy.

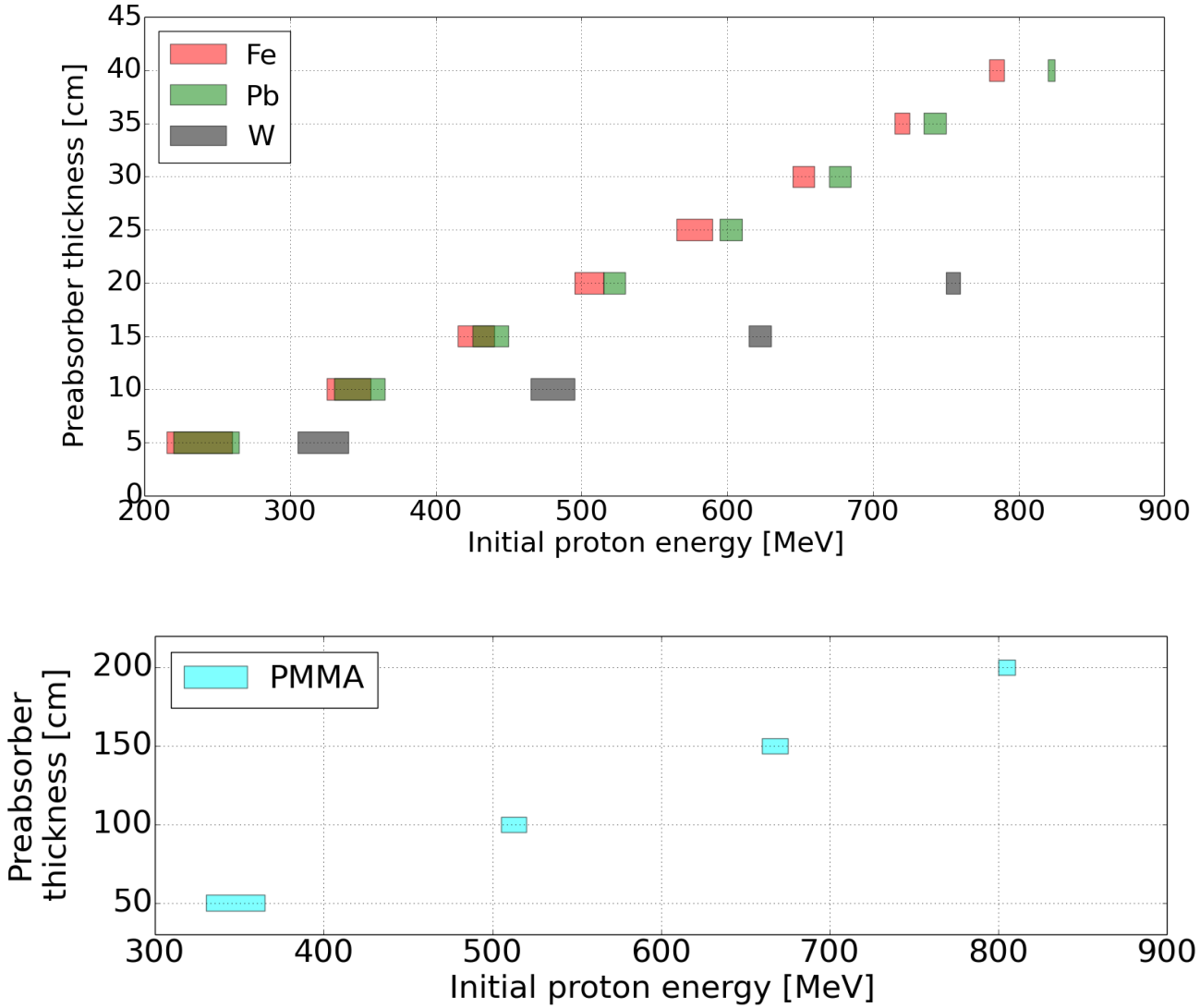

Figure 4.12: In PRR30 measurable initial proton energies with use of preabsorber block of various materials and thicknesses.

4.2.2 Energy resolution

To obtain data on the energy resolution of the configuration with preabsorber blocks, the same procedure was executed as described in Section 4.1.2 for the energy resolution of the pure PRR30. A Gauss function was fitted to the histograms "Etot" which show the total energy deposit per event. Mean μ and standard deviation σ of this fit were stored and plotted as a function of the initial proton energy.
With preabsorber blocks, the total energy deposit in "Etot" does not show a nice narrow peak like in Figure 4.3 for the PRR30 by itself. Instead, a big part of all events shows a total energy deposit very close to zero. If a Gaussian fit is done on this histogram, the major peak will sometimes not be caught correctly, see Figure 4.13a. In this case, the fit range was cut to start from a value larger than zero. This can be seen in Figure 4.13b for a cut at 5 MeV, where the fit was done to an energy range from 5 MeV to 200 MeV.
The large low-energy fraction is caused by secondary particles, mainly protons and electrons. In Figure 4.14 and Figure 4.15, the total energy deposit is shown discriminated by particle type for electrons and protons. If only primary protons are considered, the low-energy part completely disappears, see Figure 4.14b.
The energy resolution properties from the fits are shown in Figure 4.16 and Figure 4.17. Again, Figure 4.16 shows the mean values μ as a function of the initial proton energy, with the standard deviation σ as error bars. In Figure 4.17, the relative energy resolution $\frac{\sigma(E)}{E}$ is plotted over the initial proton energy. Each line in Figure 4.16 and Figure 4.17 shows the properties of the calorimeter with one absorber block of a certain material and thickness in front. The materials can be distinguished by the color of the line. The shape of the data points depicts the thickness.
For thick absorbers, the width of the total energy deposit distribution is larger than for thin absorbers. This results in much longer error bars in the curve for e.g. 20 cm W than for 5 cm W. The relative energy resolution $\frac{\sigma(E)}{E}$, however, is almost the same. This comes from the fact that the larger standard deviation is divided by an also larger initial proton energy in case of the 20 cm block.
For each absorber block of one material and one thickness, its individual curve $\frac{\sigma(E)}{E}$ over E is monotonically decreasing. This is due to the well-known fact that the energy resolution of a calorimeter increases with increasing energy [13]. For all shown absorber blocks, the energy resolution is between 1 % and 3 %, so approximately one percent higher than for the calorimeter without preabsorber.

4.3 Extension of energy range with sampling calorimeter

Another approach to extend the energy range of the calorimeter is to change it into a sandwich sampling calorimeter. After each layer of scintillator, one or more layers of passive absorber material is placed. One can add the same total amount of passive material as in the preabsorber such that the particles are slowed down to energies detectable by the

PRR30. Due to the scintillator sheets in between, one can get information from points over the whole particle path instead of only at the end.
Absorber materials investigated are brass, bronze and copper (Cu) as those are materials commonly used in sampling calorimeters. The variation of these three absorber materials showed no significant difference in the signal. Absorber pieces of 3 mm, 4 mm and 5 mm were investigated, each in 1:1 and 2:1 alternation with the scintillators. For 2:1, two absorber pieces were placed between each neighbouring pair of scintillators. Also configurations with linearly increasing as well as decreasing absorber thicknesses were simulated. The thickness of the scintillator pieces was constant at 3 mm. The distance between any two elements (scintillator-absorber or absorber-absorber) was always 5 mm. Simulations were done with 10^5 primary protons per run. Table 4.1 gives an overview of the simulated configurations with linearly varying absorber thickness. Plots are only shown of some configurations as representatives.

thickness range [mm]	bronze	brass
1 - 15	✓	
1 - 10	✓	
0.5 - 20	✓	
0.2 - 20	✓	
0.1 - 22	✓	✓
0.01 - 22	✓	ⓥ

(a) Linearly increasing

thickness range [mm]	bronze	brass	Cu
5 - 1	✓		
10 - 1	✓		
12 - 2		✓	
15 - 1	ⓥ	✓	
20 - 1		✓	
50 - 1			✓

(b) Linearly decreasing

Table 4.1: Simulated thickness variations. The circled checkmarks denote those analysed in detail in the following sections.

4.3.1 Bragg peak range

The energy deposit per scintillator sheet of the configuration with 3 mm brass absorber alternating 1:1 can be seen in Figure 4.18. The Bragg peak is very well distinguishable in the shown energy range from 60 MeV to 380 MeV which gives an interval of 320 MeV. This is a slight increase of the range from the pure TERA calorimeter (195 MeV; from 40 MeV to 135 MeV). The peak maxima are gradually decreasing.

One challenge with sampling calorimeters is visible in Figure 4.19, where the energy deposition per scintillator slab is shown for a configuration with linearly decreasing absorber thickness from 15 mm to 1 mm bronze. The Bragg peak maxima are not steadily decreasing in value but jump up and down. For example, the maximum of the 350 MeV curve is significantly lower than the one for 450 MeV. The reason is that the position of the maximum energy deposition came to lie inside an absorber instead of a scintillator. As a result, a great part of the energy is deposited "invisibly" outside the sensitive volume.

This falsely shrinks the Bragg peak of the 350 MeV run.

Another property in Figure 4.19 is the broad local maximum before scintillator number five for energies ≥ 350 MeV. The contribution grows with increasing energy. This can be seen very distinctly for 800 MeV as this curve lies clearly above the others for most part of the shown energy range. This fact and the shape of the curves hint to particle showers as the underlying cause. In Figure 4.20, the longitudinal energy deposition of a hadronic particle shower is shown. The shape of the curves in Figure 4.20 is very similar to the one in Figure 4.19. This shower-related bump can be seen in most of the simulated sampling structures. It is most prominent for the ones with decreasing absorber thickness (Figure 4.19). Here, very high-energetic particles meet thick, high-density and high-Z absorbers. According to Equation (2.13), the creation of neutral pions is more likely for these high energies. This results in a higher electromagnetic component which causes a higher signal than purely hadronic deposition (see Section 2.4).
The shower induced part can also be seen in Figure 4.21 for the 2:1 arrangement with 5 mm brass and in Figure 4.22 for linearly increasing thickness from 0.01 mm to 22 mm, but the contribution is much lower. For 1:1 with 3 mm, it vanishes (see Figure 4.18).

The Bragg peak range for three representative configurations is shown in Figure 4.23. The absorber material in all three cases was brass.

4.3.2 Energy resolution

Analogous to the method in Section 4.2.2 and Section 4.1.2, the energy resolution properties for the sampling calorimeter were extracted from the Gaussian fit to the total energy deposit in the whole calorimeter.
The total energy deposit shows a very narrow peak at low energies. As the energy increases, the tails to both sides of the peak broadens more and more. The tip of the peak remains recognisable in most cases, see Figure 4.24. For decreasing thickness and the 5 mm brass 2:1 configuration however, a broader sub-peak starts to emerge, see Figure 4.25. This is caused by the growing number of secondary particles at higher energies in the thick and dense absorber pieces. The signal solely from primary protons does not show this feature but only the narrow peak at ≈ 40 MeV, see Figure 4.26. Primary protons are the particles of which the energy must be measured, thus the fit was done to this peak. This was achieved by limiting the fit range to 5 MeV around the maximum's x-value.

Figure 4.27 shows the plot of the mean μ over the initial proton energy for three sampling configurations with brass as absorber material. The standard deviation σ is drawn as error bars. The very flat rise of the curve for increasing thickness is a problem. From the signal in the calorimeter it is no longer possible to deduce the initial proton energy. A signal of 30 MeV in the calorimeter can mean any initial proton energy between 550 MeV and 800 MeV. The signal for 200 MeV is even lower than the one for 250 MeV. For higher energies, the curve shows a rise, but it is not steep enough to allow for discrimination as the error bars are larger than the difference in signal. The 5 mm curve is steeper but still not steep enough in relation to the size of the error bars. Only for the 3 mm configuration, the signal can definitely be traced back to an initial energy. But this configuration can only

be used in a small energy range compared to the others, see Figure 4.23. All three curves show significant deviations from a linear function. The various kinks make it impossible to map the energy deposit back to an initial energy. The fraction of energy deposited in the passive absorbers shows unpredictable variations.

The significance of an energy resolution value is questionable as the energy signal can not be used due to its ambiguity. For the sake of completeness, a plot of $\frac{\sigma(E)}{E}$ is shown nevertheless in Figure 4.28. The kinks from Figure 4.27 are amplified. The rise towards higher energies which is typical for calorimeters can not be seen for the sampling arrangements (compare with Figure 4.17). The energy resolution jumps up and down between 0.2 and 1.2 %. This seems like a low value, i.e. a good energy resolution. It has to be considered though, that σ is taken from the Gaussian function fit only to the narrow peak of the total energy deposit, see Figure 4.24 and Figure 4.25. The influence of the broad base in Figure 4.24 and increasingly prominent subpeaks in Figure 4.25 are not included.

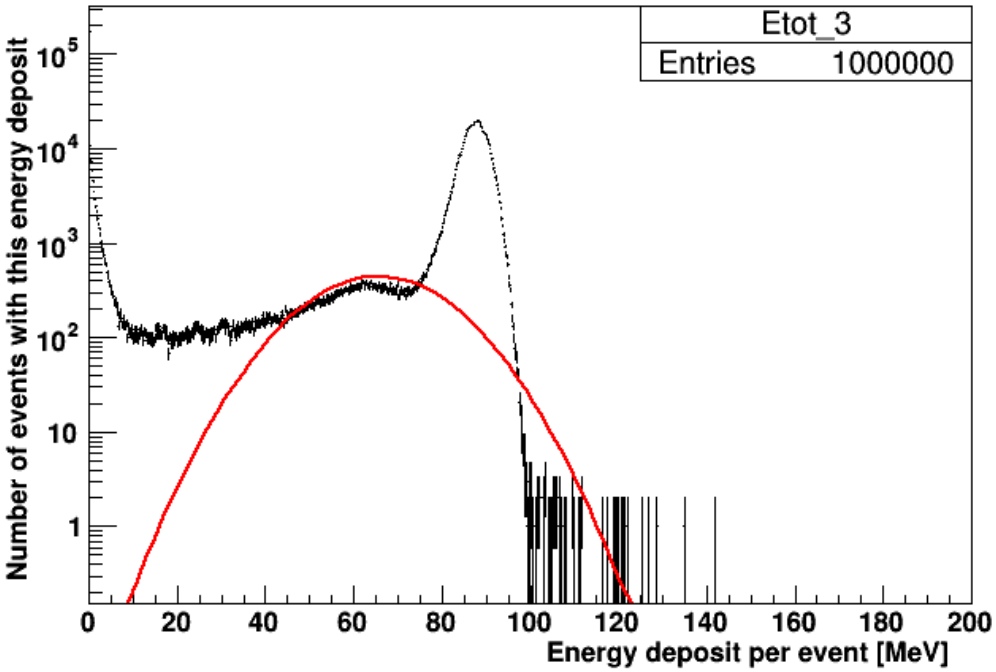

(a) Fit over whole x range

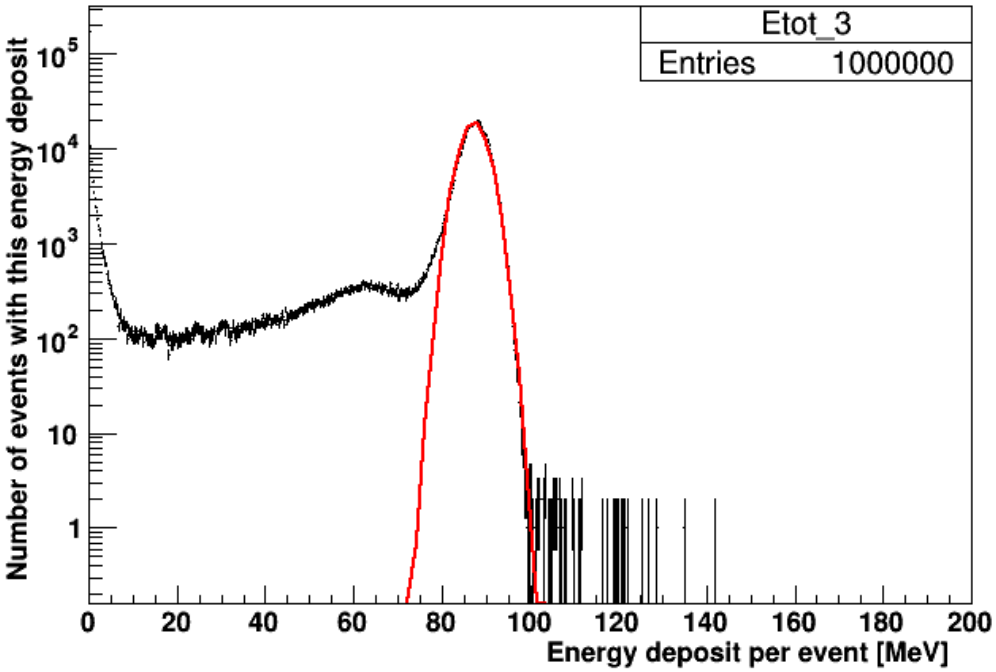

(b) Fit range from 5 MeV to 200 MeV

Figure 4.13: Gaussian fit to total energy deposit per event for PRR30 with 5 cm Fe preabsorber

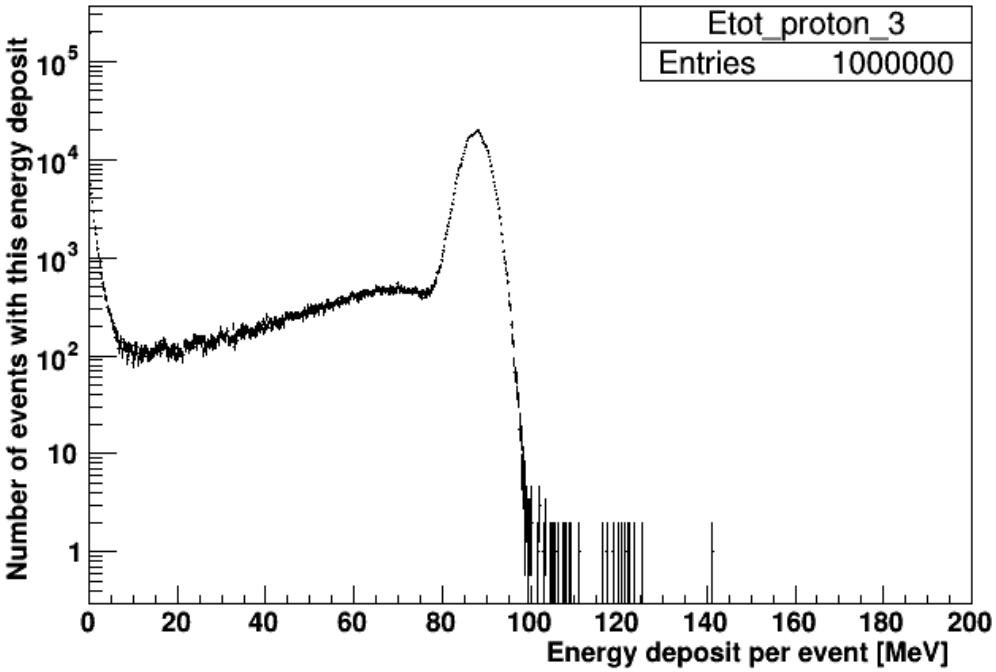

(a) All protons

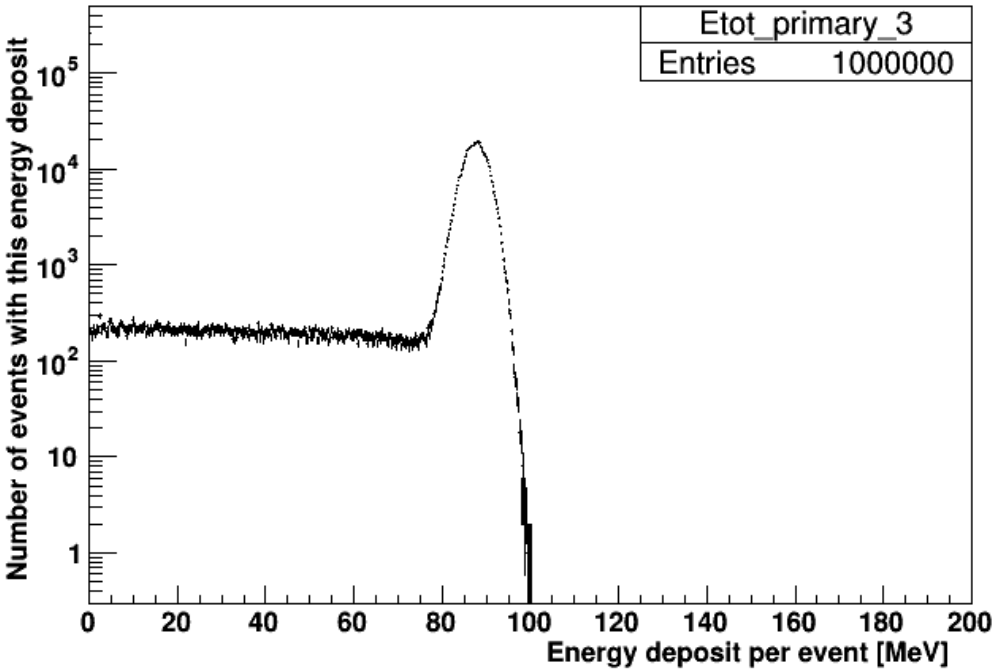

(b) Primary protons

Figure 4.14: Total energy deposit per event, protons' contribution.

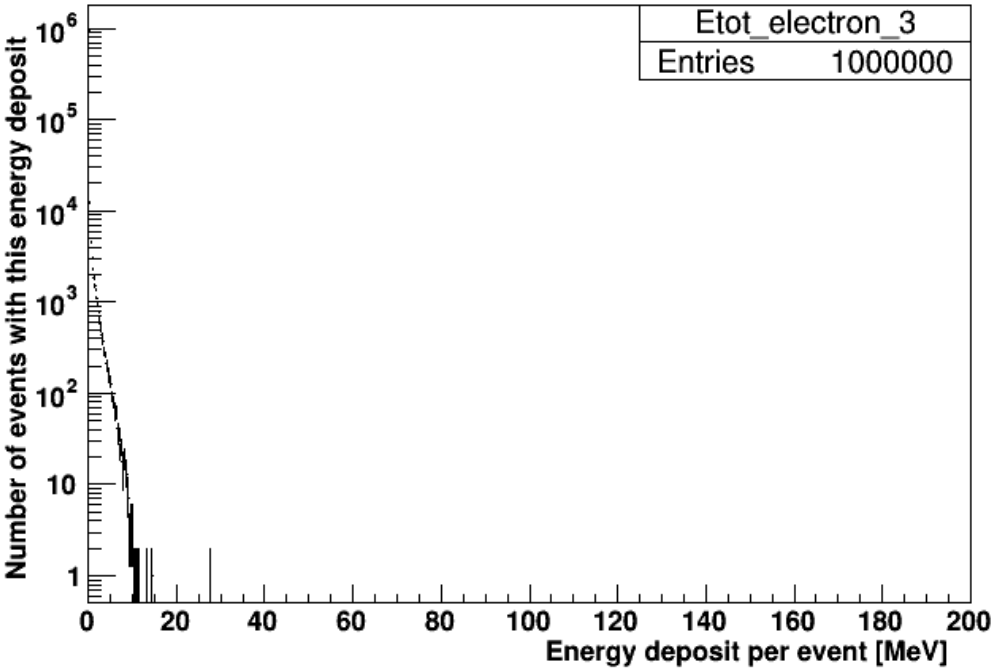

Figure 4.15: Total energy deposit per event, electrons' contribution.

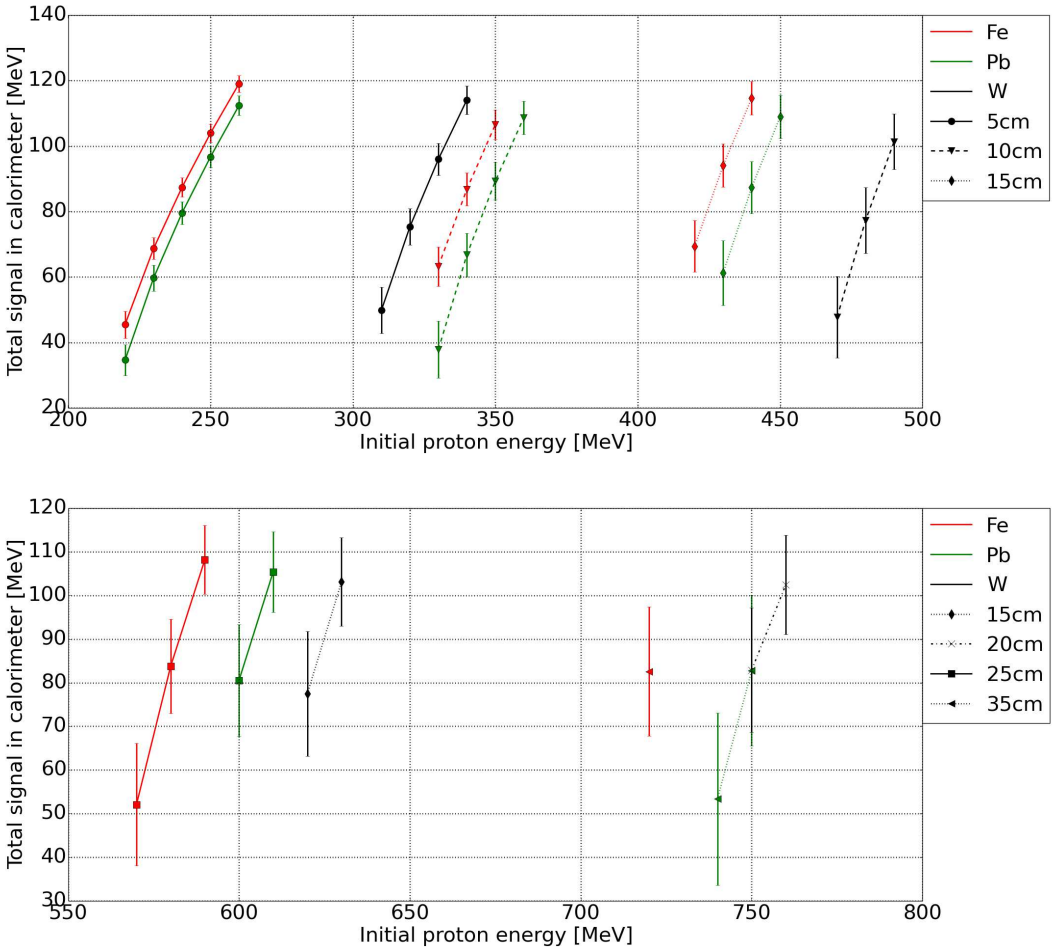

Figure 4.16: Mean value and standard deviation of the Gaussian fit to the total signal in the TERA calorimeter with different preabsorbers in front. $\mu(E)$ is shown as data points with $\sigma(E)$ as error bars. The colors denote the material of the preabsorber block: red for iron, green for lead, black for tungsten. The thicknesses are distinguished by the symbol as depicted in the legends.

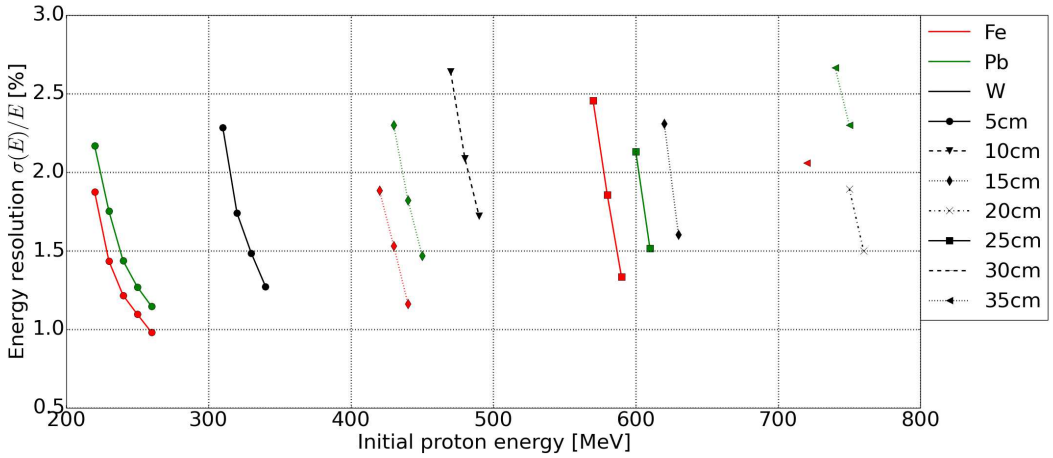

Figure 4.17: $\frac{\sigma(E)}{E}$ of the TERA calorimeter with passive preabsorber block.

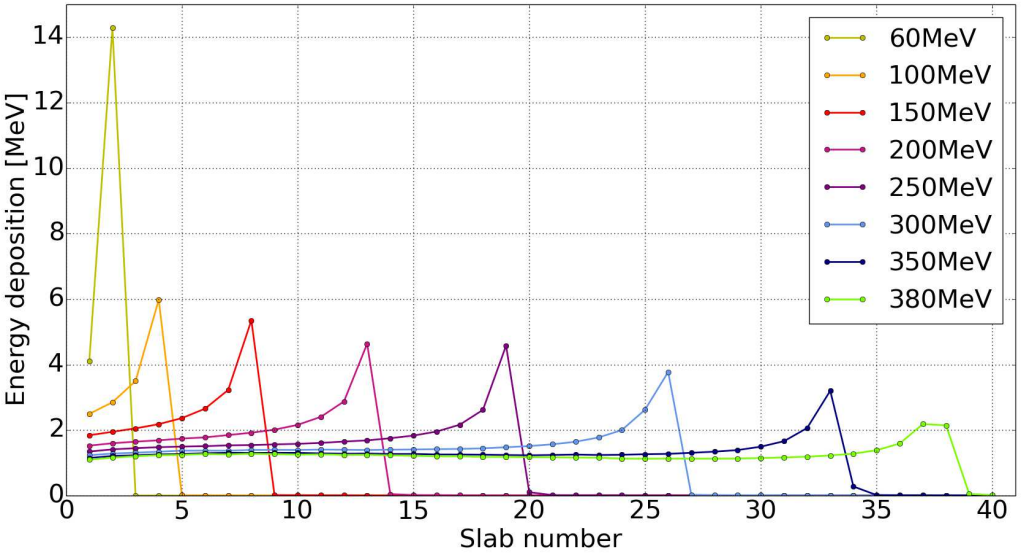

Figure 4.18: Energy deposition per scintillator slice in sampling calorimeter with 3 mm brass absorber alternating 1:1.

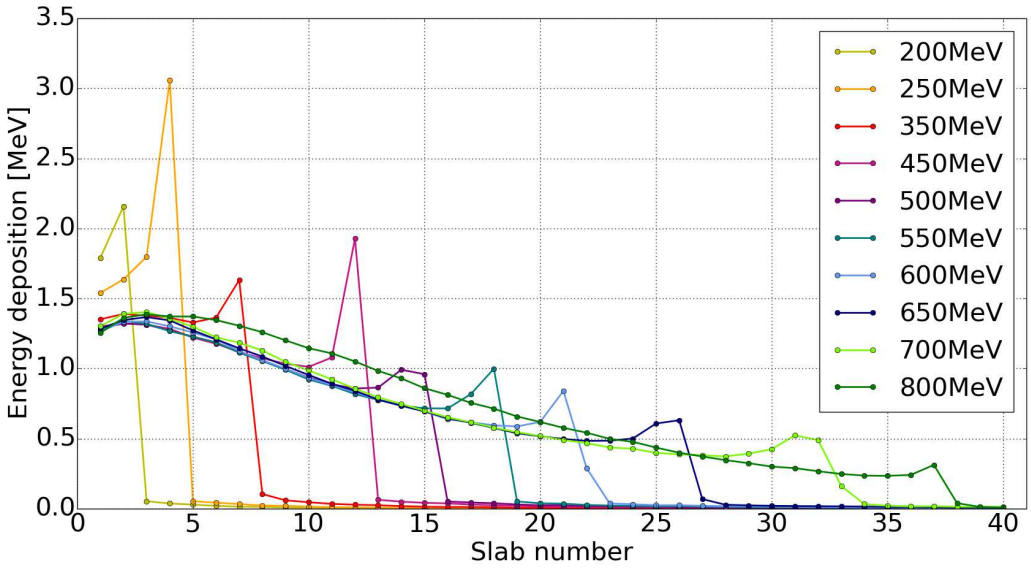

Figure 4.19: Energy deposition per scintillator slice in sampling calorimeter with copper absorber with thickness linearly decreasing from 15 mm to 1 mm.

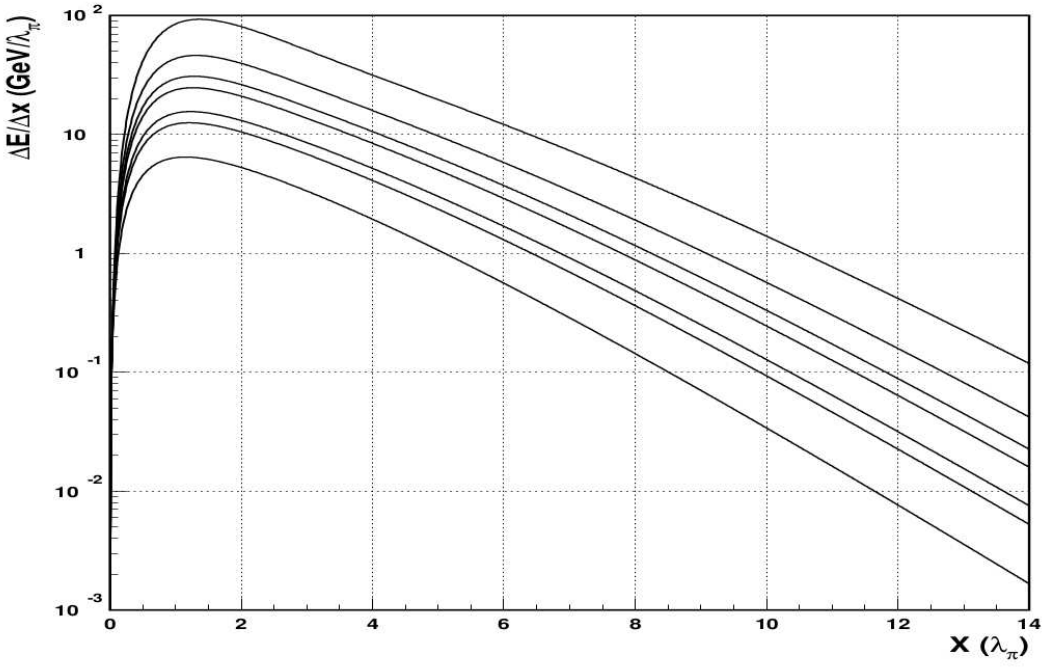

Figure 4.20: Typical longitudinal energy profile of a hadronic shower. The energy deposition of the shower is shown as a function of depth into the calorimeter along the direction of propagation of the particle shower. [58]

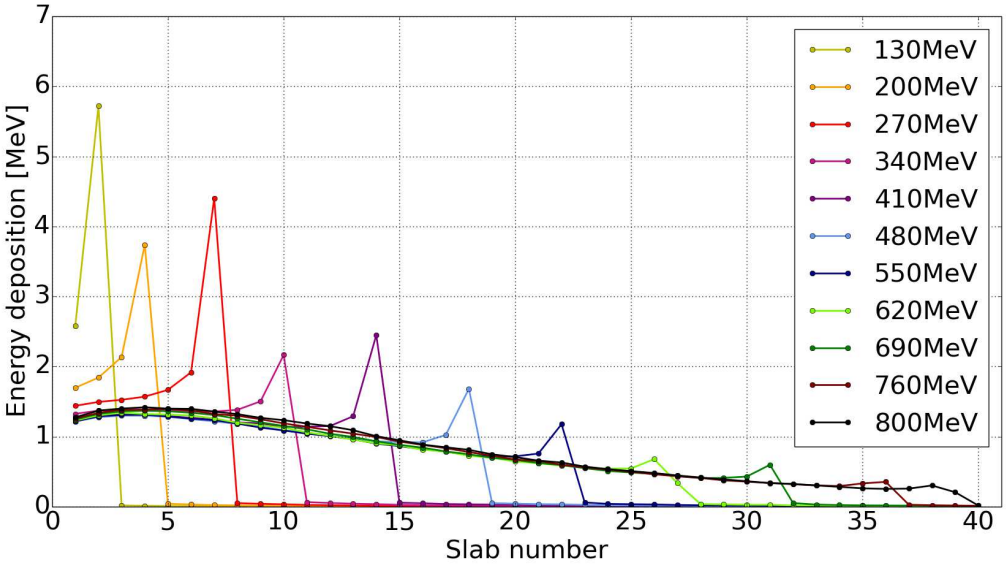

Figure 4.21: Energy deposit per scintillator for sampling calorimeter with 5 mm brass absorber alternating 2:1 with scintillator pieces.

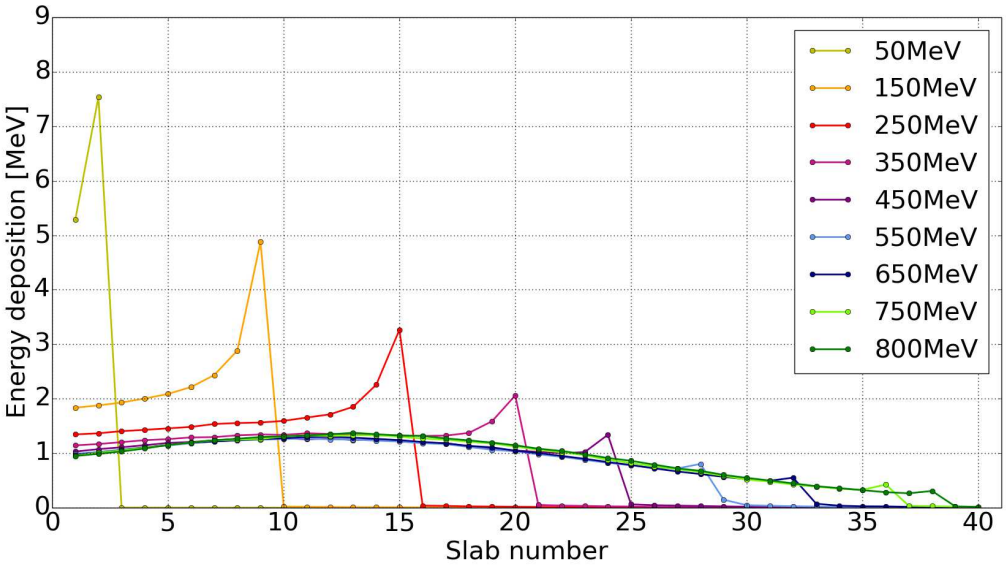

Figure 4.22: Energy deposit per scintillator for sampling calorimeter with brass absorber's thickness linearly increasing from 0.01 mm to 22 mm.

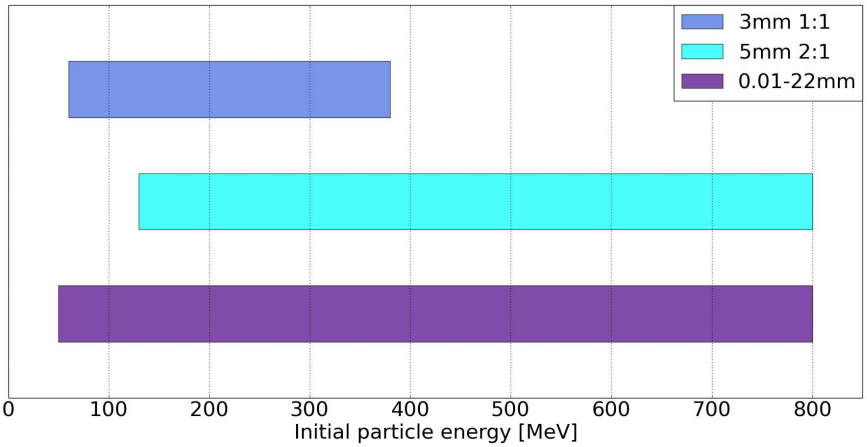

Figure 4.23: Bragg peak energy range of three sampling calorimeter arrangements with brass as absorber material.

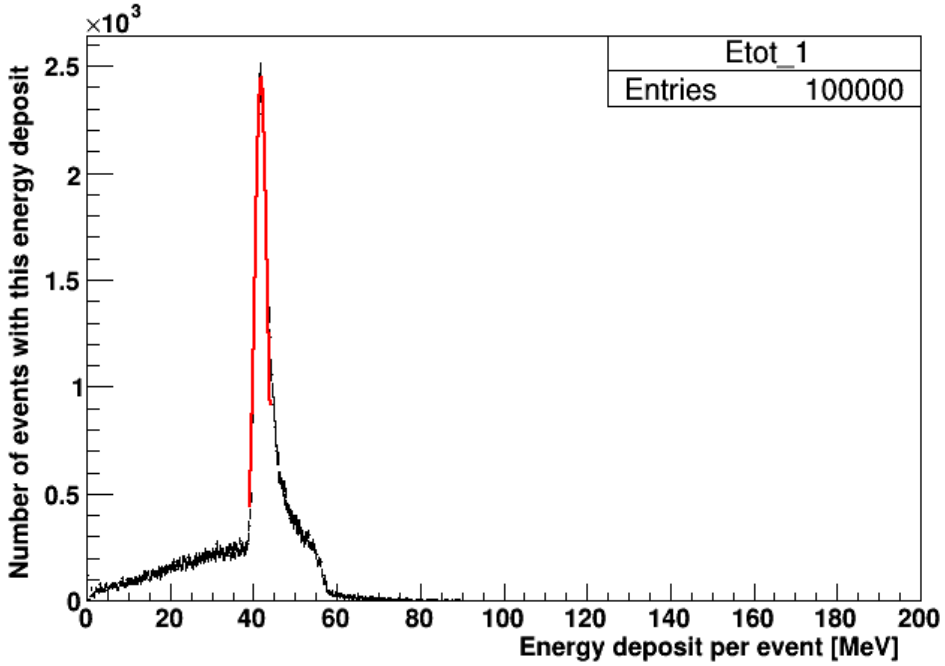

(a) 3 mm 1:1, 290 MeV

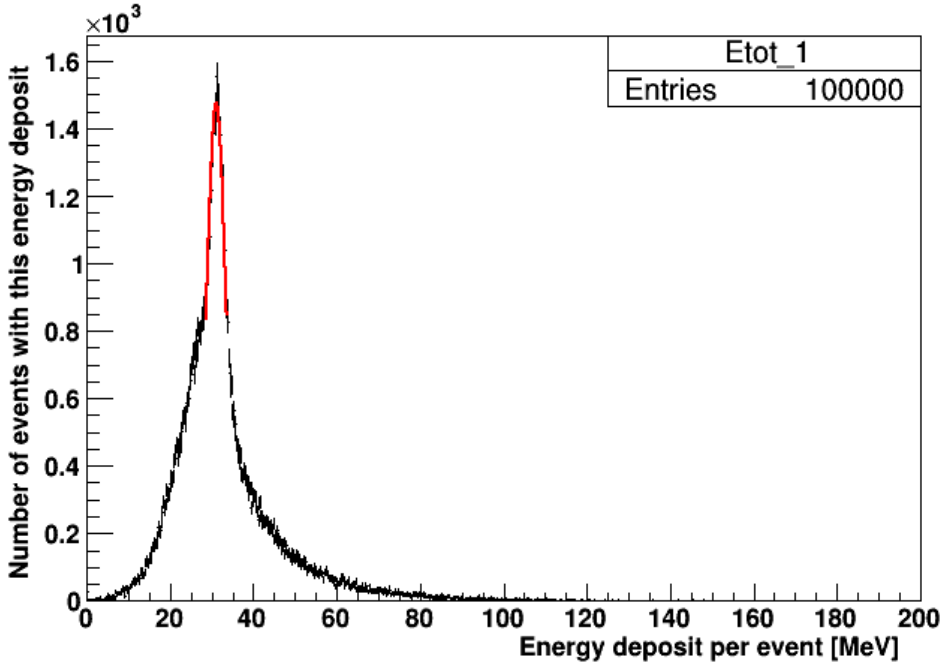

(b) 0.01 mm to 22 mm brass, linearly increasing; 700 MeV

Figure 4.24: Total energy deposit per event for 3 mm brass alternating 1:1 and brass with increasing thickness shows unambiguous narrow peak also at higher energies.

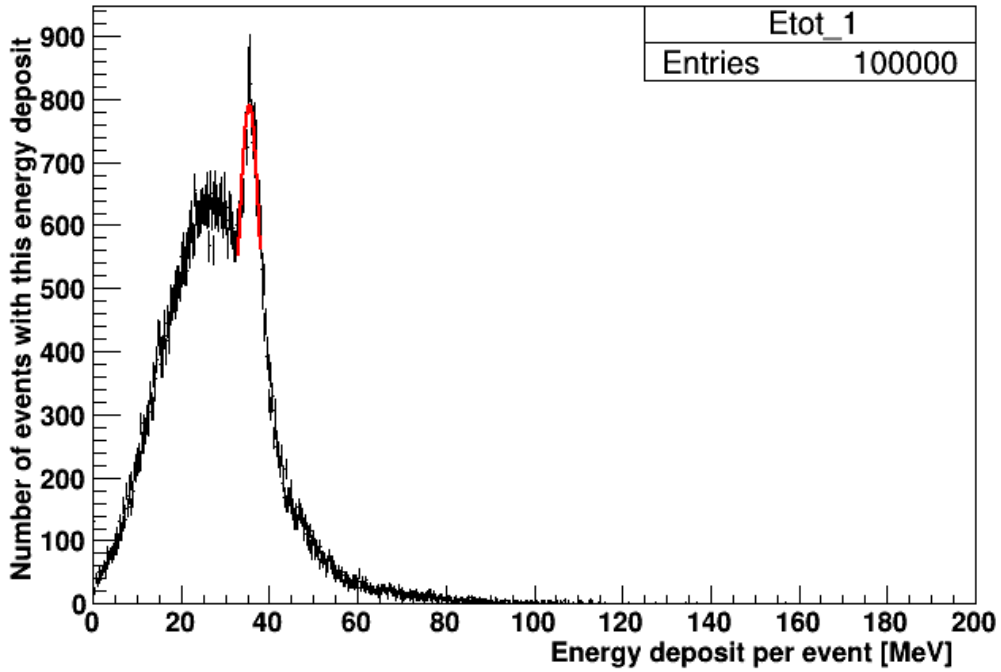

(a) 5 mm brass, 2:1; 750 MeV

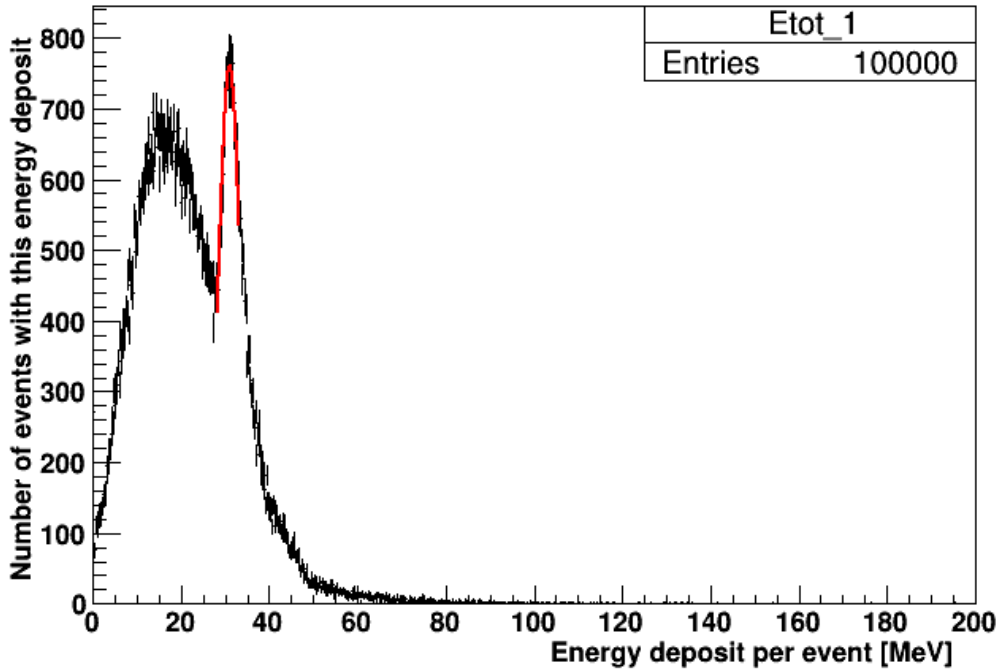

(b) 15 mm to 1 mm bronze, linearly decreasing; 650 MeV

Figure 4.25: In sampling configuration, the total energy deposit per event starts to show a broad subpeak below the narrow peak when the initial proton energy is increased.

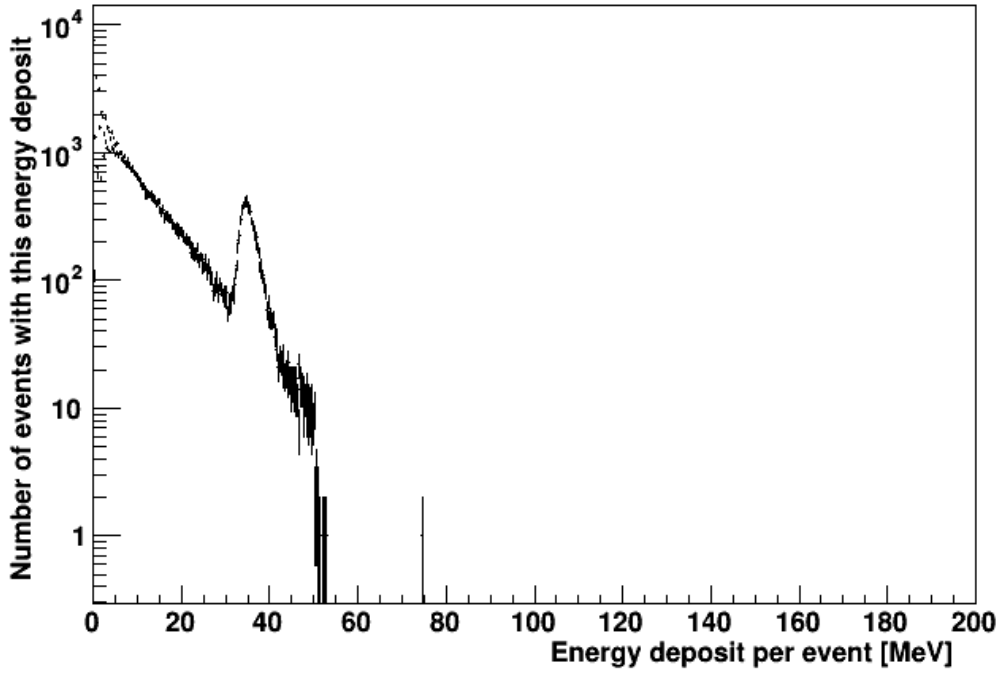

Figure 4.26: Total energy deposit only of primary protons in sampling configuration with 5 mm brass, 2:1 at 750 MeV. The broad subpeak from Figure 4.25a does not appear. The y-axis is shown in logarithmic scale.

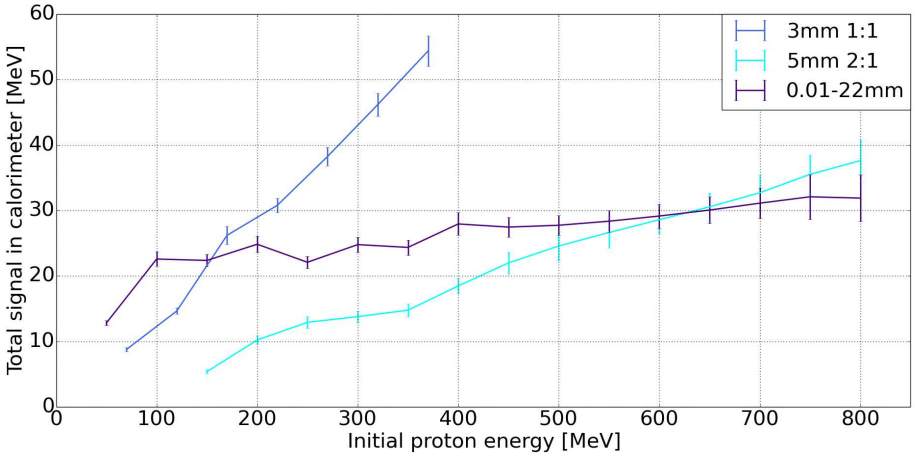

Figure 4.27: $\mu(E)$ with $\sigma(E)$ as error bars for three sampling configurations with brass as absorber material.

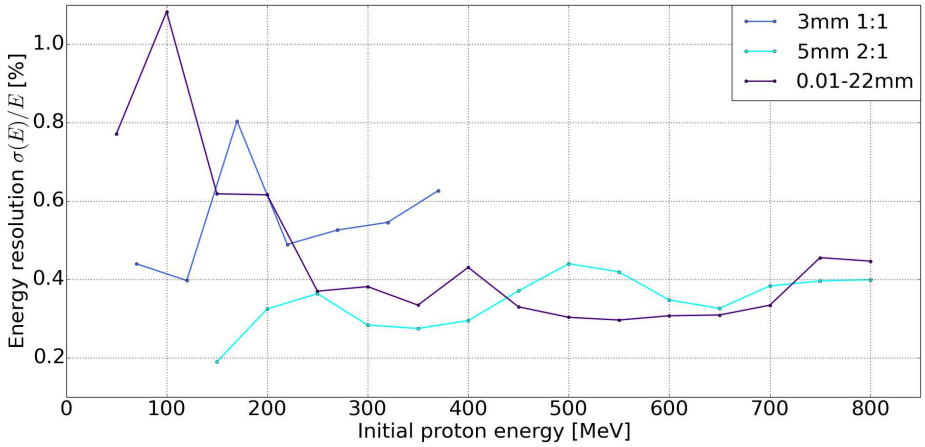

Figure 4.28: $\frac{\sigma(E)}{E}$ for three sampling configurations with brass as absorber material.

5 Conclusion and outlook

For this thesis, a computer simulation of the TERA calorimeter PRR30 was used to analyse its properties and usability in a proton computed tomography setup. The simulation was built with the software toolkit Geant4. Most important information to find was the proton energies which can be measured and the energy resolution for these. The energy resolution was obtained from a fit of a Gaussian function to the main peak of the total energy deposit in the calorimeter, divided by the proton initial energy.
The PRR30 by itself shows a clear Bragg peak for a proton energy range from 40 MeV to 135 MeV. This is the regime in which it can be used for energy measurement of protons. The energy resolution $\sigma(E)/E$ lies between 0.4% and 1.8% in this range. There is a slight trend to smaller σ, i.e. improving energy resolution, for increasing energy.
As the accelerator at MedAustron, where the experiments are conducted, offers proton energies up to 800 MeV, the calorimeter should ideally be usable for proton energy measurement up to this energy. Different geometries were tested to see if this can be achieved by small alterations of the calorimeter.
One attempt was the placement of a passive absorber block in front of the PRR30. Blocks of Fe, Pb, W, PMMA and water with thicknesses up to 40 cm for the metals and up to 2 m for PMMA and water were simulated. For thin preabsorbers, the signal in the calorimeter does not change significantly. The energy range can be shifted to higher energies without making the Bragg peak unrecognisable. With a 5 cm Fe preabsorber, energies up to 260 MeV can be measured in the PRR30. With increasing thickness, the Bragg peak starts to deform, reducing the width of the measurable energy interval. For a 30 cm Fe absorber block, the energy interval is only 15 MeV wide, compared to 45 MeV for 5 cm Fe. The relative energy resolution $\frac{\sigma(E)}{E}$ ranges between 0.9 and 2.7 for the examined blocks and energies.
Also, a sampling calorimeter was simulated with different absorber materials (brass, bronze, copper) and thicknesses. Placement of 3 mm brass between each pair of scintillators results in an increase of the energy interval from 60 MeV to 380 MeV. The Bragg peak is still distinctly visible for each of these energies. With increasing absorber thickness and energy, the sampling calorimeter's Bragg curve starts to show a large flat peak in the first scintillator pieces. Towards the end of the calorimeter, there is still a clearly visible peak, but its height is much lower than the maximum of the broader peak. From the total energy deposit in the PRR30 alone, it is no longer possible to deduce the initial proton energy. Information like the position of the peak has to be added.

Generally, a small extension of the energy range can be done with reasonable results. Configurations which absorb protons of the whole desired range from 50 MeV up to 800 MeV show poor results when it comes to signal significance and energy resolution.

Appendices

A Acronyms

CSDA continuous slowing-down approximation

CT computed tomography

ECR electron cyclotron resonance

GEM gas electron multiplier

HU Hounsfield unit

MCS multiple Coulomb scattering

pCT proton computed tomography

PMT photomultiplier tube

PRR30 Proton Range Radiography 30

PS polystyrene

PVT polyvinyltoluene

RSP relative stopping power

SiPM silicon photomultiplier

SP stopping power

SPAD single photon avalanche diode

TOF time of flight

WLS wavelength shifting

B Code

B.1 Materials

Most materials are built from the Geant4 datebase with the use of the nist manager.

```
G4NistManager* nist = G4NistManager::Instance();
G4Material* air = nist->FindOrBuildMaterial("G4_AIR");
```

The scintillator material BC-408 is built from elements in a function `BC408()`. This is a member function of `DetectorConstruction`.

```
G4Material* DetectorConstruction::BC408()
{
  G4Element* elH = new G4Element("Hydrogen", "H", 1., 1.0079 * g/mole);
  G4Element* elC = new G4Element("Carbon", "C", 6., 12.011 * g/mole);

  double Hpervol = 5.23;
  double Cpervol = 4.74;
  double Hmolmass = elH->GetA();
  double Cmolmass = elC->GetA();

  double Hfraction = 1/( 1+ Cpervol*Cmolmass/(Hpervol*Hmolmass) );
  double Cfraction = 1/( 1+ Hpervol*Hmolmass/(Cpervol*Cmolmass) );

  G4double bcDensity = 1.032 * g / cm3;
  G4int ncomponents;

  G4Material *bc408 = new G4Material("BC-408", bcDensity, ncomponents = 2);
  bc408->AddElement(elH, Hfraction);
  bc408->AddElement(elC, Cfraction);

  return bc408;
}
```

B.2 Volumes

Construction of a volume is done in three steps: solid, logical volume and physical volume. Here as an example the scintillator piece:

```
G4double scintX = 30. * cm, scintY = 30. * cm, scintZ = 3. * mm;
G4Box *scintBox = new G4Box("scintillator", scintX * 0.5, scintY * 0.5, scintZ * 0.5);
G4LogicalVolume *scintLog = new G4LogicalVolume(scintBox, bc408, "scintillator");}
```

A Solid can also be created via boolean operation from other solids:

```
G4SubtractionSolid* aluWrapping = new G4SubtractionSolid("aluWrapping", aluBox,scintBox);
```

Placement of the scintillator pieces with aluminium and paper wrapping in a loop:

```
for (int i = 0; i < fNoOfScintLayers; i++)
{
  ostringstream sName; sName << "scintillator_" << i;
  ostringstream wName1; wName1 << "aluWrapping_" << i;
  ostringstream wName2; wName2 << "paperWrapping_" << i;
  new G4PVPlacement(nullptr, scintillatorPositions.at(i),
    scintLog, sName.str(), worldLog, 0, i );
  new G4PVPlacement(nullptr, scintillatorPositions.at(i),
    aluWrappingLog, wName1.str(), worldLog, 0, i, surfCheck);
  new G4PVPlacement(nullptr, scintillatorPositions.at(i),
    paperWrappingLog, wName2.str(), worldLog, 0, i, surfCheck);
}
```

Member function to add passive preabsorber block:

```
void DetectorConstruction::AddBlock(G4Material* material, G4ThreeVector dimensions,
 G4double frontend)
{
  G4Box* Box = new G4Box("Block", 0.5*dimensions.x(), 0.5*dimensions.y(), 0.5*dimensions.z());
  G4LogicalVolume* Log = new G4LogicalVolume(Box, material, "Block");
  G4double thickness = dimensions.z();
  G4ThreeVector position = G4ThreeVector(0., 0., frontend+0.5*thickness);
  new G4PVPlacement(nullptr,position,Log,"Block",fWorldLog,0,true);

  G4double radius=50.*cm;
  G4Sphere* sphere = new G4Sphere("sphere", radius-0.5 ,radius, 0., 360.*degree,0.,180.*degree);
  G4Box* box = new G4Box("box", 30*0.5*cm, 30*0.5*cm, (radius+thickness*0.5)*0.5);
  G4ThreeVector sphere_position = G4ThreeVector(0.,0.,(0.5*radius-0.25*thickness));
  G4SubtractionSolid* particleSphere = new G4SubtractionSolid("Sphere", sphere, box, 0,
   sphere_position );
  G4Material* air = G4NistManager::Instance()->FindOrBuildMaterial("G4_AIR");
  G4LogicalVolume* particleSphereLog = new G4LogicalVolume(particleSphere, air, "Sphere");
  new G4PVPlacement(nullptr,position,particleSphereLog,"particleSphere",fWorldLog,0,true);
}
```

B.3 Sensitivity

Sensitive detectors are created and then associated with a logical volume.

```
void DetectorConstruction::ConstructSDandField()
{
  G4SDManager* sdManager = G4SDManager::GetSDMpointer();
  sdManager->SetVerboseLevel(2);

  G4VSensitiveDetector* ScintEVol = new EVolSD("scintEVol");
  sdManager->AddNewDetector(ScintEVol);
  SetSensitiveDetector(" scintillator ",ScintEVol);
}
```

Data is retrieved from the step and stored in the hit in `EVolSD`:

```
G4bool EVolSD::ProcessHits(G4Step* step, G4TouchableHistory* /*ROhist*/)
{
  EVolHit* hit = new EVolHit();
    hit->SetVolumeName( step->GetPreStepPoint()->GetPhysicalVolume()->GetName() );
    hit->SetEdep( step->GetTotalEnergyDeposit() );
    hit->SetParticleType( step->GetTrack()->GetParticleDefinition()->GetParticleName() );
  hit->SetParentID(step->GetTrack()->GetParentID());
    fHitsCollection->insert(hit);
}
```

B.4 Physics

The physics list is created in `main` and registered to the run manager.

```
G4PhysListFactory factory;
G4VModularPhysicsList* PhysicsList = factory.GetReferencePhysList("QGSP_BERT_HP");
```

B.5 Primary particle source

Macro file:

```
/gps/particle proton
/gps/pos/centre 0 0 0 cm
/gps/direction 0 0 1
/gps/ene/type Mono
```

In `main`:

```
ostringstream GPSCommand;
GPSCommand <<"/gps/ene/mono " << GPSEnergy.at(i-1) << " MeV";
UImanager->ApplyCommand(GPSCommand.str());
```

B.6 Data output

In `main`:

```
G4AnalysisManager* man = G4AnalysisManager::Instance();
std::ostringstream filename;
filename << "output_"<< Emin << "MeV.root";
man->OpenFile(filename.str());
```

In `RunAction`:

```
std::ostringstream sName;
sName << "Etot_"<< fRunID;
std::ostringstream sTitle;
sTitle << "Total_Energy_deposited_in_all_scintillator_layers_with_GPSEnergy_=_" << fGPSEnergy
<< "_MeV";
man->CreateH1(sName.str(), sTitle.str(),1000,0.,200.);
```

In `EventAction`:

```
if(name=="scintillator")
{
  fE_scint.at(number)+=Edep;
  if( particle == "proton")
  {
    Escint_proton.at(number)+=Edep;
  }
}
for(unsigned int i=0; i<fE_scint.size(); ++i)
{
  man->FillH1(NoOfH1*RunID-(NoOfH1-11), i, fE_scint.at(i));
  man->FillH1(NoOfH1*RunID-(NoOfH1-12), i, Escint_proton.at(i));
}
```

Bibliography

[1] Alfred R Smith. Proton therapy. *Physics in Medicine and Biology*, 51(13):R491–R504, jun 2006.

[2] Wayne D Newhauser and Rui Zhang. The physics of proton therapy. *Physics in Medicine and Biology*, 60(8):R155–R209, mar 2015.

[3] Courtesy of F. Ulrich-Pur.

[4] Robert Renbert Wilson. Radiological use of fast protons. *Radiology*, 47 5:487–91, 1946.

[5] Particle therapy co-operative group. Accessed 13.01.2020.

[6] Accessed 15.01.2020.

[7] Uwe Schneider, Eros Pedroni, and Antony Lomax. The calibration of CT hounsfield units for radiotherapy treatment planning. *Physics in Medicine and Biology*, 41(1):111–124, jan 1996.

[8] G Poludniowski, N M Allinson, and P M Evans. Proton radiography and tomography with application to proton therapy. *The British Journal of Radiology*, 88(1053):20150134, 2015. PMID: 26043157.

[9] R. Schulte, V. Bashkirov, Tianfang Li, Zhengrong Liang, K. Mueller, J. Heimann, L. R. Johnson, B. Keeney, H. F. . Sadrozinski, A. Seiden, D. C. Williams, Lan Zhang, Zhang Li, S. Peggs, T. Satogata, and C. Woody. Conceptual design of a proton computed tomography system for applications in proton radiation therapy. *IEEE Transactions on Nuclear Science*, 51(3):866–872, June 2004.

[10] P. Pemler, J. Besserer, J. de Boer, M. Dellert, C. Gahn, M. Moosburger, U. Schneider, E. Pedroni, and H. Stäuble. A detector system for proton radiography on the gantry of the paul-scherrer-institute. *Nuclear Instruments and Methods in Physics Research Section A: Accelerators, Spectrometers, Detectors and Associated Equipment*, 432(2):483 – 495, 1999.

[11] H.F.-W. Sadrozinski, V. Bashkirov, M. Bruzzi, L.R. Johnson, B. Keeney, G. Ross, R.W. Schulte, A. Seiden, K. Shahnazi, D.C. Williams, and L. Zhang. Issues in proton computed tomography. *Nuclear Instruments and Methods in Physics Research Section A: Accelerators, Spectrometers, Detectors and Associated Equipment*, 511(1):275 – 281, 2003. Proceedings of the 11th International Workshop on Vertex Detectors.

[12] S. Agostinelli et al. Geant4—a simulation toolkit. *Nuclear Instruments and Methods in Physics Research Section A: Accelerators, Spectrometers, Detectors and Associated Equipment*, 506(3):250 – 303, 2003.

[13] Hermann Kolanoski and Norbert Wermes. *Teilchendetektoren. Grundlagen und Anwendungen*. Springer-Verlag, Berlin Heidelberg, 2016.

[14] J. Hyun, P. Piot, and T. Sen. Optics and bremsstrahlung estimates for channeling radiation experiments at fast, 2018.

[15] M. J. Berger and S. M. Seltzer. Tables of energy losses and ranges of electrons and positrons, 1964.

[16] K.A. Olive. Review of particle physics. *Chinese Physics C*, 38(9):090001, aug 2014.

[17] Solange Gagnebin, Damian Twerenbold, Eros Pedroni, David Meer, Silvan Zenklusen, and Christian Bula. Experimental determination of the absorbed dose to water in a scanned proton beam using a water calorimeter and an ionization chamber. *Nuclear Instruments and Methods in Physics Research Section B: Beam Interactions with Materials and Atoms*, 268(5):524 – 528, 2010.

[18] H.E.S. Pettersen, M. Chaar, I. Meric, O.H. Odland, J.R. Sølie, and D. Röhrich. Accuracy of parameterized proton range models; a comparison. *Radiation Physics and Chemistry*, 144:295 – 297, 2018.

[19] G.F. Knoll. *Radiation detection and measurement*. Wiley, 1 1989.

[20] Wolfgang Lucha and Meinhard Regler. *Elementarteilchenphysik in Theorie und Experiment*. Sappl (Kufstein), 1997.

[21] J.B. Birks. *The Theory and Practice of Scintillation Counting*. Elsevier Ltd., 1964.

[22] Anuwut Petdum, Waraporn Panchan, Pattanawit Swanglap, Jitnapa Sirirak, Thanasat Sooksimuang, and Nantanit Wanichacheva. “turn-on” [5]helicene-based fluorescence sensor with very large stokes shift for highly selective detection of ag+ and agnps. *Sensors and Actuators B: Chemical*, 259:862–870, 2018.

[23] `https://scionix.nl/frame/`. Accessed on 16.01.2020.

[24] Valentina Giacometti. *Modelling and improvement of proton computed tomography*. PhD thesis, University of Wollongong, 2016.

[25] A A Mustafa and D F Jackson. The relation between x-ray CT numbers and charged particle stopping powers and its significance for radiotherapy treatment planning. *Physics in Medicine and Biology*, 28(2):169–176, feb 1983.

[26] George T.Y. Chen, Rajinder P. Singh, Joseph R. Castro, John T. Lyman, and Jeanne M. Quivey. Treatment planning for heavy ion radiotherapy. *International Journal of Radiation Oncology*Biology*Physics*, 5(10):1809 – 1819, 1979.

[27] Robert P Johnson. Review of medical radiography and tomography with proton beams. *Reports on Progress in Physics*, 81(1):016701, nov 2017.

[28] Dongxu Wang, T. Rockwell Mackie, and Wolfgang A. Tomé. On the use of a proton path probability map for proton computed tomography reconstruction. *Medical Physics*, 37, 2010.

[29] Dongxu Wang, T. Rockwell Mackie, and Wolfgang A. Tomé. Bragg peak prediction from quantitative proton computed tomography using different path estimates. *Physics in Medicine and Biology*, 56, 2011.

[30] T. Schreiner, M. Stock, P. Georg, and D. Georg. Medaustron: First years of operation. *Nuclear Physics News*, 29(2):22–24, 2019.

[31] Markus Stock, Petra Georg, Ramona Mayer, Till T. Böhlen, and Stanislav Vatnitsky. Development of clinical programs for carbon ion beam therapy at medaustron. *International Journal of Particle Therapy*, 2(3):474–477, 2015.

[32] L Badano, Michael Benedikt, P J Bryant, M Crescenti, P Holy, A T Maier, M Pullia, S Rossi, and P Knaus. *Proton-Ion Medical Machine Study (PIMMS), 1.* Mar 1999.

[33] P. J. Bryant et al. Proton-Ion Medical Machine Study (PIMMS), 2. 2000.

[34] M. Benedikt and A. Wrulich. Medaustron—project overview and status. *The European Physical Journal Plus*, 126(7):69, Jul 2011.

[35] Alexander Burker, Thomas Bergauer, Albert Hirtl, Christian Irmler, Stefanie Kaser, Peter Paulitsch, Vera Teufelhart, Felix Ulrich-Pur, and Manfred Valentan. Imaging with ion beams at medaustron. *Nuclear Instruments and Methods in Physics Research Section A: Accelerators, Spectrometers, Detectors and Associated Equipment*, page 162246, 2019.

[36] Courtesy of A. Burker.

[37] Ugo Amaldi. TERA Programme: Medical Applications of Protons and Ions. 1996.

[38] Ugo Amaldi. Oncological hadrontherapy and the projects of the tera foundation. *Nuclear Physics News*, 7(2):23–28, 1997.

[39] U Amaldi. Hadrontherapy in the world and the programmes of the tera foundation. *Tumori*, 84(2):188—199, 1998.

[40] M. Bucciantonio, U. Amaldi, R. Kieffer, N. Malakhov, F. Sauli, and D. Watts. Fast readout of gem detectors for medical imaging. *Nuclear Instruments and Methods in Physics Research A*, 718:160–163, 2012.

[41] U. Amaldi, A. Bianchi, Y-H. Chang, A. Go, W. Hajdas, N. Malakhov, J. Samarati, F. Sauli, and D. Watts. Construction, test and operation of a proton range radiography system. *Nuclear Instruments and Methods in Physics Research Section A: Accelerators, Spectrometers, Detectors and Associated Equipment*, 629(1):337 – 344, 2011.

[42] Martina Bucciantonio. *Development of an advanced Proton Range Radiography system for hadrontherapy*. PhD thesis, Universitat Bern, 2015.

[43] Saint-Gobain Ceramics & Plastics, Inc. `https://www.crystals.saint-gobain.com/sites/imdf.crystals.com/files/documents/bc400-404-408-412-416-data-sheet.pdf`. Accessed 23.09.2018.

[44] F. Sauli. Gem: A new concept for electron amplification in gas detectors. *Nuclear Instruments and Methods in Physics Research Section A: Accelerators, Spectrometers, Detectors and Associated Equipment*, 386(2):531 – 534, 1997.

[45] L. L. Carter and E. D. Cashwell. Particle-transport simulation with the monte carlo method, 1975.

[46] Geant4 book for application developers. `http://geant4-userdoc.web.cern.ch/geant4-userdoc/UsersGuides/ForApplicationDeveloper/html/index.html`. Accessed 16.01.2020.

[47] `http://geant4.web.cern.ch/`. Accessed 16.1.2020.

[48] Geant4 Collaboration. Geant4 material database. `http://geant4-userdoc.web.cern.ch/geant4-userdoc/UsersGuides/ForApplicationDeveloper/html/Appendix/materialNames.html#g4matrdb`. Accessed 20.08.2018.

[49] C. Altunbas, M. Cap, K. Dehmelt, J. Ehlers, J. Friedrich, I. Konorov, A. Gandi, S. Kappler, B. Ketzer, R. De Oliveira, S. Paul, A. Placci, L. Ropelewski, F. Sauli, F. Simon, and M. van Stenis. Construction, test and commissioning of the triple-gem tracking detector for compass. *Nuclear Instruments and Methods in Physics Research A*, 490:177–203, 2002.

[50] Geant4 Collaboration. Reference physics lists. `https://geant4.web.cern.ch/node/155`. Accessed 20.05.2019.

[51] G.Folger and J.P.Wellisch. String parton models in geant4. *Computing in High Energy and Nuclear Physics*, 2003.

[52] D.H. Wright and M.H. Kelsey. The geant4 bertini cascade. *Nuclear Instruments and Methods in Physics Research A*, 2015.

[53] Rene Brun and Fons Rademakers. Root — an object oriented data analysis framework. *Nuclear Instruments and Methods in Physics Research Section A: Accelerators, Spectrometers, Detectors and Associated Equipment*, 389(1):81 – 86, 1997. New Computing Techniques in Physics Research V.

[54] https://root.cern.ch/. Accessed 17.12.2019.

[55] urlhttps://root.cern.ch/root/htmldoc/guides/users-guide/ROOTUsersGuide.html. Accessed 10.12.2018.

[56] M. Bucciantonio, U. Amaldi, R. Kieffer, F. Sauli, and D. Watts. Development of a fast proton range radiography system for quality assurance in hadrontherapy. *Nuclear Instruments and Methods in Physics Research A*, 732:564–567, 2013.

[57] Q Ingram. Energy resolution of the barrel of the CMS electromagnetic calorimeter. *Journal of Instrumentation*, 2(04):P04004–P04004, apr 2007.

[58] Y. A. Kulchitsky, M. V. Kuzmin, and V. B. Vinogradov. Longitudinal hadronic shower development in a combined calorimeter, 1999.